

ABSTRACT

LUND, KELSEY ALEXANDRA. How the Gentle Winds Beckon: *r*-Process Nucleosynthesis in Neutron Star Merger Winds. (Under the direction of Gail McLaughlin).

The rapid neutron capture process (*r*-process) is one of the main mechanisms whereby elements heavier than iron are synthesized, and is entirely responsible for the natural production of the actinides. 50 years ago, it was proposed that the *r*-process could occur in the unbinding of material during the inspiral and merger of either a neutron star and black hole, or two neutron stars. Multi-messenger observations of the binary neutron star merger, GW170817, provided the first confirmation of lanthanide production in the merger ejecta. However, the full picture of the role neutron star mergers play in the production of galactic *r*-process abundances remains unclear. Understanding the intricacies of nucleosynthesis neutron star mergers is a multi-physics problem spanning several orders of magnitude in physical and temporal scale.

In this work, I combine the use of *r*-process network calculations, general relativistic magnetohydrodynamics simulations with neutrino transport, and chiral effective field theory informed nuclear equations of state to probe uncertainties in *r*-process production from binary neutron star mergers. I investigate the role of global β -decay rates and other properties of off-stability nuclei in nuclear energy generation, kilonova light curve modeling, and the enhancement of heavy elements in some of the oldest stars. I further investigate the role of magnetic fields in the evolution of the post-merger black hole accretion disk system and its ability to enhance or hinder *r*-process production. I combine uncertainties from nuclear physics and magnetohydrodynamics with multi-messenger data from GW170817 to constrain the maximum neutron star mass.

In particular, actinide production is an essential part of studies of the *r*-process, as these elements are solely synthesized via the *r*-process. In this work, I find that actinide production can be enhanced by strong magnetic fields as well as slow β -decay rates in heavy nuclei. With the work contained in this dissertation, I find the post-merger system to continue to be a promising site for the production of a full *r*-process pattern, and highlight key areas where questions still remain.

© Copyright 2024 by Kelsey Alexandra Lund

All Rights Reserved

How the Gentle Winds Beckon:
r-Process Nucleosynthesis in Neutron Star Merger Winds

by
Kelsey Alexandra Lund

A dissertation submitted to the Graduate Faculty of
North Carolina State University
in partial fulfillment of the
requirements for the Degree of
Doctor of Philosophy

Physics

Raleigh, North Carolina
2024

APPROVED BY:

James Kneller

Richard Longland

Jonathan Engel

Shobhan Gaddameedhi

Gail McLaughlin
Chair of Advisory Committee

BIOGRAPHY

Kelsey Alexandra Lund was born in Southern California, but spent different epochs growing up in Mexico, Catalonia and Florida. After a semester of taking classes and walking up mountains in Arizona, her undergraduate career continued at MiraCosta College, with beach breaks between classes and work. She obtained her Bachelor of Science in Physics at University of California San Diego in 2017. During her years as an undergraduate, she dabbled in experimental cosmology and radio astronomy, but found her place in nuclear astrophysics. She pursued this as soon as she began her graduate studies at North Carolina State University in 2018. In the summer of 2020, she joined T-Division at Los Alamos National Laboratory.

Kelsey is an accumulator of languages, with fluency in English, Catalan, and Spanish- and a passable ability to communicate in a few others.

"The mountains are calling, but the sea beckons."

ACKNOWLEDGEMENTS

I am profoundly grateful to my PhD advisor, Gail McLaughlin, for her guidance and mentorship throughout my time as her student. I sincerely appreciate the opportunities she has provided for me over these last 6 years to learn and grow, as well as for her patience, understanding, and encouragement throughout it all.

The work that I have done as a graduate student has been greatly enriched thanks to my mentors, collaborators, and friends in Los Alamos. I would especially like to express my gratitude to Matthew Mumpower, Jonah Miller, and Ingo Tews- thanks for being part of the Cool Collaboration.

Given the computational demands of the work presented here, I wish to express my appreciation for the people who have come to my rescue when computers and I did not get along. Thanks to Daniel and Kevin in the NCSU Physics department, Dodi at the Notre Dame CRC, as well as Don, the HPC and AskIT teams at Los Alamos National Lab. Similarly, I would like to extend my appreciation to the administrators who have facilitated all the bureaucratic aspects of this endeavor, especially Rhonda, Lori, Beth, Jen, Lily, and Leah.

Collaborations and friendships are the lifeblood of academic endeavor. I am deeply grateful to the collaborators with whom I have had the pleasure of working, including (but not limited to) Rebecca, Erika, Trevor, Jenni, Yonglin, and Rahul. I am also grateful to the mentors and teachers I have had throughout my career as a scientist as well as the collaborations I have been part of, including C. Cottrell, J. Cole, G. Fuller, C. Hales, B. Keating, E. Michelsen, T. Schäfer, and the FIRE Collaboration. Thanks also to the NCSU NucAstro Supergroup, the Knightsbridge Boys, the Person St. crew, and the Leonard family, whose friendship and support I have valued greatly.

Finally, I want to thank my family and friends for their love, encouragement, and for helping keep life fun. I hit the jackpot when I ended up with Kendra and CB as my siblings. My mother has been an endless source of love, patience, and inspiration; words alone do not seem sufficient to express how grateful I am to her. Lastly, I want to thank Oriol, my husband and best friend, for standing by me through the high moments and the low, and always reminding me that everything is going to be okay.

DEDICATION

To the four best friends a girl can have:

This dissertation is dedicated to my brother, sister, husband, and especially my mother.



Figure 1: Early depiction of the reading of a dissertation in nuclear astrophysics. Credit: Jerome et al. (1330).

TABLE OF CONTENTS

| | |
|--|-------------|
| List of Tables | viii |
| List of Figures | ix |
| Chapter 1 The Synthesis of Elements in the Universe | 1 |
| 1.1 Nucleosynthesis in a Nutshell | 2 |
| 1.1.1 Light Element Nucleosynthesis | 2 |
| 1.1.2 Heavy Element Nucleosynthesis | 5 |
| 1.2 Rapid Neutron Capture Process | 7 |
| 1.3 Astrophysical Sites of the r-Process | 7 |
| 1.3.1 Supernovae | 9 |
| 1.3.2 Compact Object Mergers | 10 |
| 1.4 Astrophysical Signatures of r-Process Nucleosynthesis | 13 |
| 1.4.1 Solar and Solar System Abundances | 13 |
| 1.4.2 Metal-Poor Stars | 14 |
| 1.4.3 Compact Object Mergers and Kilonovae | 15 |
| Chapter 2 Methods and Techniques | 17 |
| 2.1 Nuclear Data | 18 |
| 2.2 Nuclear Reaction Networks | 19 |
| 2.2.1 PRISM | 19 |
| 2.3 Accretion Disk Simulations | 22 |
| 2.3.1 nubhlight | 23 |
| Chapter 3 From Mergers to the Stars: Sources of Uncertainty in Different Stages of r-Process Modeling | 26 |
| 3.1 The Blink of an Eye: Fractions of a Second | 27 |
| 3.2 Outward Bound: Milliseconds to Seconds | 28 |
| 3.3 Moving up in the World: Seconds to Years | 30 |
| Chapter 4 The Influence of Beta-Decay Rates on r-Process Observables | 31 |
| 4.1 Abstract | 32 |
| 4.2 Introduction | 32 |
| 4.3 Method | 34 |
| 4.3.1 Model Set and Nucleosynthesis | 35 |
| 4.3.2 Nuclear Heating | 39 |
| 4.3.3 Semi-Analytic Light Curve Model | 39 |
| 4.3.4 Nuclear Cosmochronometry | 40 |
| 4.4 Effective Heating and Light Curve | 41 |
| 4.4.1 Single Trajectory | 41 |
| 4.4.2 Combined Trajectories | 50 |
| 4.5 Applications for Nuclear Cosmochronometry | 57 |
| 4.5.1 Actinide Constraint | 59 |
| 4.5.2 Chronometric Agreement | 59 |

| | |
|---|------------|
| 4.6 Conclusion | 64 |
| Chapter 5 Magnetic Field Strength Effects on Nucleosynthesis from Neutron Star Merger Outflows | 68 |
| 5.1 Abstract | 69 |
| 5.2 Introduction | 69 |
| 5.3 Method | 70 |
| 5.3.1 Post-Merger Disk Evolution | 70 |
| 5.3.2 Nucleosynthesis | 73 |
| 5.4 Outflow Properties | 75 |
| 5.4.1 Mass Ejection | 75 |
| 5.4.2 Nucleosynthetic Conditions | 77 |
| 5.5 Nucleosynthesis Results | 80 |
| 5.5.1 Global Results | 80 |
| 5.5.2 Angular Dependence | 80 |
| 5.6 Conclusion and Outlook | 85 |
| Chapter 6 Kilonova Emissions from Neutron Star Merger Remnants: Implications for Nuclear Equation of State | 88 |
| 6.1 Introduction | 89 |
| 6.2 Equations of State | 91 |
| 6.3 Post-Merger Disk Mass | 91 |
| 6.4 Disk to Wind Mass | 92 |
| 6.5 Kilonovae from Disk Winds | 95 |
| 6.6 Kilonova Constraints on Nuclear EoS | 97 |
| 6.7 Summary and Discussion | 98 |
| 6.8 Conclusion | 101 |
| Chapter 7 Summary & Outlook | 102 |
| APPENDICES | 106 |
| Appendix A Variables | 107 |
| Appendix B Grid Size and Resolution | 108 |
| Appendix C Disk Mass Fit Formulae | 110 |
| C.1 Binary Tidal Deformability | 110 |
| C.2 Prompt Collapse Threshold Mass | 111 |
| C.3 Lightest NS Compactness | 112 |
| Appendix D Numerical Relativity Simulations of Binary Neutron Star Mergers | 113 |
| References | 118 |

LIST OF TABLES

| | |
|--|-----|
| Table 1.1 Classification criteria of low-metallicity stars as relevant for this body of work. It should be noted that, although not listed here, the prefixes used to describe metal-poorness extend to “Giga-metal-poor”, where $[Fe/H] < -9.0$, followed by “Ridiculously metal-poor”, for which no observations exist (Frebel 2018). | 15 |
| Table 2.1 Description of symbols used in equations of GR ν MHD. | 24 |
| Table 4.1 Nuclear mass models (and associated references) used in nucleosynthesis calculations. | 37 |
| Table 4.2 Names of select r-ii stars with their observed abundances. These stars are sorted by increasing actinide enhancement. | 40 |
| Table 4.3 Average of the ratios of total effective heating using NES or MKT to total effective heating using MLR beta decay rates, over different time periods. In the 1-10 days column, the average ratio of bolometric luminosity is listed in parentheses. Bold-faced values indicate an average change of $\pm 50\%$ or more. | 48 |
| Table 5.1 <i>Top:</i> Global outflow properties for each disk. <i>Bottom:</i> Mass and composition properties for each angular cut within each disk. | 77 |
| Table 6.1 Wind masses from GRMHD simulations of NS-NS or NS-BH mergers, shown in solar masses as well as a percentage of the initial disk mass. In the first column, the remnant black hole masses are included in parentheses. | 94 |
| Table 6.2 Key parameters of models 12 (here Z12) and 13 (here Z13) from Zhu et al. (2021) used in this work. These include the theoretical nuclear mass model fission rates and daughter production distributions used. Given that these models were constructed from combinations of single- Y_e trajectories, we also include the average electron fraction for each case. | 98 |
| Table A.1 A summary of common acronyms and their abbreviations. | 107 |
| Table A.2 A list of common physical variables used in this work. | 107 |
| Table A.3 A list of common physical constants and their abbreviations. | 107 |
| Table D.1 Simulation data from numerical relativity simulations. | 113 |

LIST OF FIGURES

| | | |
|------------|---|----|
| Figure 1 | Early depiction of the reading of a dissertation in nuclear astrophysics. Credit: Jerome et al. (1330) | v |
| Figure 1.1 | Elemental abundances of the solar system. Data is taken from Asplund et al. (2009), with <i>r</i> -process residuals computed from Arlandini et al. (1999), and is scaled following the \log_e notation, where $N_H = 12$ | 3 |
| Figure 1.2 | Termination region of the <i>s</i> -process in relation to the long-lived isotopes of thorium and uranium, highlighting the “Chasm of α -Instability” | 6 |
| Figure 1.3 | Decay rates of nuclei at the termination point of the <i>s</i> -process and beyond. Data taken from Kondev et al. (2021). Darker shades represent nuclei with longer half-lives | 8 |
| Figure 1.4 | Scaled abundances of five metal-poor, <i>r</i> -process enhanced stars selected for their uranium abundances. The solar <i>r</i> -process abundances pattern is shown as a black line. | 16 |
| Figure 2.1 | Major outflow components from a black hole accretion disk that could result from a binary neutron star merger. The outflows are shown from the side (xz plane) and colored by electron fraction, Y_e . This snapshot was taken roughly 30 ms into a nubhlight simulation with a weak initial magnetic field. | 22 |
| Figure 3.1 | Spatial trajectories of tracers responsible for the production of 50% of lanthanide (top) and actinide (bottom) production by mass, colored by lanthanide (or actinide) mass fraction at 1 GYr (left) and Y_e at $T_9 = 10$ (right) for three GRMHD accretion disk simulations. | 29 |
| Figure 4.1 | Logarithmic ratios of NES (top), MLR (center), and MKT (bottom) beta decay rates with respect to MLR03 beta decay rates. The color bar is adjusted to values of -2,2 to reveal trends more clearly. The area covered by the Nubase 2016 data set (Audi et al. 2017) is removed. | 36 |
| Figure 4.2 | Distribution of combined single- Y_e trajectories. The color of each line indicates the average Y_e of the “combined trajectory”. A selection of combinations are shown as a guide to highlight the double-peak structures within the distribution. This color scheme is used throughout this work to refer to results for each combined trajectory, with the bluer combinations having less neutron-rich (low Y_e) material and the more brown combinations having more neutron-rich material. | 38 |
| Figure 4.3 | Range of effective heating rate predictions for all nuclear mass models from Table 4.1 when a single Y_e trajectory is considered. Looking at the columns from left to right, the initial electron fraction increases from 0.02 to 0.18 to 0.21. The width of each band corresponds to the range of heating predictions for the NES (dark blue), MLR (pink), or MKT (light blue) simulations with the nine different mass models and both 50/50 as well as K&T fission daughter product distributions for which we calculate heating. For comparison, the maximum total heating is shown for each set of simulations as a series of dotted lines. | 43 |

| | | |
|-------------|---|----|
| Figure 4.4 | Uncertainty range of analytic light curve models for all nine theoretical nuclear models from Table 4.1, when a single Y_e trajectory is considered, with the calculation carried out to 40 days post-merger. The initial electron fraction increases from 0.02 to 0.18 to 0.21 from top to bottom. The width of each band corresponds to the range of luminosity predictions when the NES (dark blue), MLR (pink), or MKT (light blue) beta decay rates are used, and include both 50/50 and KT fission yields. | 44 |
| Figure 4.5 | Ratio of beta decay rates used in NES:MLR (top) or MKT:MLR (bottom) calculations in the region feeding into important alpha decay heaters (outlined in black boxes) identified in, for example, sly4.18. We show here only the rates subject to theoretical models; those covered by the Nubase2016 data set are shown in grey. | 46 |
| Figure 4.6 | Theoretical branching ratios for a selection of key nuclei that have the potential to be important spontaneous fission heaters, as identified in, for example, hfb22.02. The grey-filled isotopes have experimentally determined values; the colored isotopes remain unmeasured. Light green, teal, and dark green represent the branchings expected for alpha decay, spontaneous fission, and beta decay, respectively. In the bottom right panel, we show the chemical names for highlighted isotopes for ease of identification. | 49 |
| Figure 4.7 | Abundance patterns at 10 GYr for combined trajectories displayed in Figure 4.2 using the FRDM2012 mass model, with the same coloring convention (brown representing more neutron-rich combinations, and blue more neutron-poor). Solar r-process residuals (Asplund et al. 2009) are plotted as black stars, scaled such that the abundance of bromine ($Z = 35$) is $10^{-2.5}$ | 51 |
| Figure 4.8 | Range of effective heating rate predictions using the FRDM2012 mass model with 50/50 fission product yields when composite- Y_e trajectories are considered. From left to right, the beta decay description used is NES, MLR, MKT. The color scheme corresponds to that shown in Figure 4.2. As in Figure 4.3, we replicate the total heating curves shown in the top row in the bottom three rows as light grey lines for easier comparison. | 53 |
| Figure 4.9 | Range of effective heating rate predictions using the HFB22 mass model when composite- Y_e trajectories are considered with 50/50 fission product yields. From left to right, the beta decay description used is NES, MLR, MKT. The color scheme corresponds to that shown in Figure 4.2. As in Figure 4.3, we replicate the total heating curves shown in the top row in the bottom three rows as light grey lines for easier comparison. | 54 |
| Figure 4.10 | Uncertainty range of analytic light curve models for FRDM2012 nuclear model with multiple- Y_e composition using 50/50 fission product yields. From left to right, the beta decay description used is NES, MLR, MKT. The color scheme corresponds to that shown in Figure 4.2, with the most striking blue representing the behavior of the most neutron-poor material and the darkest brown that of the most neutron-rich material. | 55 |

| | | |
|-------------|--|----|
| Figure 4.11 | Uncertainty range of analytic light curve models for HFB22 nuclear model with multiple- Y_e composition using 50/50 fission product yields. From left to right, the beta decay description used is NES, MLR, MKT. The color scheme corresponds to that shown in Figure 4.2, with the most striking blue representing the behavior of the most neutron-poor material and the darkest brown that of the most neutron-rich material. | 55 |
| Figure 4.12 | Maximum uncertainty from the use of different beta decay rates for the stars listed in Table 4.2, with each row corresponding to a different star. The left column shows ages computed using the 50/50 fission yields, while the right column contains those obtained using the K&T fission yields. As throughout this work, NES calculations are shown in dark blue, while MLR and MKT calculations are shown in pink and light blue, respectively. The regions are filled in to show the range of values obtained using the three different chronometers, as described in Equations 4.12-4.14. Dashed horizontal lines indicate a value of 13.7 GYr; solid horizontal lines indicate a value of 0 GYr. | 58 |
| Figure 4.13 | Composite values of initial production abundances of europium (red), thorium (teal), and uranium (pink), separated out by beta decay rates used. NES, MLR, and MKT simulations are shown in the top, middle, and bottom rows, respectively. The left column shows results obtained using the 50/50 fission yields, and the right column shows those obtained using the K&T fission yields. The horizontal axis shows average Y_e (with increasing neutron richness) of the combined trajectories. | 60 |
| Figure 4.14 | Uncertainty in age estimates due to uncertain nuclear physics and Y_e for fixed stellar observations. The ages in this figure are calculated solely using the U:Th abundance. A horizontal dotted line indicates the value of 13.7 GYr. NES, MLR, and MKT calculations are shown as dark blue, pink, and light blue bars, respectively. The left panel shows results obtained using the 50/50 fission yields while the right panel shows those obtained using the K&T fission yields. | 61 |
| Figure 4.15 | Full range of predicted age values for each star when the full range of observational error bars plus the full uncertainty from the composite trajectories are used. Each point represents an age predicted by an individual composite trajectory that shows agreement between all three chronometer pairs. Results in the left and right panels use 50/50 and K&T fission yield descriptions, respectively. NES calculations are represented as dark blue diamonds, MLR as pink squares, and MKT as light blue circles. | 62 |
| Figure 4.16 | Combined trajectories (as described in Section 4.3, represented on the vertical axis by average Y_e) which yield chronometric agreement for each of the stars in our sample. The different beta decay rates are indicated by the marker colors as in Figure 4.14. | 65 |

| | | |
|-------------|---|----|
| Figure 4.17 | Representative theoretical abundance pattern compared to stellar and solar observations when nucleosynthesis calculations are carried out to the times indicated in each panel. The color of the squares representing the theoretical abundances indicate the set of beta decay rates used for that particular calculation, i.e. light blue for MKT and dark blue for NES. In the upper right corner of each panel, we include the weight distribution (as could be extracted from Figure 4.2) used for the specific calculation for which the abundance is shown. The stellar observational values plus their error bars are shown as black diamonds, and the solar <i>r</i> -process residuals from Asplund et al. (2009) are shown as a solid grey line. We additionally show solar <i>r</i> -process abundances as grey stars when those same data points exist for the stellar observation. We highlight the elements europium ($Z=63$), thorium ($Z=90$), and uranium ($Z=92$) with vertical dashed lines, as these were the elements we used to carry out our analysis. For each star, all data is scaled to europium... | 66 |
| Figure 5.1 | The value of β (left) and density (right) for the three different disks with decreasing field strength from top to bottom. The disks are shown at 4 ms physical time post-merger. | 71 |
| Figure 5.2 | <i>Top panel:</i> Cumulative mass ejected for each disk as a function of time. <i>Bottom panels:</i> Relative (fractional) mass ejected through r_{ex} as a function of time and angle above the mid-plane for each disk outflow. In each case, the values of the histograms sum to one. | 76 |
| Figure 5.3 | <i>Top row:</i> Distribution of electron fraction (left), and entropy (right) at t_{10} , showing total mass in each bin in units of M_{\odot} . <i>Bottom row:</i> The same as the top row but showing the fractional mass distribution. | 78 |
| Figure 5.4 | Fractional mass distributions of key properties divided into angular cuts for b10 (top row), b30 (middle row), and b100 (bottom row). The left column shows electron fraction while the right column shows entropy. | 79 |
| Figure 5.5 | <i>Top panel:</i> Isotopic mass for all three disk outflows. <i>Second panel:</i> Abundances for all three disk outflows, compared to solar (grey points). All abundances are scaled to the value of $A=120$ from b10. <i>Bottom panels:</i> Total abundance for b10 (third panel), b30 (fourth panel), b100 (bottom panel) outflows as well as the contribution from the material in each angular cut. | 81 |
| Figure 5.6 | <i>Left:</i> Ejecta mass (top, solid), lanthanide mass (middle, dashed), and actinide mass (bottom, dotted) produced in each of the angular components. The total (top) disk mass, total lanthanide (middle) mass, and total actinide (bottom) masses are shown in black for each disk. <i>Right:</i> Percent values of the contribution to the total ejecta mass (top, solid), the total lanthanide mass (middle, dashed), and the total actinide mass (bottom, dotted) for the initial value of β characterizing each disk, for each angular component. In all panels, the light, medium, and dark blue lines show the contribution from the polar, intermediate, and equatorial outflow, respectively. | 82 |
| Figure 5.7 | <i>Teal:</i> Two dimensional histograms showing the fractional mass binned by t_{ex} (x-axis, left) or $\log_{10}(X_{\text{Lan}})$ (y-axis, right) and angle above the mid-plane (vertical axis). The color map shows the fraction of the total mass, i.e. all values sum to one on each face. <i>Purple:</i> Mapping of the average entropy as a function of t_{ex} and X_{Lan} . The disks are shown with increasing β from left to right. | 84 |

| | | |
|------------|--|-----|
| Figure 6.1 | Mass radius curves for equations of state. The total sample of 2000 EoSs results in a range of $8.7 \leq R_{1.4} \leq 15.1$ and $1.89 \leq M_{\text{TOV}} \leq 3.99$ | 90 |
| Figure 6.2 | <i>Top:</i> Compilation of disk masses, as a function of the smallest NS compactness, C_1 for the 112 NR simulation points described in the text (dark squares). We show as triangles the results from the fitting formulae presented in Rad18 (dark blue, Radice et al. 2018b), KF20 (teal, Krüger and Foucart 2020), and D+20 (light blue Dietrich et al. 2020). The results from the fit proposed in Equation 6.1 are shown as pink diamonds. <i>Bottom:</i> Ratio between the masses obtained from the fit formulae to the NR data points. | 93 |
| Figure 6.3 | Inferred peak luminosity and times from the late-time, red component assuming a two-component model to explain the GW170817 electromagnetic signal (dashed vertical lines). Shaded regions highlight variation of these quantities with respect to ejecta mass from the Z12 and Z13 models of Zhu et al. (2021). The second darkest shaded region shows the region through which the peak time (top) and luminosity (bottom) overlaps, while the darkest shaded region shows the values through which both of the inferred observed quantities overlap. | 96 |
| Figure 6.4 | <i>Left:</i> Disk masses as a function of lightest neutron star compactness, C_{light} , for four binaries. <i>Right:</i> Mass-radius curves for allowed EoSs. <i>Both columns:</i> For each binary, EoSs that result in disk masses between the inferred values of $0.042 - 0.122M_{\odot}$ (indicated with dashed lines in the left column) are shown colored according to the $1.4M_{\odot}$ radius ($R_{1.4}$), as shown in the color bar. EoSs that do <i>not</i> result in masses within the aforementioned range are shown in grey for ease of comparison with Figure 6.1. | 99 |
| Figure B.1 | Quality factor for the MRI, averaged over ϕ in the midplane at 25 ms (left) and 64 ms (right) for each disk. The quality factor for the lab frame, vertical component of the magnetic field is shown as dashed lines while the comoving field is shown as solid lines. | 109 |
| Figure D.1 | Disk masses from NR simulations, shown as a function of the binary tidal deformability (left), the ratio of the total binary mass to the black hole-formation threshold mass (center), and the compactness of the smallest binary component (right). The legend indicates the sources from which each data point was extracted by the first three letters of the principal author followed by the publication year. | 117 |

CHAPTER
ONE

THE SYNTHESIS OF ELEMENTS IN THE UNIVERSE

Once upon a time, it was said that Prometheus stole fire from the gods, and the earth was formed from the flesh of the frost giant Ymir. These early stories demonstrate the persistence with which humans have identified the elements in the world around them, and sought explanations for their origins. Just as the description of the elements that make up the Universe has evolved, so too have the methods to uncover and understand the origin of these elements. In earlier times, cataloging the elements was the work of chemists and geologists, who meticulously measured the abundances of different elements in the Earth's crust. The bridge between terrestrial studies of elemental composition (see for example United States Geological Survey publications under Clarke in the late 19th and early 20th centuries) and the astrophysical origin of the elements arose with measurements of elements of sodium, magnesium, hydrogen, calcium, iron, bismuth, tellurium, antimony, and mercury in distant stars (Huggins and Miller 1864; Clarke 1873).

Early work modeling the synthesis of elements in stars was largely carried out by Fred Hoyle, who suggested that elements heavier than lithium were created via nuclear reactions in the interiors of stars (Hoyle 1946, 1954). The study of the origin of the elements became inseparable from nuclear physics following the work of Suess and Urey (1956), who linked the shell structure of nuclei to the peaked structure of the observed abundance patterns. Following this, the work of Cameron (1957) and Burbidge et al. (1957) effectively established the field of nuclear astrophysics, which examines the physical processes involved in the production of elements as a means of understanding the astrophysical origin and evolution of the chemical composition of the universe. The origin of the elements remains one of the major questions in nuclear astrophysics.

1.1 Nucleosynthesis in a Nutshell

1.1.1 Light Element Nucleosynthesis

Big Bang Nucleosynthesis

The lightest of elements were formed seconds after the Big Bang, when the universe had cooled to a point that basic nuclei could form. This idea was proposed in the 1940s, by Gamow (1946) and later in the work of Alpher et al. (1948)¹, where the authors suggested that the elements in the universe must have been formed via a “building-up” process. Protons could capture free neutrons which had not had time to decay given the short amount of time since their creation to form deuterium (a hydrogen nucleus with a single neutron). Subsequent captures would then result in the formation of heavier and heavier elements.

This model was inadequate for successfully describing the origin of the entire curve of observed abundances (see, for example, Figure 1.1). However, it remains a currently accepted mechanism for the formation of primordial hydrogen, helium, and trace amounts of lithium. While this only accounts

¹This paper represents an amusing anecdote in the history of nuclear astrophysics with the inclusion of Hans Bethe so the author list would read out the alphabetical Greek $\alpha\beta\gamma$.

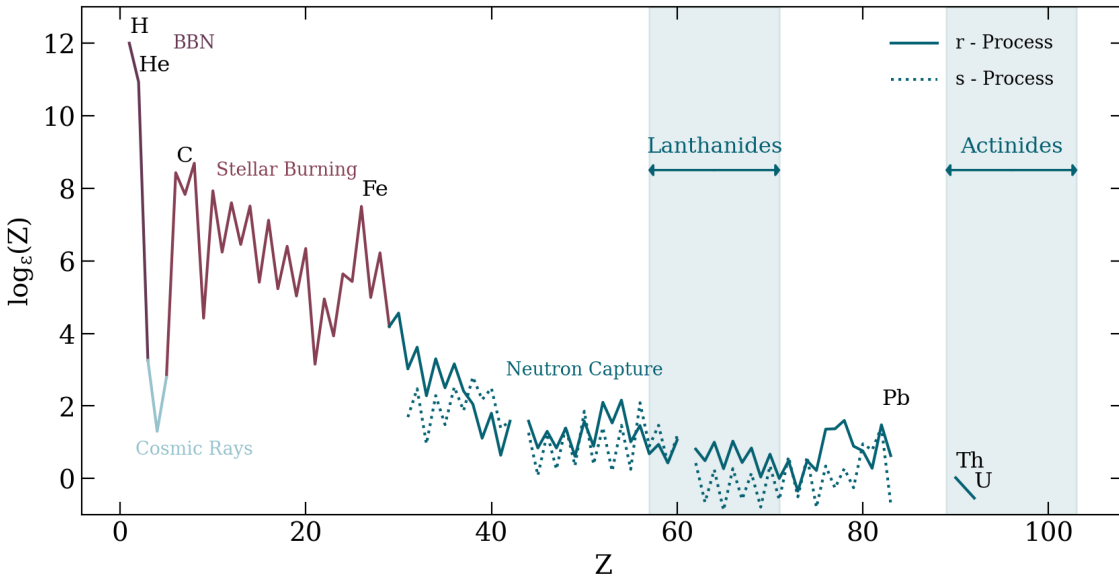


Figure 1.1: Elemental abundances of the solar system. Data is taken from Asplund et al. (2009), with *r*-process residuals computed from Arlandini et al. (1999), and is scaled following the \log_{ϵ} notation, where $N_H = 12$.

for (part of) the first three elements on the periodic table, it is worth noting that hydrogen and helium make up some 99% of the baryonic material in the universe.

Stellar Nucleosynthesis

Stars are generally defined as self-gravitating bodies undergoing nuclear reactions; the onset of nuclear fusion of hydrogen to form helium marks the point where a star “turns on” and begins the main sequence stage of its evolution. During their main sequence stage, the cores of stars exist in hydrostatic equilibrium,

Depending on the zero-age main sequence (ZAMS) mass of the star, the process of producing helium from hydrogen in the stellar core will predominantly occur through the proton-proton (p-p) chain or the carbon-nitrogen-oxygen (CNO) cycle. The p-p chain is the main source of energy for the majority of the main sequence stage of lower mass ($\lesssim 1.3 - 1.8 M_\odot$) stars with core temperatures between $\sim 4 - 15 \times 10^6$ K. The p-p chain ultimately results in the reaction



with the intermediate production of 3_2He (Bethe 1939).

In stars with larger masses ($\gtrsim 1.3 M_\odot$), where core temperatures exceed 15×10^6 K, a larger part of the energy generation comes from the production of helium via the CNO cycle, where carbon, nitrogen,

and oxygen act as catalysts:



For masses above $\sim 1.5M_\odot$ with core temperatures above about 18×10^6 K, the energy production is dominated by the CNO cycle.

The fate of a star beyond its main sequence phase is largely dependent on its ZAMS mass, with larger mass stars burning their fuel more efficiently and living shorter lifetimes on the main sequence compared to their lower mass counterparts. Low mass stars ($M < 8M_\odot$) reach the end of their lives upon exhaustion of their core hydrogen, with burning still taking place in a shell surrounding the helium ash core. If the star is sufficiently massive ($M \gtrsim 0.6M_\odot$), helium burning ignites in the core, creating carbon and oxygen, with the outer layers expanding in size and luminosity with time. The remnant of low mass stars is a white dwarf: a compressed, inert core supported by electron degeneracy pressure.

In massive stars (greater than $\sim 8M_\odot$), carbon burning paves the way for successively heavier nuclei to form, resulting in an onion-shell-like structure. Each shell is characterized by the burning of the most abundant species with the outer shell burning hydrogen, then helium, carbon, neon, oxygen, and silicon for increasingly interior shells. This process continues only to the extent that it is energetically favorable to do so: the fusion of light elements results in nuclei with slightly lower binding energy than the sum of the two parents combined. Iron-peak nuclei, however, have the highest binding energy of all elements and iron fusion cannot occur in the core.

Electron degeneracy pressure is able to support the self-gravity of the core up to the Chandrasekhar mass ($\sim 1.4M_\odot$). Photodissociation of iron-peak nuclei, $\text{Fe}(\gamma, \alpha)$ ², decreases the outward pressure triggering an initial collapse, leading to increased density and chemical potential. This facilitates electron captures on both protons and free nuclei,



and neutronization of the core, further contributing to the decrease in outward pressure and causing a rapid collapse of the core. This collapse continues until the core reaches nuclear density, at which point it is supported by neutron degeneracy pressure, and the collapse comes to a rapid halt, generating an outward shock wave, resulting in a supernova explosion. Depending on the mass of the star, the

²This abbreviated form is commonly used in nuclear physics, where $A(a,b)B$ represents the full expression $A + a \rightarrow B + b$.

remnant object is either a neutron star or black hole, with more massive ($\gtrsim 20M_{\odot}$) stars resulting in a black hole remnant.

1.1.2 Heavy Element Nucleosynthesis

The production of elements beyond the iron peak was first described in its modern form in Cameron (1957) and Burbidge et al. (1957) and relies heavily on nuclear processes governed by fundamental principles of nuclear physics. The synthesis of these elements is attributed largely to neutron capture processes, in which a nucleus, composed of neutrons and protons, captures a neutron resulting in a nucleus with larger mass number:



Complementary to the capture of one or several neutrons is the β -decay of unstable nuclei:



It is the combination of neutron captures and β -decays that allow the neutron capture process mechanism to produce a wide variety of nuclei; in rather simplistic terms, neutron capture processes can be characterized as a competition between neutron captures and the half-lives with which the unstable nuclei that are created undergo β -decay. This leads to the distinction between two major neutron capture processes: slow and rapid. While neutron capture processes are the focus of this work, additional minor processes exist. These include, for example, the rp - and p -processes which are invoked to explain the production of neutron-deficient isotopes of elements (Bildsten 1997; Schatz et al. 2001), as well as the νp -process, via which absorption of antineutrinos in a proton-rich supernova environment create neutrons which capture on neutron-deficient nuclei (Fröhlich et al. 2006).

Slow Neutron Capture Process

The slow neutron capture process (s -process) is so-called because in the framework of comparing neutron capture timescales to those of β -decay, the β -decay timescale "wins" (is shorter). The s -process occurs in environments of relatively low neutron density ($n_n \sim 10^6 \text{ cm}^{-3}$) over extremely long timescales. The s -process operates mostly in the late-life stages of low- to intermediate-mass stars (see, for example, Gallino et al. 1992; Straniero et al. 1995; Gallino et al. 1998; Busso et al. 1999; Pignatari et al. 2010) during the asymptotic giant-branch (AGB) phase of their lives, as well as in the helium and carbon burning stages of massive stars. It is characterized by the slow, steady building of heavy nuclei along the valley of β -stability.

The peaks in the s -process pattern, which can be seen in the dashed lines of Figure 1.1, reveal fundamental nuclear physics properties. Nucleons (the collective term for neutrons and protons) fill discrete energy levels in the nucleus in a manner analogous to the way electrons fill valence shells in atoms. Certain numbers of protons and neutrons represent so-called "magic" numbers. Continuing with

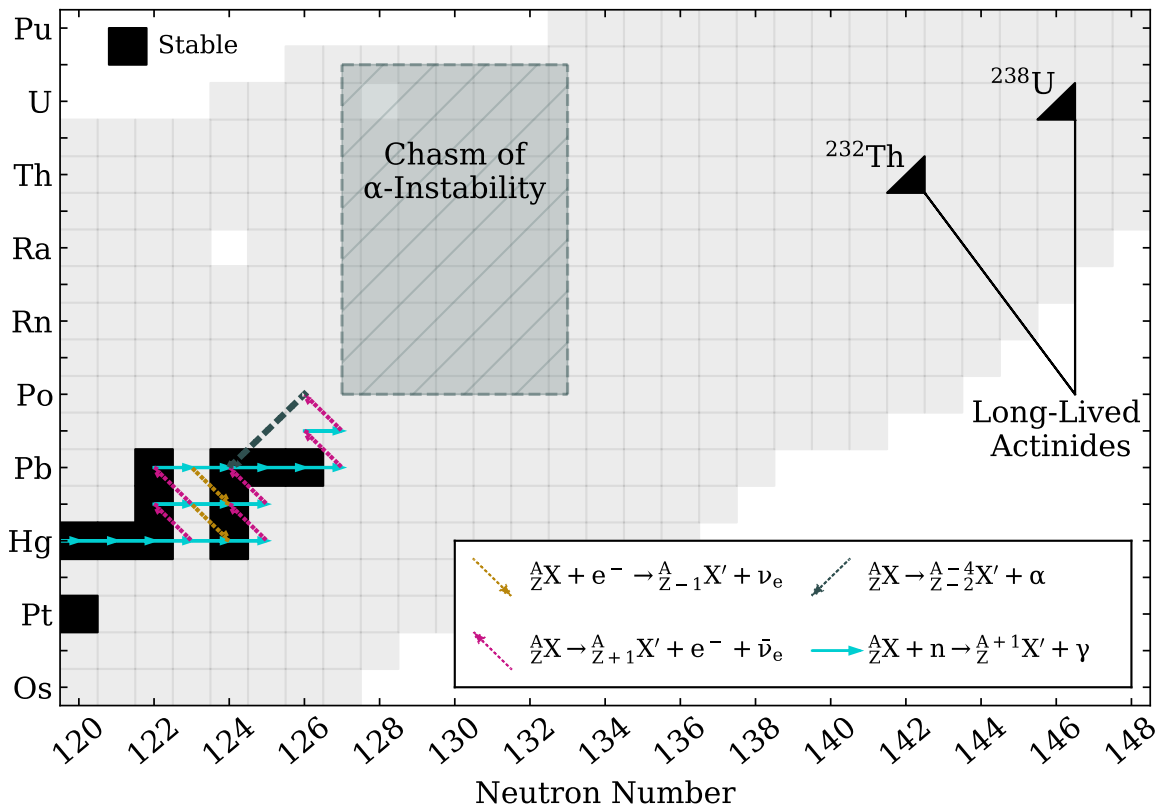


Figure 1.2: Termination region of the *s*-process in relation to the long-lived isotopes of thorium and uranium, highlighting the “Chasm of α -Instability”.

the analogy of valence electrons, these magic numbers represent shell closures that result in particularly stable configurations of nuclei. For neutrons in heavy elements nucleosynthesis, these magic numbers occur at $N = 50, 82$, and 126 (Mayer 1948). The result of a nucleus with a filled neutron shell, or close to a filled shell, is a more tightly bound nucleus with a significantly reduced neutron capture cross-section. This reduced cross-section slows down the neutron capture process, causing a pile-up of material, which in turn results in an increased abundance along isobars of the closed shells. Given that the *s*-process proceeds close to the valley of β -stability, the resulting peaks lie close to these shell closures, around $N = 50, 82$, and 126 .

The *s*-process terminates near isotopes of lead ($Pb, Z=82$) and bismuth ($Bi, Z=83$), at the upper edge of the valley of β -stability, as is shown in Figure 1.2. The nucleus resulting from the capture of a neutron onto ^{208}Pb has an extremely long half-life of 2×10^{19} years (de Marcillac et al. 2003); despite being radioactive, it is long-lived enough to be part of the *s*-process. However, subsequent neutron capture and β -decay produces a nucleus of ^{210}Po , which undergoes α -decay into the stable isotope ^{206}Pb , thus terminating the *s*-process path.

1.2 Rapid Neutron Capture Process

One of the most glaring shortcomings of the *s*-process mechanism is its inability to produce the long-lived actinides: ^{232}Th and ^{238}U , whose half-lives are roughly 14 and 4 Gyr, respectively. They are present in the Sun, the Earth's crust, stars in the Milky Way, and certain glazed dinnerware produced between the 1930s and 1970s (Buckley et al. 1980).

In particular, the termination point of the *s*-process lies at the beginning of the Chasm of α -Instability³, as can be seen by the large light blue patch of Figure 1.3. Nuclei in this region, highlighted in both Figures 1.2 and 1.3, are unstable to α -decay on very short timescales ($\mathcal{O}(\text{ns-ms})$), thus inhibiting any build-up of material by neutron captures on slow timescales. This problem is rather simply solved by the capture of neutrons on a timescale that is *rapid* compared to the β -decay timescale. This is the basic idea behind the rapid neutron capture process, or *r*-process, which is the main topic of this work.

In its most basic form, the *r*-process consists of several, successive neutron captures onto a single nucleus. This is made possible in an environment of extremely high neutron density ($n_n \gtrsim 10^{20} \text{ cm}^{-3}$), accompanied by high temperature and entropy. In these extreme environments, seed nuclei rapidly capture neutrons to produce extremely neutron-rich nuclei, up until the point that the photo-dissociation rate equals that of the neutron capture rate, at which point the system exists in $(n, \gamma) \rightleftharpoons (\gamma, n)$ equilibrium. Eventually, the free neutrons become depleted, slowing down the capture rate compared to the rate of decays of the heavy nuclei produced. This “freeze-out” sets the abundance pattern that subsequently decays, effectively locking in the resulting abundance of isotopes along the path toward stability.

The “neutron-richness” of the material as it undergoes nucleosynthesis is often described by the electron fraction, or Y_e :

$$Y_e = \frac{n_p}{n_p + n_n}, \quad (1.12)$$

representing the proportion of free protons (n_p) to total baryons ($n_p + n_n$). A smaller Y_e therefore represents a larger proportion of free neutrons to protons. In cases where this quantity is especially low ($\lesssim 0.2$), the *r*-process path produces such heavy nuclei ($Z \gtrsim 90$) that they become unstable to fission. If this occurs while neutron capture rates are high, the resulting fission daughter products become seed nuclei for the *r*-process. Similarly, high-mass nuclei whose decay chains terminate near the aforementioned Chasm are, of course, susceptible to α -decay. Thus the rapid neutron capture process, though facilitated by neutron captures and β -decays, is, in reality, a menagerie of nuclear processes taking place in an extreme environment.

1.3 Astrophysical Sites of the *r*-Process

The extreme environments required for the *r*-process to occur have led to many hypotheses about where such conditions might exist. Given the short lifetime of the neutron (~ 15 minutes in vacuum),

³At the time of writing, the author could not find an official name for this region of the chart of the nuclides, so has taken the liberty of bestowing a name herself.

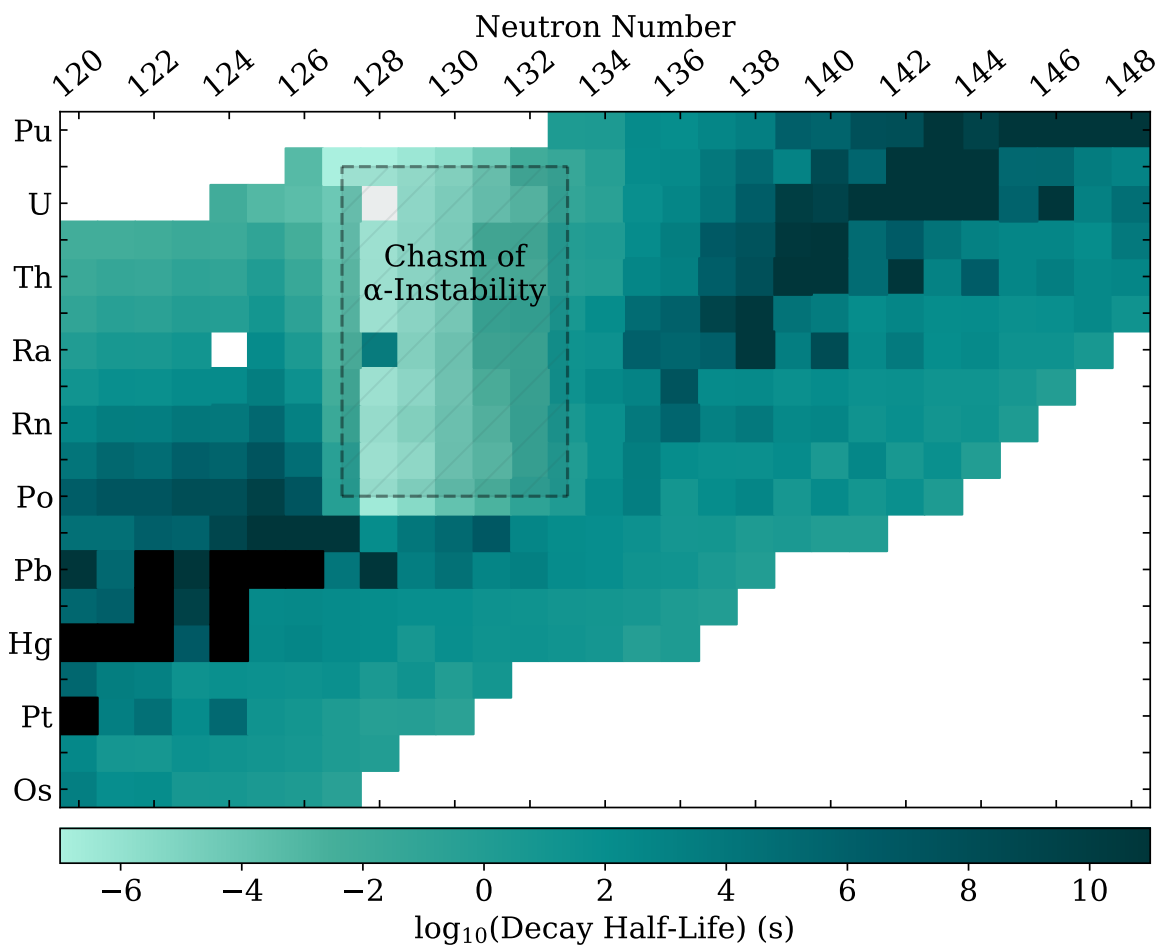


Figure 1.3: Decay rates of nuclei at the termination point of the *s*-process and beyond. Data taken from Kondev et al. (2021). Darker shades represent nuclei with longer half-lives.

the most basic requirement of a high neutron-to-seed ratio necessitates a transient environment in which neutrons can be produced in necessarily high quantities. This section describes some of the historically significant and currently accepted candidates for such sites.

1.3.1 Supernovae

The original proposed scenario capable of producing the conditions conducive to *r*-process nucleosynthesis date back to the inception of the field of nuclear astrophysics itself (Cameron 1957; Burbidge et al. 1957). It was proposed that core-collapse supernovae (CCSNe) could provide the necessary conditions. One of the earliest time-dependent calculations modeling the *r*-process in a supernova environment is the work of Seeger et al. (1965), where the solar system abundance pattern was attributed to a superposition of nucleosynthesis events occurring on different timescales but ultimately concluding that no single event could produce all three peaks.

Later, it was proposed that the high-entropy neutrino-driven wind of a core-collapse supernova could be the production site of the *r*-process. Work carried out in the 1990s largely supported this idea through detailed nucleosynthesis calculations and hydrodynamic modeling (Woosley and Hoffman 1992; Meyer et al. 1992; Takahashi et al. 1994; Woosley et al. 1994; Qian and Woosley 1996; Wanajo et al. 2001). CCSNe as the leading production site for the full *r*-process subsequently began to fall out of favor, partially due to the incorporation of more detailed neutrino physics (as well as more detailed hydrodynamics) showing them to be unlikely to be able to produce the conditions necessary to produce the full *r*-process pattern (Thompson et al. 2001; Arcones et al. 2007; Fischer et al. 2010; Hüdepohl et al. 2010; Martínez-Pinedo et al. 2012; Roberts et al. 2012).

Despite the disfavoring of CCSNe as a primary production site of the *r*-process, it is still thought that some light *r*-process elements could be produced in these environments (Thompson et al. 2001; Wanajo et al. 2011; Arcones and Thielemann 2012). Furthermore, recent years have seen the suggestion of rare types of supernovae that could theoretically be capable of synthesizing some *r*-process material.

Magnetorotationally-driven supernovae are commonly referred to as MHD supernovae due to the use of magnetohydrodynamical (MHD) simulations to study their behavior. These supernovae are characterized by strong magnetic fields ($\mathcal{O}(10^{12}\text{G})$) and rotation that affect the dynamics and morphology of the outflow. Work carried out in recent years indicate that heavy *r*-process nucleosynthesis can take place immediately following core-bounce, in late-time ejecta, or even in the high entropy jets formed by the funneling of the strong magnetic fields (Symbalisty et al. 1985; Burrows et al. 2007; Winteler et al. 2012; Thielemann et al. 2017; Mösta et al. 2018; Reichert et al. 2021; Obergaulinger and Aloy 2022; Reichert et al. 2022; Bugli et al. 2023; Powell et al. 2023; Reichert et al. 2024, and many, many more).

It has also been proposed that heavy element nucleosynthesis could occur in the material surrounding the nascent black hole following the collapse of a rapidly rotating massive star, with the event and resulting system termed *collapsar*. It is thought that the accretion disk formed by the post-bounce fall-back material fosters similar conditions to accretion disks formed after a compact object merger event (discussed in the next section), which are favorable to heavy element nucleosynthesis (MacFadyen

and Woosley 1999; Surman and McLaughlin 2004; Kohri et al. 2005; Surman et al. 2006; Rockefeller et al. 2008; Siegel et al. 2019; Miller et al. 2020).

Both MHD supernovae and collapsars are exotic supernovae, and are considered to be quite rare. It is estimated that perhaps only a fraction of 1% of massive stars develop the right combination of strong magnetic fields and rapid rotation. It has also been suggested that these types of events could have been more prevalent earlier in the history of the Universe (Woosley and Heger 2006). Contrarily, recent claims have been made that despite the rarity, these types of events are such effective producers of heavy materials, that they are capable of having produced more than 80% of the galactic *r*-process material (Siegel et al. 2019). Whether these exotic supernovae remains promising candidates remains a point of debate amongst the community, and have neither been confirmed nor completely ruled out.

1.3.2 Compact Object Mergers

The year in which this dissertation was written marks 50 years since the proposal of compact object mergers as a candidate site for heavy element nucleosynthesis. Lattimer and Schramm (1974)⁴ suggested that the coalescence of a neutron star and a black hole would result in the tidal disruption of the neutron star, and that heavy element nucleosynthesis could take place in this tidal ejecta. The merger of two neutron stars, although mentioned in these first papers, was developed later by Symbalisty and Schramm (1982). Binary neutron star mergers as a source for the *r*-process became especially relevant in light of the detection of the orbital decay of PSR B1913+16, the first ever detection of binary pulsar system⁵ (Hulse and Taylor 1975a,b).

The physics involved in compact object mergers continued to develop over subsequent decades, both in terms of the potential for detection of gravitational radiation and in terms of the prospects for *r*-process nucleosynthesis in the ejecta. It was recognized that these coalescence events would be exciting targets for future gravitational-wave detectors. Li and Paczyński (1998) also proposed that an optical transient powered by the radioactive decay of the heavy elements synthesized in the merger could be detectable in supernova searches. This electromagnetic (EM) transient earned two names. The first, earlier term was suggested in Kulkarni (2005) to be a *macronova*, as the energetics of the light curve were expected to resemble a supernova, but with a brightness somewhere between a classical nova and a supernova. Eventually, this terminology lost out in popularity to *kilonova*, which carried with it a more precise indication of the expected peak luminosity being roughly 1000 times that of a classical nova (Metzger et al. 2010).

The gravitational-wave detection of the neutron star merger GW170817 plus the associated transient signals observed across the EM spectrum (AT 2017gfo) represented a major multi-messenger detection that resulted in a wealth of data that is still being analyzed to this day (Abbott et al. 2017b,c,a; Chornock et al. 2017; Goldstein et al. 2017; Nicholl et al. 2017; Savchenko et al. 2017; Soares-Santos et al. 2017; Villar

⁴This paper is often cited side-by-side with Lattimer and Schramm (1976), in which the idea is further developed.

⁵Later taking on the name of the Hulse-Taylor binary after its discoverers who were awarded the 1993 Nobel Prize for this discovery.

et al. 2017, and several others). This combined observation has lent the most support to the radioactively powered kilonova light curve. In particular, the long-lived, long-wavelength part of the light curve points to the production of atomically complex (and therefore high opacity) lanthanides (Cowperthwaite et al. 2017; Drout et al. 2017; Kilpatrick et al. 2017; Perego et al. 2017; Pian et al. 2017, see Section 1.4.3 for further discussion).

While this historical observation lends a great deal of support to neutron star mergers as r-process-producing sites, and despite the scrutiny with which it has been studied over the last few years, much remains unknown. For example, it is unknown whether there is variety in kilonova signals or whether this represented a “typical” kilonova. Furthermore, the question remains whether *r*-process material produced in neutron-star mergers is sufficient to explain galactic abundances, or whether other, more exotic sites are needed (see the discussion of exotic supernovae above). The role of neutrinos and such effects as flavor oscillation or energy transport remain unclear in the context of compact object mergers (including but not limited to Richers et al. 2015; Malkus et al. 2016; Perego et al. 2016; Zhu et al. 2016; Miller et al. 2019a; Froustey et al. 2024; Padilla-Gay et al. 2024).

There also remains the nature of the conditions during and after the merger event, and to what extent nucleosynthesis occurs in different parts of the merger such as the material squeezed out of the contact interface between the two stars or the accretion disk surrounding either a hypermassive neutron star or black hole remnant. Different sites within the merger itself are generally thought to have different levels of effectiveness at producing a full *r*-process pattern. These different “sites” correspond to different channels of mass ejection, and are often invoked to explain different components to the light curve (Perego et al. 2017; Kasen et al. 2017; Waxman et al. 2018). The broadest classification scheme usually consists of *dynamical* and *secular* ejecta.

Dynamical Ejecta

Material that is ejected *during* the merger of two compact objects occurs on *dynamical* timescales. On these timescales, the outflow of material is primarily driven by two main mechanisms. The first mechanism involves the rapid expulsion of material through tidal interactions, which tear apart the neutron star(s) and result in the earliest outflows. The second mechanism, occurring on similar timescales, involves the generation of shocks during and after the merger when the surfaces of the neutron stars touch, leading to material being expelled from the contact interface. The initial tidal ejecta is characterized by a very low Y_e (~ 0.1) and tends to be confined to regions closer to the orbital plane. Conversely, the shock-driven outflow occurs slightly ($\mathcal{O}(\text{ms})$) later, and consists of material with higher entropies and Y_e .

Combined, these outflows exhibit characteristic velocities ranging $0.1 \leq v/c \leq 0.3$, where c is the speed of light. They encompass a range of electron fractions, spanning from very low values ($Y_e \sim 0.1$) to relatively higher ones, particularly within the context of robust *r*-process nucleosynthesis ($Y_e \gtrsim 0.25$). There is a broad consensus regarding the favorable conditions for *r*-process nucleosynthesis occurring in material ejected via tidal tails. This is less clear for the shock-driven ejecta, especially for calculations

which account for weak interactions driving the Y_e up sufficiently to significantly reduce the amount of r -process produced (Wanajo et al. 2014; Goriely et al. 2015; Foucart et al. 2016; Radice et al. 2016; Martin et al. 2018; Kullmann et al. 2021). However, uncertainties persist regarding whether the mass of the ejected material alone is sufficient to account for the observed r -process abundances in the Galaxy, with estimates of the total dynamical ejecta ranging between $10^{-4} M_\odot < M_{\text{dyn}} < 10^{-2} M_\odot$ (Rosswog et al. 1999; Bauswein et al. 2013b; Hotokezaka et al. 2013a; Dietrich and Ujevic 2017; Radice et al. 2018b).

Secular Ejecta

The system following the inspiral and merger of two neutron stars consists of a central remnant surrounded by an accretion disk. Mass ejected on these later timescales, up to a few seconds, is dominated by winds driven off the remnant and disk (Dessart et al. 2009; Fernández and Metzger 2013). The nature of the central remnant is determined largely by the binary mass and properties of the nuclear equation of state (EoS). Binaries with total mass below M_{TOV} ⁶ result in stable neutron star remnant. There exists a theoretical mass above which the system will undergo direct collapse to a black hole; this so-called *threshold mass* is a quantity predicted by the EoS, and expected to be roughly 1.3-1.7 times larger than M_{TOV} (Bauswein et al. 2013a; Shibata and Taniguchi 2006; Hotokezaka et al. 2011). For binaries with masses below this threshold mass but above M_{TOV} , the system could be left with a rotation-supported hypermassive or supramassive neutron star possibly existing for up to tens of ms before collapsing (Sekiguchi et al. 2011; Hotokezaka et al. 2013b; Fujibayashi et al. 2023; Just et al. 2023).

Initially, the disk exhibits high accretion rates and large amounts of thermal neutrinos which carry away a small amount of mass from the disk surface in the form of a neutrino-driven wind (Popham et al. 1999; Ruffert et al. 1997; McLaughlin and Surman 2005; Surman et al. 2008; Perego et al. 2014). As the disk evolves, transitioning from neutrino-cooled to radiatively inefficient states, significant outflows occur, driven by viscous turbulent heating, nuclear recombination (Beloborodov 2008; Lee et al. 2009; Metzger et al. 2009; Fernández and Metzger 2013), and magnetic field effects. In particular, MHD turbulence, generated by the magnetorotational instability (Velikhov 1959; Balbus and Hawley 1991), can be responsible for large outflows of up to 40% of the initial disk mass (Fernández et al. 2018; Christie et al. 2019; Sprouse et al. 2024). Though sensitive to the conditions of the initial binary system, typical disk masses are expected to range from $\sim 10^{-2} M_\odot$ to a few tenths of a solar mass (Oechslin and Janka 2006), thus resulting in the disk alone potentially being capable of an outflow mass on the order of a few hundredths of a solar mass ($\mathcal{O}(10^{-2})$). It is becoming more and more apparent that outflows from the post-merger system represent an important component of the ejecta, thanks both to the large amounts of material ejected as well as the favorable conditions for r -process nucleosynthesis. It has been proposed that the post-merger system alone could be capable of producing the entire observed r -process pattern (Wu et al. 2016).

⁶Shorthand for the maximum mass of a cold non-rotating neutron star, with the subscript referring to the upper limit of the mass as given by the Tolman-Oppenheimer-Volkoff (TOV) equations (Oppenheimer and Volkoff 1939).

1.4 Astrophysical Signatures of r-Process Nucleosynthesis

As discussed at the beginning of this chapter, the detailed cataloguing of the elements as they occur on Earth and in the Universe is a practice that goes back more than a century. However, the identification of the *r*-process as a unique source of element production introduces the question of the source of the *r*-process elements and the identification of *r*-process signatures in the solar system and beyond. This section describe some of these astrophysical signatures.

1.4.1 Solar and Solar System Abundances

Given that the *s*-process proceeds close to stability, the nuclei involved are significantly easier to study than nuclei far from stability. For this reason, models of the *s*-process can be used to estimate its contribution to abundance patterns found in the solar system. From this contribution, the remainder is generally attributed to the *r*-process, yielding the *r*-process residual. These two different contributions can be seen in Figure 1.1 as a solid (*r*-process) and dashed line (*s*-process), with the separate lines obtained by the method described above. The abundance pattern itself consists of data from Asplund et al. (2009), while the *s*-process contribution to that abundance pattern is from Arlandini et al. (1999). The remainder, shown as a solid line, is taken to be the *r*-process contribution to the solar pattern. Two independent but complementary methods are used to determine the solar system abundance, and are discussed below.

Solar Abundances

Measurements from the Sun are obtained via photospheric line absorption spectroscopy. As radiation photons are emitted from the Sun's outer convective layer, they can interact with heavy ions and atoms that exist in the photosphere, leaving dark absorption lines in the resulting spectrum. By measuring and identifying these lines, relative abundances can be inferred (Lodders 2003; Asplund et al. 2009).

It should be noted that while this method is the most widely used for determining the chemical composition of the Sun, and is the best method to date, it comes with a number of challenges. In particular, *r*-process elements that exist within the solar atmosphere exist in quantities that are orders of magnitude smaller than those of, for example, hydrogen and helium. This can result in absorption lines from heavy elements being comparatively faint and difficult to distinguish. The diversity of elements in the Sun, and their respective diversity of ionization states, results in an incredibly rich spectrum, from which it can be difficult to distinguish distinct lines. The interpretation of absorption lines, even given perfect observing conditions, is subject to models of complex atomic and molecular transitions as well as models of the solar atmosphere itself. This can lead to potentially large uncertainties, especially in the context of the highly complex lanthanides and actinides produced via the *r*-process. Furthermore, very little *isotopic* information is available from the Sun alone.

Meteoric Abundances

One of the primary sources of meteoric abundances are obtained from chondrites- stony meteors formed from pre-solar grains whose composition remains roughly unchanged from the time of their formation to the present. As such they provide excellent probes of the early composition of the solar system⁷. Meteoric abundances offer the opportunity to obtain high precision isotopic abundances. However, they are comparatively lacking (compared to solar values) in key elements, namely H, C, N O, and noble gases, as these ultra-volatile elements readily form gaseous compounds. With these exceptions, and for the majority of elements measured in both the Sun and meteors, the inferred abundances agree to within $\sim \pm 10\%$ (Asplund et al. 2009; Lodders et al. 2009).

1.4.2 Metal-Poor Stars

At less than 5 billion years old, the Sun is a relatively young star. This is reflected in its complex chemical composition. The presence of a wide range of elements is not linked to the production of those elements in the Sun, but to the presence of those elements when the Sun was formed. The material that formed the Sun was "contaminated" by the products of the previous ~ 9 billion years of nucleosynthetic events. Hence each new generation of stars bears the chemical compositions of stars that came before.

Under this model, stars with lower metal⁸ content than the Sun are metal-poor, while stars with similar metal content to the Sun are metal-rich. Due to the numerous spectral lines detectable from iron (Fe, Z=26) transitions, and their relative ease of detection, the "metallicity" is generally characterized by the relative amount of iron to hydrogen (H) compared to the Sun. This ratio, and indeed the ratio of any element (A) to element (B) relative to the ratio of the same two elements in the Sun, can be expressed with the bracket notation:

$$[A/B] = \log_{10} \left(\frac{n_A}{n_B} \right)_* - \log_{10} \left(\frac{n_A}{n_B} \right)_\odot, \quad (1.13)$$

where the * (\odot) subscript refers to the stellar (solar) values. However, it is often less useful to compare chemical signatures in stars to the Sun and more useful to compare relative abundances of different elements within a single star. For this purpose, the " \log_ϵ " notation is used to denote the number of atoms of element A with respect to those of hydrogen (H), in the star:

$$\log_\epsilon(A) = \log_{10} \left(\frac{n_A}{n_H} \right) + 12, \quad (1.14)$$

such that the abundance of hydrogen (n_H) is kept constant at 10^{12} .

For the classification by iron content, current observations of stars have yielded values of [Fe/H] spanning roughly seven orders of magnitude. This scale includes stars with roughly five times the

⁷An idea that goes back to the 18th century, when the "father of meteorics" proposed that fireballs from the sky could be explained by rocks burning up in the atmosphere, much to the consternation of his contemporaries (Chladni 1794; Marvin 1996).

⁸It should be noted that anything heavier than helium (Z=2) is considered to be a metal in astronomy. Therefore a star with any signature of an element heavier than helium has "metals".

Table 1.1: Classification criteria of low-metallicity stars as relevant for this body of work. It should be noted that, although not listed here, the prefixes used to describe metal-poorness extend to “Giga-metal-poor”, where $[Fe/H] < -9.0$, followed by “Ridiculously metal-poor”, for which no observations exist (Frebel 2018).

| Classification | Criteria |
|----------------------|--|
| Metal-poor | $[Fe/H] < -1.0$ |
| Very metal-poor | $[Fe/H] < -2.0$ |
| Extremely metal-poor | $[Fe/H] < -3.0$ |
| limited-r | $0.3 < [Eu/Fe]$ |
| r-i | $+0.3 < [Eu/Fe] \leq +0.7^9$ |
| r-ii | $+0.7 < [Eu/Fe]$ |
| Actinide-boost | $\log_{\epsilon}(\text{Th/Dy}) > -0.9$ |

solar metallicity (Ness et al. 2013) as well as stars with non-detections of iron. These non-detections provide something of an experimental lower limit of $[Fe/H] < -7.1$ (Keller et al. 2014). Due to their low metallicities, metal-poor stars that are enriched with *r*-process material offer an excellent window to studying these signatures. *r*-process enhancement is determined by the amount of europium (Eu, Z=63) with respect to iron, as europium is considered an “*r*-process only” element (one that is almost entirely produced via the *r*-process). When the iron abundance in the star is on the order of 100 times smaller than the Sun ($[Fe/H] < -2$), but the europium to iron abundance is larger than that of the Sun ($[Eu/Fe] > +1$), the star falls into the category of metal-poor *and* *r*-process-enhanced. Detections of these *r*-process enhancements have increased significantly over recent years; to date, there are more than 300 metal-poor, *r*-processed enhanced stars (Holmbeck et al. 2020a).

Furthermore, a subset of these metal-poor, *r*-process enhanced stars exhibit signatures of actinides. Given the extremely old age of the stars in which these signatures occur (by the same metallicity-age relation), the detection of actinides is interpreted as the detection of two specific isotopes: ^{232}Th and ^{238}U , as these are the longest-lived actinide isotopes (highlighted in Figure 1.2). Of these, uranium (U) lines tend to be the most difficult to detect due to strong blending with neighboring iron or lanthanum (La) lines (Kramida et al. 2023; Shah et al. 2023). This difficulty is so great, in fact, that only five *r*-process enhanced, metal-poor stars have reliable¹⁰ measurements of uranium. The abundance patterns of these stars are shown in Figure 1.4.

1.4.3 Compact Object Mergers and Kilonovae

The observational evidence of *r*-process elements discussed thus far have been indicative of the existence of *r*-process events occurring in some cosmic past. Though they have been detections of the elements

⁹As with many conventions, the limits of these classifications change with time and evolving data. Here, 0.7 is designated as the upper limit following the suggestion of Holmbeck et al. (2020a), rather than the previously-used upper limit of 1.0.

¹⁰CS22892 (Sneden et al. 2003) is a metal-poor, *r*-process enhanced star, but only has an upper limit of a uranium detection so if not usually used in analyses involving uranium.

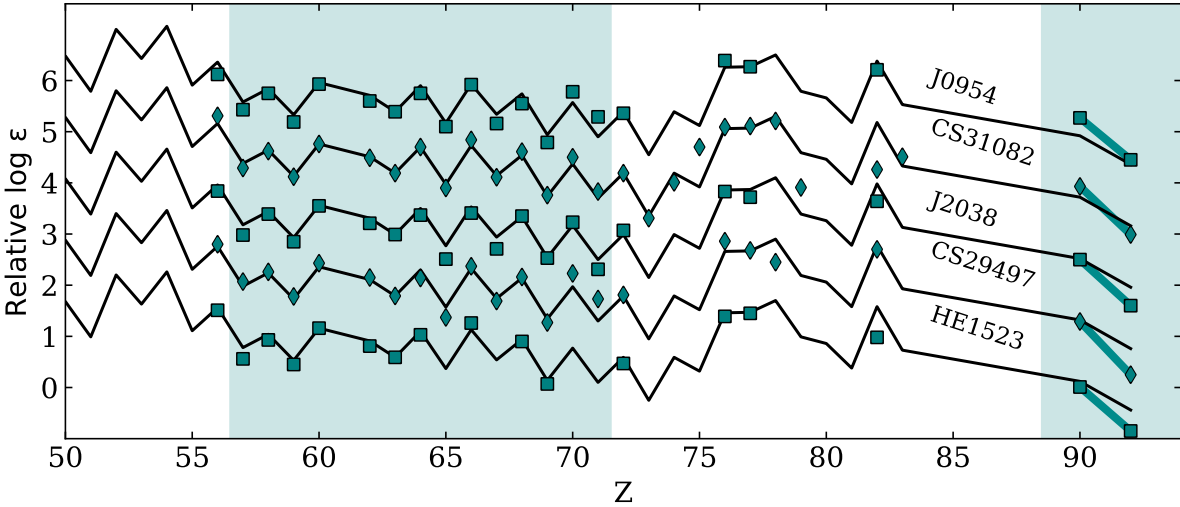


Figure 1.4: Scaled abundances of five metal-poor, r -process enhanced stars selected for their uranium abundances. The solar r -process abundances pattern is shown as a black line.

produced via the r -process, one would not generally consider them to be detections of r -process-producing events, or indicative of *freshly* synthesized material.

The multi-wavelength observations following GW170817 saw a distinctive optical and infrared signature characterized by a rapid rise in brightness followed by a gradual decline over several days to weeks (Chornock et al. 2017; Cowperthwaite et al. 2017; Tanvir et al. 2017; Villar et al. 2017). This gradually declining, longer-wavelength component is consistent with the presence of high-opacity lanthanides in the ejecta (Barnes and Kasen 2013; Kasen et al. 2017) and provides the strongest evidence of an abundance pattern that reaches lanthanide production. Estimates of the lanthanide-bearing ejecta resulting from this merger predict roughly $5 \times 10^{-2} M_{\odot}$ of lanthanide-bearing ejecta (Cowperthwaite et al. 2017; Villar et al. 2017)¹¹.

While it is broadly accepted that lanthanides were produced in the merger event, little information has been gleaned about the exact composition of the ejecta. Features centered around 1.48 and 1.75 μm (near-infrared, NIR) are attributed to spectral lines of Cs I ($Z=55$) and Te I ($Z=52$), and indicate production of light r -process elements (Smartt et al. 2017). Further claims have been made regarding the detection of a residual spectral feature around 8000 Å, attributed to the presence of Sr ($Z=38$) (Watson et al. 2019). While these claims of detections of specific elements remains inconclusive, they lend further support to the production of r -process elements in the merger event. Evidence for actinide and superheavy element production from neutron star mergers also remains inconclusive (Kasliwal et al. 2022), but represents an exciting theoretical and observational prospect (Holmbeck et al. 2018b; Chen and Liang 2023; Holmbeck et al. 2023a).

¹¹This mass corresponds to a two-component (red+blue) model. The expected mass is smaller when a third “purple” component is accounted for in the model.

CHAPTER
TWO

METHODS AND TECHNIQUES

2.1 Nuclear Data

As discussed in Chapter 1, the r-process is characterized by successive reactions and decays (*nuclear trajectories*) occurring far from β -stability. The properties of nuclei that exist on the neutron-rich side of, and far from, β -stability must be estimated if they are to be used for nucleosynthesis calculations. The mass of a nucleus is perhaps its most fundamental property and is directly related to its binding energy per nucleon, which plays a large part in determining its half-life.

Numerous methods exist for predicting the masses of nuclei, generally falling somewhere on a scale between microscopic and macroscopic. Here, micro- or macroscopic refers to the treatment of nuclei in the model; microscopic models lean more heavily on a description of the nucleus based on nucleon-nucleon interactions of the individual nucleons of which it is composed (for example the Hartree-Fock-Bogoliubov (HFB) models used by Goriely et al. 2009, 2013a,b). More macroscopic models, on the other hand, characterize the nucleus based on larger scale behaviour and global properties. While the former tends to be based on, for example, quantum mechanical effects and first-principles physics, the latter tends to be more based on empirical or semi-empirical observations. In practice, most models are described by a microscopic-macroscopic approach where one starts with a macroscopic model then adds microscopic corrections (for example the commonly-used Finite-Range-Droplet Model- FRDM Möller et al. 2015).

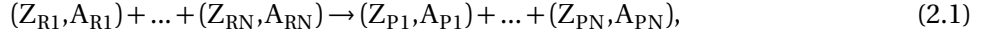
However one might describe the method used to obtain the model, it is generally true that theoretical models are compared to experimental data, with the “success” of a model usually tied to how well it predicts measured nuclear properties. Given that the nuclear physics far from stability is largely unknown, it should be noted that a reasonable fit to experimental data is not a guarantee that a theoretical model will accurately describe nuclei far from stability.

The nucleosynthesis aspects of the works contained herein are carried out with “self-consistent” nuclear data. Given the influence of the nuclear mass on all other reaction and decay properties, theoretical data is computed to be consistent with the theoretical mass model (Mumpower et al. 2016a,b, 2018; Zhu et al. 2021). This involves a number of considerations, including:

- Calculation of the single neutron separation energies, S_{1n} , which impact neutron capture, photodissociation rates, and beta-delayed neutron emission probabilities
- Calculation of the β -delayed neutron emission probabilities, which is especially relevant for nuclei very far from stability
- Calculation of Q-values used in post-processing for the purpose of converting abundance changes to nuclear heating rates

2.2 Nuclear Reaction Networks

State of the art nuclear reaction networks (Lippuner and Roberts 2017; Sprouse et al. 2021; Reichert et al. 2023) are computational tools that track the evolution of elemental abundances and energy generation in a medium via thousands of nuclear reactions and decays. Mainly, for a process described by the conversion of N reactants (R) into N products (P), i.e.



one can write the following set of differential equations :

$$\{\forall i \in \{R1, \dots, RN\} : \frac{dY(Z_i, A_i, t)}{dt} = \lambda(t) \rho^{N-1} \prod_{j=R1, \dots, RN} Y(Z_j, A_j, t)\}, \text{ and} \quad (2.2)$$

$$\{\forall i \in \{P1, \dots, PN\} : \frac{dY(Z_i, A_i, t)}{dt} = P(i) \lambda(t) \rho^{N-1} \prod_{j=R1, \dots, RN} Y(Z_j, A_j, t)\}. \quad (2.3)$$

Here $\lambda(t)$ represents the rate of a given reaction as a function of time and possibly temperature, ρ is the density of the material, and $P(i)$ is the probability that species (Z_i, A_i) will be produced. By solving this set of equations over all processes occurring at each timestep, the number abundance (Y) of a species with proton number (Z) and mass number (A) can be computed as a function of time (Sprouse et al. 2021).

Thus it is possible to simulate nuclear trajectories given some set of nuclear data and thermodynamic conditions on which these data might depend. Useful quantities which emerge from these simulations include the abundance as a function of time as well as the change in abundance, the so-called "flow", which tracks the changing species by reaction type. From these two quantities, it is possible to construct other useful quantities, including the mass fraction of lanthanides or actinides as a function of time, nuclear heating rates, late-time abundances, etc., depending on the end goal of the simulation output.

2.2.1 PRISM

The parts of this work which call for the tracking of nuclear abundances are carried out using the Portable Routines for Integrated nucleoSynthesis Modeling (PRISM, Sprouse et al. 2021), a nuclear reaction network code written in object-oriented Fortran.

PRISM is a stand-alone network that follows nuclear reactions and decays in a system that is assumed to be closed, i.e. no nuclei leave or enter the system. Furthermore, it assumes that the velocity and position distribution of the material undergoing nucleosynthesis is uniform, i.e. there is no inhomogeneous expansion or fluid mixing. This is in contrast to networks that are designed to run in-line with a different simulation, e.g. a hydrodynamics simulation. These are usually more targeted to a specific group of reactions relevant to the system being studied. Below are some key considerations when using PRISM to perform nucleosynthesis that are intended to serve as a general reference. The reader is

directed to the software manual for more detailed descriptions regarding installation requirements, input file formatting, etc.

Nuclear Data Input

The most basic ingredient required for a nuclear reaction network is a description of the nuclear processes involved. The way in which these processes are incorporated into the network, and the information required for them, depends on which of four categories listed below best describes the process itself. It should be noted, first, that one of the greatest benefits of PRISM is its flexibility in accepting nuclear data. PRISM uses a hierarchically-sorted input control file where the nuclear data the user wishes to use is listed. Thus a deliberate construction of this input file can prompt PRISM to begin with the most extensive set of theoretical rates spanning as much of the chart of nuclides as possible (or reasonable), then overwrite successively with a self-consistently calculated set of theoretical rates, followed by measured data. This is especially useful if one is interested in investigating the rate of a particular decay or region that is unmeasured.

Decays: A decay process is characterized by the properties of the nucleus itself rather than external factors (such as temperature or density), and by having a well-defined set of daughter products from the decay. Nuclei that undergo decays are characterized by their half-life, or the time required for an initial number, N_0 of nuclei to be decreased by a factor of two:

$$N(t) = N_0 \left(\frac{1}{2} \right)^{\frac{t}{t_{1/2}}}, \quad (2.4)$$

where the half-life, $t_{1/2}$, is related to the rate of decay, λ by

$$t_{1/2} = \frac{\ln(2)}{\lambda}. \quad (2.5)$$

This type of process applies to α -decays as well as β -decays close to stability.

Probabilistic Decays: As described above, a process which depends on the properties of the nucleus (rather than the thermodynamic conditions) is characterized by the decay rate (or half-life) of that nucleus. However, the distinction exists for decays in which the daughter product distribution has some associated probability and can therefore result in a different set of products with each decay. This type of decay applies to spontaneous fission as well as some β -decays far from stability where the "traditional" β -decay is accompanied by the prompt emission of one or more neutrons.

Reactions: A reaction process is characterized by two or more reactants coming together to form a well-defined set of daughter products at a rate which is characterized by the thermodynamic conditions of the system. This process applies to such reactions as neutron and electron captures.

Probabilistic Reactions: Similar to decays and probabilistic decays, probabilistic reactions are distinguished from reactions by the probabilistic nature of their daughter product distribution. This type of reaction applies to induced fission processes, where a nucleus undergoes fission due to its

interaction with a reactant, e.g. neutron-induced fission or beta-delayed fission.

Thermodynamic Input

To follow the nuclear abundance evolution when reactions are involved, it is essential to have the time-evolution of the density and temperature in the regime where those reactions are relevant¹. In the context of this work, this thermodynamic evolution (referred to throughout this work, as well as in the literature, as “trajectories” or “thermodynamic trajectories”) is obtained by one of two methods, summarized here but described in more detail where relevant throughout the text.

Tracer Particles: In hydrodynamical or MHD simulations (which are the topic of Section 2.3), it is common to include computational elements that *trace* the motion and evolving properties of the fluid. Each simulation can reasonably track $\mathcal{O}(10^7)$ individual tracers. By taking those tracers that become unbound ($\mathcal{O}(10^5)$), one can obtain a wide range of trajectories with conditions reflecting the outcome of the detailed physical evolution of the disk. Thus one can use tracers to estimate nucleosynthesis outcomes of a more realistic physical system.

Parameterized Wind Model: A common method of qualitatively modeling a high-entropy environment for a “hot” r-process is employing a parameterization of an exponentially decreasing temperature and density due to a spherical, steady-state ($r^2 \rho v = \text{constant}$) expansion of a radiation-dominated gas (Panov and Janka 2009). Following a choice of initial conditions, such as temperature, entropy per baryon, and expansion timescale (τ_{dyn}), the density, ρ , and temperature, T_9 ², evolve as

$$T_9(t) = T_{9,0} \cdot \exp^{-t/\tau} \quad (2.6)$$

$$\rho(t) = \rho_0 \cdot \exp^{-3t/\tau}. \quad (2.7)$$

This parameterization approach significantly simplifies the problem by assuming what is essentially a one-dimensional wind, with no accounting for complex fluid behaviour. However, as a starting point, its simplicity allows one to investigate how the choice of initial conditions affects nucleosynthesis. Furthermore, it is relatively straightforward to construct linear combinations of nucleosynthesis calculations performed with these parameterized trajectories in order to approximate the results from more computationally expensive simulations.

Initial Composition

The third ingredient for a nucleosynthesis calculation is a description of the mass fraction, X_i , of each nucleus corresponding to the initial conditions, such that

$$\sum_i X_i = 1 \quad (2.8)$$

¹Late-time nucleosynthesis is significantly more strongly influenced by the decays of long-lived species.

²A commonly-used shorthand to express temperature in units of GK, e.g. $T_9 = 5$ is equivalent to $T = 5 \times 10^9 \text{ K}$.

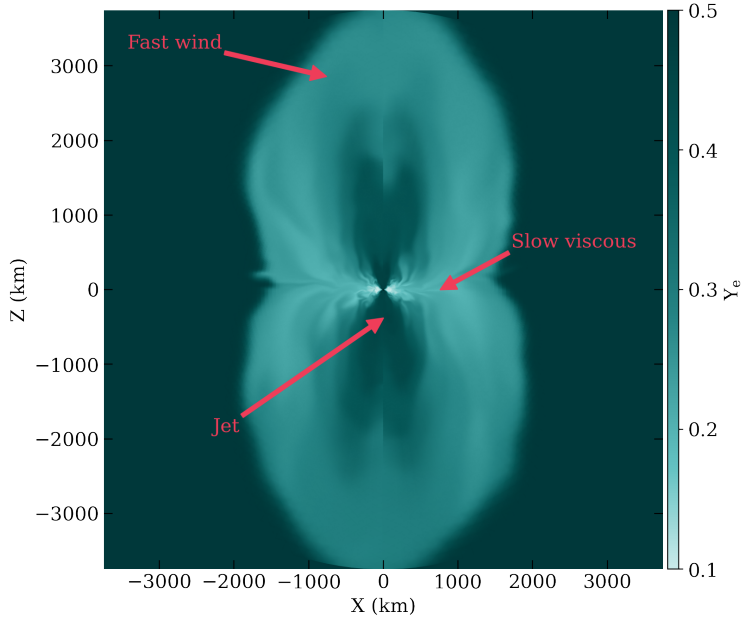


Figure 2.1: Major outflow components from a black hole accretion disk that could result from a binary neutron star merger. The outflows are shown from the side (xz plane) and colored by electron fraction, Y_e . This snapshot was taken roughly 30 ms into a nubhligh simulation with a weak initial magnetic field.

over all nuclei. In practice, a key choice here is that of the initial electron electron fraction. For a choice of initial Y_e , the distribution of nuclei satisfies

$$Y_e = \sum_i X_i \frac{Z_i}{A_i} \quad (2.9)$$

where the sum is over nuclei with proton number, Z_i and mass number, A_i .

2.3 Accretion Disk Simulations

The accretion disk surrounding a black hole is of astrophysical relevance on scales spanning stellar mass black holes in X-ray binary systems to supermassive black holes powering distant quasars. General relativistic magnetohydrodynamical (GRMHD) simulations offer the most detailed insight into the evolution of magnetically-driven outflows from an accretion disk surrounding the black hole remnant of a neutron star merger. Material is blown off the disk with varying velocities and dynamics leading to a rough distinction of outflow components, as illustrated in Figure 2.1. Turbulent heating causes a fast, hot wind to be driven off at early times in an hourglass shape around the poles. Meanwhile, turbulent viscosity drives slower material closer to the equator- this component tends to make up the largest outflow mass. Finally, the magnetic field can power a Blandford and Znajek (1977) low-mass but fast jet.

2.3.1 nubhlight

nubhlight (Miller et al. 2019a) is a three-dimensional GRMHD code with Monte Carlo neutrino radiation transport. The reader is referred to the public repository or original software publication for a complete description of the code (Miller et al. 2019a), though some details are included here. nubhlight solves the equations of ideal GRMHD via finite-volume methods with constrained transport, and uses Monte Carlo methods to perform neutrino radiation transport. These equations include³

$$\partial_t(\sqrt{-g}\rho_0 u^t) + \partial_i(\sqrt{-g}\rho_0 u^i) = 0 \quad (2.10)$$

$$\partial_t[\sqrt{-g}(T_\nu^t + \rho_0 u^t \delta_\nu^t)] + \partial_i[\sqrt{-g}(T_\nu^i + \rho_0 u^i \delta_\nu^i)] = \sqrt{-g}(T_\lambda^\kappa \Gamma_{\nu\kappa}^\lambda + G_\nu) \quad (2.11)$$

$$\partial_t(\sqrt{-g}B^i) + \partial_i[\sqrt{-g}(b^j u^i - b^i u^j)] = 0 \quad (2.12)$$

$$\partial_t(\sqrt{-g}\rho_0 Y_e u^t) + \partial_i(\sqrt{-g}\rho_0 Y_e u^i) = \sqrt{-g}G_{ye}, \quad (2.13)$$

with energy-momentum tensor T_ν^μ :

$$T_\nu^\mu = (\rho_0 + u + P + b^2) u^\mu u_\nu + \left(P + \frac{1}{2}b^2\right) \delta_\nu^\mu - b^\mu b_\nu. \quad (2.14)$$

The symbols used in Equations 2.10- 2.13 are labeled in Table 2.1 for convenience. Equation 2.10 represents the conservation of baryon number, or continuity. It dictates that the rate of change of rest mass density in a fluid element plus the net flux of mass across a surface must equal zero. Equation 2.11 represents energy-momentum conservation, subject to the radiation source term, G_ν . The evolution of the magnetic field is determined by Equation 2.12, and is subject to the no-monopole constraint:

$$\partial_i(\sqrt{-g}B^i) = 0, \text{ where} \quad (2.15)$$

$$B^i = {}^*F^{it}, \text{ and} \quad (2.16)$$

$${}^*F^{\mu\nu} = b^\mu u^\nu - b^\nu u^\mu \quad (2.17)$$

is the dual of the electromagnetic field (Maxwell) tensor, $F^{\mu\nu}$.

Finally, Equation 2.13 describes lepton number conservation subject to the source term, G_{ye} , which encodes the rates of lepton density transfer between the fluid and radiation field.

The key aspect of nubhlight as a GRMHD code is its treatment of neutrino transport via Monte-Carlo methods. nubhlight tracks neutrino interactions, classified as either absorption/emission or scattering processes with the former being the reactions that affect the electron fraction, Y_e , through the weak nuclear interaction. Neutrinos are treated as massless particles travelling on null geodesics, and obey the radiative transfer equation:

$$\frac{D}{d\lambda} \left(\frac{h^3 I_{\epsilon,f}}{\epsilon^3} \right) = \left(\frac{h^2 \eta_{\epsilon,f}}{\epsilon^2} \right) - \left(\frac{\epsilon \chi_{\epsilon,f}}{h} \right) \left(\frac{h^3 I_{\epsilon,f}}{\epsilon^3} \right). \quad (2.18)$$

³Einstein notation is used: repeated indices imply summation over all possible values.

Table 2.1: Description of symbols used in equations of GR ν MHD.

| MHD Terms | |
|--------------------------------------|--|
| Symbol | Description |
| $\sqrt{-g}$ | Square root of det(metric tensor) |
| ρ_0 | Rest energy |
| u^μ | Fluid four-velocity |
| T_ν^μ | Stress-energy tensor |
| $\Gamma_{\nu\kappa}^\lambda$ | Christoffel connection |
| G_ν | Radiation source term |
| B^i | B-field components of the Maxwell tensor |
| b^μ | B-field four-vector |
| b^2 | Square of the magnetic field |
| Y_e | Electron fraction |
| G_{ye} | Lepton source term |
| δ_ν^t | Kronecker delta |
| Greek indices ($\mu = 0, 1, 2, 3$) | Time + space components |
| Latin indices ($i = 1, 2, 3$) | Space-like components |

| Neutrino Terms | |
|-------------------------|---|
| Symbol | Description |
| $I_{\epsilon,f}$ | Intensity of ν -field |
| f | Neutrino flavor $f \in \{ \nu_e, \bar{\nu}_e, \nu_x \}$ |
| $\alpha_{\epsilon,f}$ | Absorption coefficient |
| $\sigma_{\epsilon,f}^a$ | Scatter coefficient for interaction a |
| $\eta_{\epsilon,f}$ | Neutrino emissivity |
| $j_{\epsilon,f}$ | Fluid emissivity |
| h | Panck's constant |
| ϵ | Neutrino energy |

The symbols in Equation 2.18 are similarly listed in Table 2.1.

At each step in a given simulation, the equations of ideal GRMHD are solved deterministically for a three-dimensional, finite-volume grid. The resolution of this grid is selected to satisfy minimum MRI-wavelength resolution requirements, which are discussed in Appendix B. The neutrino radiation transport is carried out by generating “superneutrinos”, or (radiation) packets of neutrinos which interact with the fluid via reactions, statistically guided by the emissivity, absorption opacity, and scattering cross sections. Each emission/absorption reaction contributes a change to the lepton source term, G_{ye} . Both G_{ye} and the radiation source term, G_ν , are then coupled to the MHD equations as in Equations 2.10- 2.13.

Once again, the reader is referred to the original software publication for details of tests used for the code at the time of its release. However, it is also worth describing two particular uses of nubhlight so far⁴. nubhlight offers a great deal of flexibility in setting the initial conditions of the disk one wishes to

⁴In addition to the work contained in Chapter 5, naturally.

investigate, meaning that it can be used to explore a wide range of astrophysical scenarios involving black-hole accretion disks.

Miller et al. (2020) used nubhlight to model the collapsar scenario (see Section 1.3.1) by constructing a $0.02M_{\odot}$ disk around a $3M_{\odot}$ black hole with initial $Y_e = 0.5$. The result of this was outflow that was relatively neutron-poor ($Y_e \geq 0.25$), producing first (and some second) peak material, but not producing third peak or actinide elements. Curtis et al. (2023) probed nucleosynthesis in the accretion disks following black hole-neutron star mergers by constructing disks with various combinations of black hole mass and spin parameter, disk mass, Y_e , and entropy. In all cases, these resulted in the production of material past the second peak, though with various levels of suppression beyond that. This implied, overall, a wide variety of possible nucleosynthetic outcomes from black hole-neutron star mergers.

While the examples do not directly relate to the work contained in this document, they highlight (or are manifestations of) some interesting physics points. The physics governing black hole accretion disk systems is largely scale-invariant. The “fundamental plane of accreting black holes” relates the properties of black hole accretion disks to the properties of the black holes themselves, and claims that a single central engine can be used to describe black holes across the mass spectrum (Shakura and Sunyaev 1973; Körding, E. et al. 2006; Mościbrodzka, M. et al. 2016). While this scale-invariance holds up well to observations, scale-dependence arises in, for example, the radiation physics relevant for energy transport in the system. The implication of this, though, is that GRMHD methods constructed to solve the problem of supermassive black hole accretion disks can be applied to stellar-size black hole systems with some clever consideration of the scale-dependent physics (Ryan et al. 2015; Miller et al. 2019a).

Thus the physical processes constructed into nubhlight are applicable to a broad range of astrophysical systems. While the examples above investigated collapsar and neutron star-black hole systems, the work of Chapter 5 is based on a single base system of a $0.12 M_{\odot}$ accretion torus surrounding a $2.8 M_{\odot}$ black hole with varying magnetic field strengths. The variation of this particular parameter is motivated by the scarcity of detailed studies of magnetic field strength effects on r-process nucleosynthesis from post-merger disks (see Section 1.3.2). However, given the wide range of conditions that could result from these mergers, there is still a wide parameter space to be explored.

CHAPTER
THREE

FROM MERGERS TO THE STARS: SOURCES OF UNCERTAINTY IN
DIFFERENT STAGES OF R-PROCESS MODELING

Neutron star mergers involve all four fundamental forces of nature working on physical scales ranging from sub-atomic and nuclear to stellar scales, as well as on timescales from fractions of a second to billions of years. The central theme of the work contained in this dissertation is the detailed investigation of different components of neutron star mergers, guided in the broadest sense by the question of whether neutron star mergers make r-process material, and what information is needed to find out. Despite the sophistication of numerical methods and modeling tools that have been made available over the last 6 years, there remains no single simulation suite that reliably models every stage of the merger, from coalescence to stellar enhancement. The ubiquitous approach in this field remains closely investigating one (or a few) aspects of the merger and stitching the pieces together as best one can. Thus careful consideration must be employed when transitioning from one scale to another to minimize the loss of accuracy or, at the very least, to be aware of simplifying assumptions made throughout.

This dissertation somewhat follows tradition by presenting three major works. A choice has been made to present these works in the chronological order in which they were completed, due to the very real, human experience of the author building upon what was learned in each work. However, this choice clashes with the scope as well as the order of the time scales explored in each work. Chapter 4 explores nuclear physics effects on nuclear heating, light curve evolution, and predictions of r-process signatures in metal-poor stars, thus exploring the latest time scales of the merger problem (hours to years). Chapter 5 takes a step back and investigates a disk that evolves on a time scale of up to a few seconds. Finally, Chapter 6 goes even further back and investigates EoS physics that set the conditions for the disk in the first place, but uses previous works to try and stitch everything together. This section aims to list some of the nuances in the framework of physical processes occurring on different time scales as well as sort of "road map" for this body of work.

3.1 The Blink of an Eye: Fractions of a Second

The formation and coalescence of two neutron stars occurs over orders of magnitudes of years. However, the time spanning the final stages of the inspiral to the point the two neutron stars touch is on the order of ms. In this regime, predictions of the behavior of the system are largely the realm of the nuclear EoS, which describes how material at nuclear densities reacts to such external forces as, for example, getting ripped apart by tidal forces.

The EoSs used in Chapter 6 are informed by chiral effective field theory (Tews et al. 2018; Capano et al. 2020). Starting from a description of pressure and energy density as a function of baryon number density, it was necessary to solve the TOV equations (Oppenheimer and Volkoff 1939) to obtain a description of the radius and tidal deformability of a neutron star as a function of its mass. These were applied to binaries with properties informed by numerical relativity simulations from the literature in order to make predictions about the system resulting from those binaries. From there, the work in Chapter 6 explores techniques used in obtaining information from this early phase of the merger via the EoS, and

probes some of the assumptions that are traditionally made when propagating this information into later parts of the merger.

3.2 Outward Bound: Milliseconds to Seconds

The evolution of the post-merger disk occurs on a timescale of up to a few seconds post-merger. Accretion in a black-hole torus system “turns on” a fraction of a second after the disk is initialized, with the exact time depending on the conditions in the disk. The detailed physics embedded in `nubhlight` represents a huge computational cost: running a single disk out just past 100 ms required roughly 3 weeks on some 300 cores. These disks carry valuable information regarding the evolution of the disk in the form of Lagrangian tracers (see Section 3.6 of Miller et al. 2019a) which track, among other quantities, the inputs necessary for nucleosynthesis: temperature, density, and Y_e , as a function of time.

Each tracer is turned into a single nucleosynthesis calculation- the combination of each nucleosynthesis calculation is what is interpreted as the abundance pattern produced in the disk outflows. It is necessary to “convert” each tracer into a thermodynamic trajectory beginning at the point where the conditions for nucleosynthesis are met. For this work, 10 GK was chosen, which required finding the point in each tracer where it was last at 10 GK, keeping in mind that some tracers crossed this threshold more than once.

Once the *tracer* is effectively “pruned”, one must record the conditions at which the resulting *trajectory* begins in order to compute a nuclear abundance consistent with the Y_e at that point. Additionally, given that the disk simulations in this work only reach $\mathcal{O}(100 \text{ ms})$, it was necessary to extrapolate assuming homologous expansion. This extrapolation is a reasonable approach *if* it is assumed that the tracers are no longer subject to turbulence in the disk and are unbound.

The results of this procedure can be see in Figure 3.1, which shows the spatial trajectories for a selection of tracers. Each row displays tracers from one of three separate disk simulations carried out using `nubhlightin` which the initial magnetic field strength was varied. For each of three disks, each unbound tracer was converted to a thermodynamic trajectory and input into a nucleosynthesis calculation. Of these, the top 50% of lanthanide-producing and actinide-producing tracers were selected, shown in the top and bottom halves of each individual panel, respectively. In the left top (bottom) half of each panel, the tracers are colored according to their resulting lanthanide (actinide) mass fraction after 1 GYr. The right side shows the Y_e each tracer had at $T_9 = 10\text{GK}$. The columns in Figure 3.1 simply categorize each set of tracers according to their angular position above the equator at the time nucleosynthesis started ($T_9 = 10\text{GK}$). The exercise of constructing this figure shows how one can connect nucleosynthetic outcomes- in this case, lanthanide or actinide production- to the morphology, or to processes occurring in the disk.

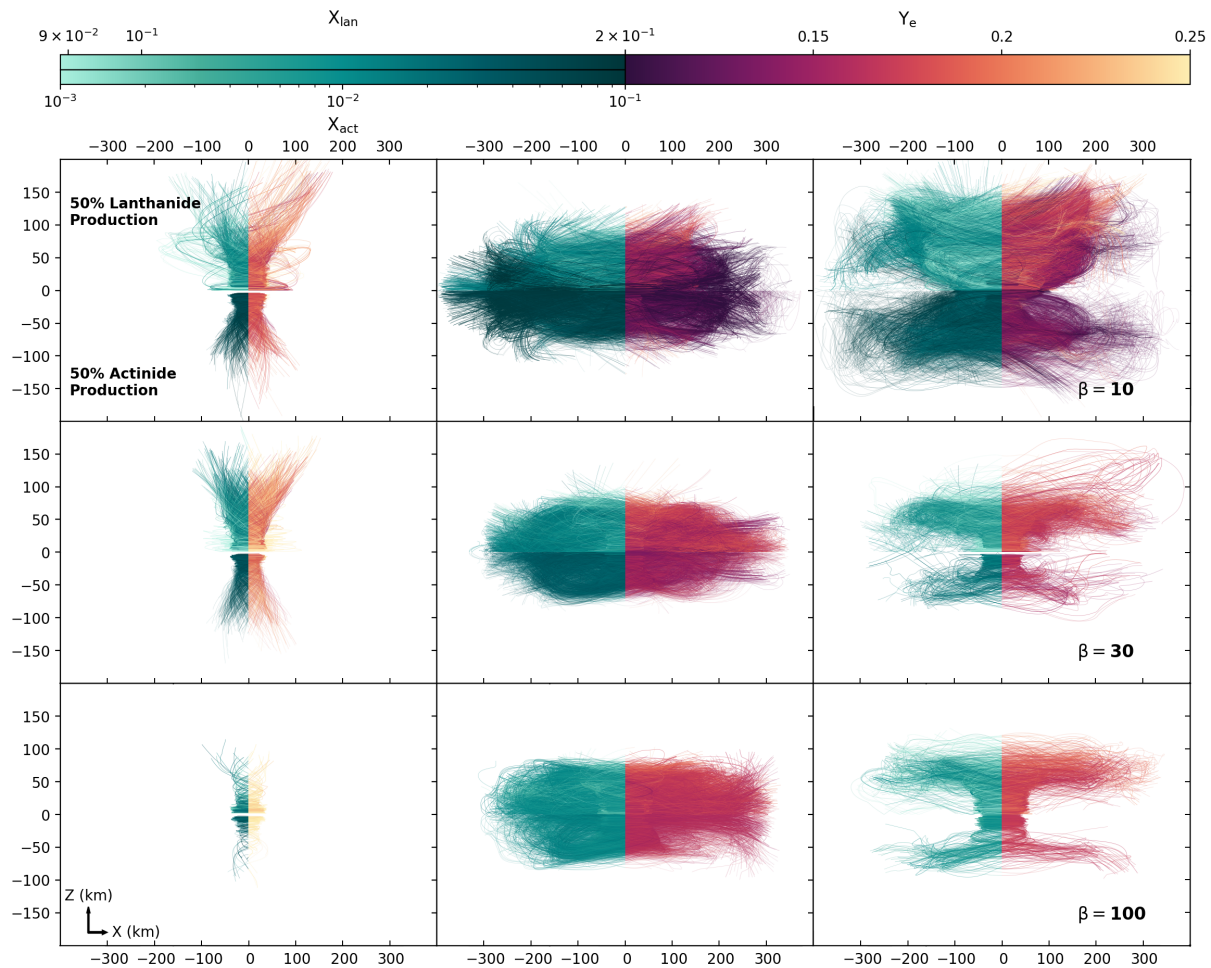


Figure 3.1: Spatial trajectories of tracers responsible for the production of 50% of lanthanide (top) and actinide (bottom) production by mass, colored by lanthanide (or actinide) mass fraction at 1 GYr (left) and Y_e at $T_9 = 10$ (right) for three GRMHD accretion disk simulations.

3.3 Moving up in the World: Seconds to Years

Whether the disk wind is approximated by a parameterized model or informed by GRMHD simulations, predicting the nucleosynthetic outcome of the post-merger disk outflow requires following processes that begin on a time scale of seconds and extend out to several years. The nuclear reactions that are followed in a network calculation carry with them energy output that powers the kilonova light curve. Computing how much energy is consumed or released in a reaction or decay requires knowledge of the mass difference between the parent and the daughter(s) to compute the Q-value:

$$Q = \left(\sum m_{\text{reactants}} - \sum m_{\text{products}} \right) c^2 \quad (3.1)$$

As described in Chapter 2, this requires a theoretical model to predict the masses of the nuclei involved.

The energy that is released from a nuclear process is deposited into the surrounding material via decay products as well as photons. The effectiveness with which this energy is transferred to the surrounding medium varies for different decay products: fission fragments and α -particles very effectively transfer energy to the surrounding medium. Conversely, β -decay products (electrons and electron neutrinos) impart energy into the diffuse medium much less efficiently¹ (see Barnes et al. 2016; Kasen and Barnes 2019, for more detailed derivations and a description of thermalization efficiencies for a kilonova medium).

A final key piece necessary for converting nuclear heating into a bolometric luminosity is an approximation of the opacity, which is largely dependent on the composition. A high opacity, which could be caused by a high lanthanide mass fraction, is expected to draw out the peak of the kilonova light curve towards later times ($\mathcal{O}(\text{days})$).

These combined effects influence the behavior of the kilonova light curve from a few days out to several weeks or months. Beyond this, decays of long-lived species closer to stability still occur. For this reason, most “final” abundance patterns are taken around 1 Gyr (10^9 years), as this gives all but the longest-lived species time to settle and decay back to stability.

Once a description of abundances is obtained, one passes into the realm of interstellar scales and timescales of galactic evolution. In this work, this takes the form of using elemental patterns produced from a variety of nuclear physics prescriptions to estimate the ages of the few metal-poor, r-process enhanced stars with uranium signatures.

¹See, for example, Figure 1 of Zhu et al. (2021) showing the steep decline in β -decay thermalization efficiency compared to α -decay and fission.

CHAPTER
FOUR

THE INFLUENCE OF BETA-DECAY RATES ON R-PROCESS OBSERVABLES

KELSEY LUND

with

JONATHAN ENGEL, GAIL McLAUGHLIN, MATTHEW MUMPOWER, EVAN NEY, REBECCA SURMAN

The following chapter was published in its entirety in The Astrophysical Journal, Vol. 944, Number 2 (2023). Some figures have been modified from their original versions to fit dissertation format.

4.1 Abstract

The rapid neutron capture process (*r*-process) is one of the main mechanisms whereby elements heavier than iron are synthesized, and is entirely responsible for the natural production of the actinides. Kilonova emissions are modeled as being largely powered by the radioactive decay of species synthesized via the *r*-process. Given that the *r*-process occurs far from nuclear stability, unmeasured beta decay rates play an essential role in setting the time scale for the *r*-process. In an effort to better understand the sensitivity of kilonova modeling to different theoretical global beta-decay descriptions, we incorporate these into nucleosynthesis calculations. We compare the results of these calculations and highlight differences in kilonova nuclear energy generation and light curve predictions, as well as final abundances and their implications for nuclear cosmochronometry. We investigate scenarios where differences in beta decay rates are responsible for increased nuclear heating on time scales of days that propagates into a significantly increased average bolometric luminosity between 1-10 days post-merger. We identify key nuclei, both measured and unmeasured, whose decay rates directly impact nuclear heating generation on timescales responsible for light curve evolution. We also find that uncertainties in beta decay rates significantly impact age estimates from cosmochronometry.

4.2 Introduction

Since its emergence in the 1950s, one of the biggest questions in the field of nuclear astrophysics remains the main production site of some of the heaviest elements, synthesized via the rapid neutron capture process (*r*-process) (Burbidge et al. 1957; Cameron 1957). It is currently hypothesized that this process, thought to be responsible for roughly half the material heavier than iron, as well as the only process for producing the actinides, occurs to some extent in the neutron-rich outflows of neutron star mergers (NSM). In addition to the many theoretical advances made in the last few decades, the recent electromagnetic observations accompanying the gravitational wave event GW170817 (Abbott et al. 2017b,c; Díaz et al. 2017) lend the most support to the long-standing idea of a kilonova (KN) explosive transient powered by the radioactive decay of freshly synthesized *r*-process material (Lattimer and Schramm 1974; Lattimer and Schramm 1976; Li and Paczyński 1998; Metzger et al. 2010; Roberts et al. 2011; Barnes and Kasen 2013; Grossman et al. 2014; Wollaeger et al. 2018; Fontes et al. 2020).

The luminosity and morphology of the light curve associated with AT2017gfo (Chornock et al. 2017; Cowperthwaite et al. 2017; Nicholl et al. 2017; Perego et al. 2017) offer unique insight into the physics of these extreme environments. The bright but rapidly decaying component of the light curve observed at shorter wavelengths indicates at least some portion of ejecta material with little to no lanthanide or actinide abundances (Metzger et al. 2010; Roberts et al. 2011; Evans et al. 2017; Miller et al. 2019b). On the other hand, a dimmer "red" signal that dominates on timescales of days (when the "blue" signal has faded away) indicates that at least some portion of the ejected material is composed of high-opacity lanthanides and possibly actinides (Barnes and Kasen 2013; Tanaka and Hotokezaka 2013; Kasen et al.

2017). These combined observations suggest distinct nucleosynthesis sites within the merger ejecta, each of which might be capable of producing a robust *r*-process pattern.

Despite the wealth of information provided by the data from GW170817, the larger endeavour of modeling KN signals for the purpose of reliably interpreting future signals remains subject to many unknown quantities and large uncertainties. While it is generally accepted that NSMs are a site for *r*-process production, it remains unclear whether these sites alone are capable of producing the entire observed *r*-process pattern. Studies of material ejected on dynamical timescales, either via tidal forces or compression between the coalescing neutron stars, predict material that is neutron-rich enough to produce out to the second and third *r*-process peaks (Rosswog et al. 1999; Goriely et al. 2011; Korobkin et al. 2012; Bauswein et al. 2013b; Wanajo et al. 2014; Sekiguchi et al. 2015; Radice et al. 2018b).

While there is general agreement on the robustness of *r*-process production in dynamically ejected channels, there is more uncertainty regarding the extent to which *r*-process production occurs in late-time accretion disk outflows driven by viscous heating. Some part of this uncertainty comes from the central remnant scenario (Shibata et al. 2005; Agathos et al. 2020; Nedora et al. 2021; Kashyap et al. 2022). When prompt collapse does not occur, neutrino interactions are capable of driving the Y_e up enough to stifle *r*-process production. Neutrino oscillations can also play a large part in determining the extent of this effect, as only electron neutrinos act to reduce the neutron-richness of the ejecta (Malkus et al. 2012; Siegel and Metzger 2017; Li and Siegel 2021).

Simulating *r*-process nucleosynthesis is also subject to large uncertainties due to its trajectory far from nuclear stability where many important quantities remain unmeasured (Martin et al. 2015; Mendoza-Temis et al. 2015; Eichler et al. 2015; Mumpower et al. 2016b; Nikas et al. 2020). Detailed calculations incorporate nuclear heating contributions from multiple decay modes, and these impact the energy released, the thermalization efficiency with which the decay products deposit energy into the system, and the composition of material that is ultimately synthesized (Beun et al. 2008; Barnes et al. 2016; Mumpower et al. 2018; Even et al. 2020; Sprouse et al. 2020).

Of particular interest is the production of heavy nuclei that can undergo alpha decay or fission, especially when these are populated such that they decay on time scales whereby they compete with beta decay heating. On time scales of days to weeks, nuclei of $A \sim 130$ contribute a large part of the beta decay heating. However, the incorporation of theoretical spontaneous fission and alpha decay rates have been found to largely impact the uncertainty in the nuclear heating on time scales relevant for the evolution of the red component of the light curve, in some cases adding up to an order of magnitude to the uncertainty (Goriely 2015; Vassh et al. 2019; Giuliani et al. 2020; Zhu et al. 2021; Barnes et al. 2021). These combine with additional uncertainties including the nuclear equation of state (Oechslin et al. 2007; Bauswein et al. 2013b; Hotokezaka et al. 2013a; Sekiguchi et al. 2015; Lehner et al. 2016), the nature of neutrino oscillations and neutrino transport in the ejecta (Ruffert et al. 1997; Foucart et al. 2016; Martin et al. 2018; Miller et al. 2019b; Kullmann et al. 2021), as well as atomic line energy calculations for high-opacity lanthanides and actinides.

One particularly important data set for an *r*-process nucleosynthesis calculation is a description

of the beta decay rates involved (Möller et al. 2003; Caballero et al. 2014; Marketin et al. 2016; Shafer et al. 2016; Ney et al. 2020; Robin et al. 2022; Kullmann et al. 2022). At early times, the extent of *r*-process production is sensitive to the beta decay rates of the nuclei involved, as these determine the relative abundances of connected isotopic chains during $(n, \gamma) - (\gamma, n)$ equilibrium and compete directly with neutron capture when equilibrium fails. At later times, and once a population of high mass number species is synthesized, beta decay rates play a further role in determining the time scale of beta decay chains which are important for heating as well as for populating species which contribute significantly to spontaneous fission and alpha decay heating. Additionally, theoretical beta decay rates can compete with theoretical alpha decay and spontaneous fission branching ratios which are crucial for determining the shape and magnitude of the light curve (Zhu et al. 2021).

In this work, we aim to incorporate different global beta decay descriptions into nucleosynthesis calculations and compare their impact with those of other astrophysical and nuclear sources of uncertainty on nuclear energy generation, light curve evolution, and predictions relevant to nuclear cosmochronometry. In Section 4.3, we describe the methods we use in generating and compiling nuclear data as well as the computational methods we use for calculating relevant quantities. We build upon the work and methods contained in Zhu et al. (2021) and Barnes et al. (2021), whose work mainly focused on off-stability mass models and different fission prescriptions. For our astrophysical conditions, we aim to investigate the behavior of ejecta containing both high and low- Y_e material, expanding upon the models considered in, e.g. Kullmann et al. (2022), which focus on specific hydrodynamical simulations that tend to include more high- Y_e material. In Section 4.4, we show the results of our calculations of nuclear energy generation and investigate cases of significant heating from heavy *r*-process alpha-decaying and fissioning nuclei on late-time light curve evolution. We also show the broader impact these uncertainties in nuclear effective heating can have on a bolometric light curve. We conclude the presentation of our results with Section 4.5, in which we compute age estimates for a selection of *r*-process-enhanced metal poor stars using theoretically calculated abundances. Finally, we provide some concluding remarks in Section 4.6.

4.3 Method

We seek to quantify the leverage of beta decay rates on key aspects of kilonova modeling when compared with other sources of nuclear and astrophysical uncertainty. The evolution of the nucleosynthetic abundances throughout the *r*-process determines the energy output in the form of nuclear heating. The thermalization profile of this released energy will determine how it is transported away from the system, which in turn affects the shape and magnitude of the observable light curve. The final abundance that is produced in a given merger event can then be used in a stellar dating technique if it is interpreted as being the sole source of a star's *r*-process material. In this section, we describe our data set and the methods used in the calculation of these quantities.

4.3.1 Model Set and Nucleosynthesis

We use the Portable Routines for Integrated nucleoSynthesis Modeling (PRISM) to perform nucleosynthesis calculations using a suite of prepared input files describing astrophysical conditions and nuclear properties for a wide range of nuclei. The extent of *r*-process production is sensitive to the beta decay rates of the nuclei involved, as these compete with neutron capture rates. Currently, many methods exist to compute beta decay rates, but few are applied to large sections of the chart of the nuclides. In order to investigate the extent of the impact of different "global" sets of beta decay rates in our calculations, we construct separate beta decay and coupled beta decay/beta-delayed fission reaction data sets consistent with three different beta decay calculations, which we describe below.

The description contained in the work of Ney et al. (2020) (calculations using these rates will hereafter be referred to as NES) uses the finite amplitude method with Skyrme density functionals to compute the beta decay half-lives for neutron rich species. These rates are an extension to Mustonen and Engel (2016), and include rates for all nuclei involved in the *r*-process as opposed to only even-even nuclei. This set of rates has not been used before in a parameterised study of *r*-process observables. The work of Marketin et al. (2016) (hereafter MKT) uses a covariant density functional theory approach with Gogny interactions to do the same. Möller et al. (2019) (hereafter MLR) uses a finite range droplet model in a quasiparticle random phase approximation to obtain β -strength functions for neutron-rich species. We use the three sets of beta decay rates described and compute beta delayed neutron emission and beta-delayed fission probabilities and daughter product distributions using Mumpower et al. (2016a). We show the base-ten logarithm of the ratio of all three sets of beta decay rates with respect to those of Möller et al. (2003) (MLR03) in Figure 4.1. By using these three sets of rates, we are able to investigate the influence of a range of broadly fast (MKT) to broadly slow (NES) rates.

In addition to beta decays, the nuclei involved in the *r*-process are also subject to other reactions and decays. The energy associated with these decays is important for the nuclear heating, and plays a large part in determining the shape and magnitude of the light curve. We calculate reaction and decay rates, as well as Q-values, consistent with the eight nuclear models listed in Table 4.1. We incorporate theoretical alpha decay rates obtained using a Viola-Seaborg relation. We use neutron capture and neutron-induced fission rates calculated using the statistical Hauser-Feshbach code, CoH (Kawano et al. 2016).

For spontaneous fission rates, we use the barrier-height-dependent prescription from Karpov et al. (2012) and Zagrebaev et al. (2011). We adopt mass models with appropriate fission barrier height descriptions: ETFSI (Aboussir et al. 1995) with ETFSI, TF (Myers and Świątecki 1999) with TF, HFB14 (Goriely et al. 2009) with HFB22 and HFB27, and FRLDM (Möller et al. 2015) for all others. We consider two possible fission fragment distributions; the first is a symmetric split, where the daughter products each equal one-half of the parent nucleus, while the second is the double Gaussian distribution described by Kodama and Takahashi (1975) (hereafter K&T). We make an exception for the fission fragment distribution of the spontaneous fission of ^{254}Cf , where we use the more detailed calculation from Zhu et al. (2018).

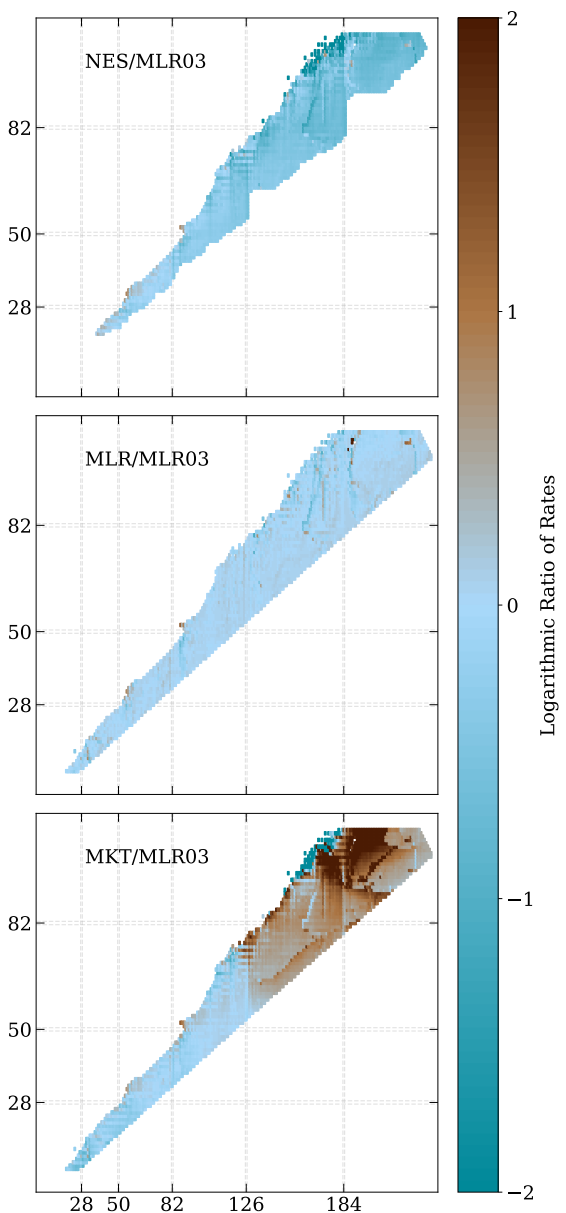


Figure 4.1: Logarithmic ratios of NES (top), MLR (center), and MKT (bottom) beta decay rates with respect to MLR03 beta decay rates. The color bar is adjusted to values of -2,2 to reveal trends more clearly. The area covered by the Nubase 2016 data set (Audi et al. 2017) is removed.

Table 4.1: Nuclear mass models (and associated references) used in nucleosynthesis calculations.

| Abbreviation | References |
|--------------|---|
| DZ33 | Duflo and Zuker (1995) |
| ETFSI | Aboussir et al. (1995); Mamdouh et al. (2001), Möller et al. (2016) |
| FRDM2012 | |
| HFB22,HFB27 | Goriely et al. (2009, 2013b) |
| SLY4 | Chabanat et al. (1998); Möller et al. (2015) |
| TF | Myers and Świątecki (1996, 1999) |
| UNEDF1 | Kortelainen et al. (2012); Möller et al. (2015) |
| WS3 | Liu et al. (2011); Möller et al. (2015) |

Finally, where experimental or evaluated data is available, we overwrite theory rates with data from Nubase (Audi et al. 2017), and calculate Q-values using experimentally determined masses from AME2016 (Wang et al. 2017).

For the thermodynamic evolution of the ejecta, we use a parameterized wind model (Panov and Janka 2009) with an initial entropy per baryon of $s/k = 40$ and an expansion timescale of 20 ms. The network begins in nuclear statistical equilibrium with initial seed nuclei determined using the SFHo equation of state (Steiner et al. 2013). In this work, we use the initial electron fraction, Y_e , as a proxy of variation in the astrophysical conditions of the ejecta in order to compare with uncertainties from the previously described variations from theoretical nuclear models. We note that a different choice of initial entropy per baryon or expansion timescale would likely have an effect on our results. While we acknowledge the importance of this question, it remains outside the scope of this work. We refer the reader to studies that explore this more carefully, including Just et al. (2015); Radice et al. (2018b); Orford et al. (2022), and others.

We use single- Y_e trajectories with initial values of 0.02, 0.18, and 0.21 for the full suite of theoretical nuclear inputs. Based on the work in Zhu et al. (2021), we consider that these can be taken to represent varying degrees of contribution from fission to the total heating, with $Y_{e,i} = 0.21$ yielding the smallest contribution.

We also consider a set of trajectories to more closely model an ejecta with non-uniform composition. To do this, we perform nucleosynthesis calculations using the FRDM2012 and HFB22 subsets of nuclear inputs on single- Y_e trajectories ranging from 0.01 to 0.35 in increments of 0.01. We map these onto an analytic probability distribution in order to sample a range of distributions with resulting average Y_e values between 0.13 and 0.23. We show these mappings in Figure 4.2, and note that the resulting distributions contain both double-peaked distributions as well as single-peaked centered around a Y_e of 0.18, as can be seen by the individual dashed lines in the figure. These distributions were obtained by

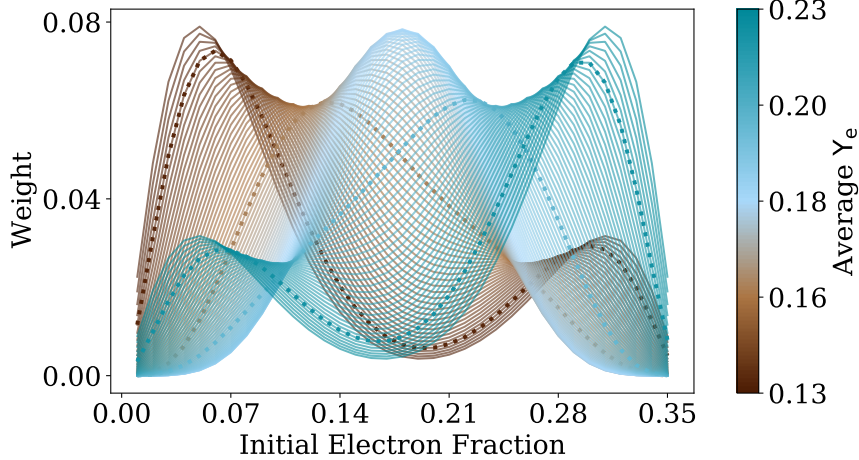


Figure 4.2: Distribution of combined single- Y_e trajectories. The color of each line indicates the average Y_e of the “combined trajectory”. A selection of combinations are shown as a guide to highlight the double-peak structures within the distribution. This color scheme is used throughout this work to refer to results for each combined trajectory, with the bluer combinations having less neutron-rich (low Y_e) material and the more brown combinations having more neutron-rich material.

combining two beta probability distribution functions and are described by the functional form

$$f(x, \alpha, \beta) = 2.5 \left(\frac{\Gamma(\alpha + \beta)x^{\alpha-1}(1-x)^{\beta-1}}{\Gamma(\alpha)\Gamma(\beta)} \right) + \quad (4.1)$$

$$\left(\frac{\Gamma(\beta + \alpha)x^{\beta-1}(1-x)^{\alpha-1}}{\Gamma(\beta)\Gamma(\alpha)} \right), \quad (4.2)$$

where $\Gamma(\alpha)$ is the gamma function of α . We vary the values of α and β between 2.5 and 10.5¹.

Previous work found that solar-like abundances can be obtained by combining individual trajectories with both high initial Y_e and well as low initial Y_e (Zhu et al. 2021). Our goal is not necessarily to obtain a solar-like final abundance pattern (we direct the reader to, for example, Ristić et al. (2023), which addresses r -process universality), since we do not know if kilonova events produce a solar pattern. Rather we aim to sample a variety of trajectories containing material with a variety of neutron richness, whether from dynamical ejecta plus disk outflows or from multi component disk outflows. This is consistent with most modern kilonova models predicting multiple ejecta components (see for example Just et al. (2015); Radice et al. (2016); Radice et al. (2018b); Miller et al. (2019b); Nedora et al. (2021); Stewart et al. (2022)), while not constraining our investigation to any single hydrodynamical simulation.

We utilize these combinations of simulations for effective heating, as well as light curve calculations out to 50 days. We also calculate late-time abundances (on the order of several GYr), for cosmochemistry calculations (see Section 4.3.4).

¹We use Scipy’s (Virtanen et al. 2020) built-in beta function to generate these distributions.

4.3.2 Nuclear Heating

The evolution of the nuclear heating is given by coupling the energy from the radioactive decays with the efficiency with which their products thermalize. We therefore take the outputs from the nucleosynthesis calculations described and calculate the effective heating rate by combining the Q-value from the radioactive decays with the thermalization efficiency. We follow the method in Kasen and Barnes (2019) and Zhu et al. (2021), with the total effective heating rate given by

$$\dot{Q}(t) = \sum_i \dot{q}_i(t) f_i(M_{ej}, v_{ej}, t) M_{ej} \quad (4.3)$$

where the sum is over all reactions and decays. The thermalization, f_i , is calculated as in Kasen and Barnes (2019) and is dependent on the ejecta mass and velocity. We use a total ejecta mass of $0.05M_\odot$ and an ejecta velocity of $0.15c$.

4.3.3 Semi-Analytic Light Curve Model

We construct a semi-analytic light curve model following Zhu et al. (2021) and Metzger (2020). We include some of the relevant details of the calculation here for convenience. We divide the ejecta into 100 layers with $0.1 < v/c < 0.4$, with a velocity-dependent mass distribution and density profile given by

$$M_v = M_{ej} \left(\frac{v_0}{v} \right)^3 \quad (4.4)$$

$$\rho(v, t) = \frac{3M_v}{4\pi v^3 t^3}. \quad (4.5)$$

The evolution of each shell is calculated independently using a forward-Euler scheme from 0.01 days to 50 days post-merger, obeying

$$\frac{dE_v}{dt} = \frac{M_v}{M_{ej}} \dot{Q}(t, v) - \frac{E_v}{t} - L_v. \quad (4.6)$$

The last term,

$$L_v = \frac{E_v}{t_{d,v} + t_{lc}}, \quad (4.7)$$

is the luminosity of a shell and is dependent on the diffusion timescale, $t_{d,v}$, and the light-crossing time, t_{lc} of that shell:

$$t_{d,v} = \frac{M_{ext} \kappa}{4\pi v t c}, \text{ and} \quad (4.8)$$

$$t_{lc} = \frac{vt}{c}. \quad (4.9)$$

Table 4.2: Names of select r-ii stars with their observed abundances. These stars are sorted by increasing actinide enhancement.

| Star Name | $\log_{\epsilon}(\text{Eu})$ | $\log_{\epsilon}(\text{Th})$ | $\log_{\epsilon}(\text{U})$ | Reference(s) |
|-------------|------------------------------|------------------------------|-----------------------------|----------------------------------|
| HE1523-0901 | -0.62 | -1.2 | -2.06 | Frebel et al. (2007) |
| CS29497-004 | -0.66 | -1.16 | -2.20 | Hill, V. et al. (2017) |
| CS31082-001 | -0.72 | -0.98 | -1.92 | Siqueira Mello, C. et al. (2013) |
| J2038-0023 | -0.75 | -1.24 | -2.14 | Hill, V. et al. (2002) |
| J0954+5246 | -1.19 | -1.31 | -2.13 | Placco et al. (2017) |
| | | | | Holmbeck et al. (2018a) |

Here, M_{ext} is the mass exterior to the shell with velocity v . κ is the opacity of the layer, which is calculated as a function of the temperature, T_v ,

$$T_v = \left(\frac{E_v \cdot \rho(v, t)}{a \cdot M_{\text{norm}}} \right)^{\frac{1}{4}} \quad (4.10)$$

of the layer, as:

$$\kappa = \begin{cases} \kappa_{\text{max}} \left(\frac{T}{4000 \text{ K}} \right)^{5.5}, & T < 4000 \text{ K} \\ \kappa_{\text{max}} & \text{otherwise} \end{cases} \quad (4.11)$$

The value of κ_{max} depends on the composition of the ejecta. Specifically, the presence of lanthanides and actinides contribute large opacities which are important for the "red" component of the light curve that is relevant on timescales of days (and the focus of this work). Given the temperature-dependent treatment we have selected (as opposed to a "grey" opacity), we adopt a value of κ_{max} of $100 \text{ cm}^2 \text{ g}^{-1}$ for all simulations, as this represents the scale of the maximum opacity from more detailed calculations of low- Y_e , lanthanide-bearing ejecta on timescales of a few days (Kasen et al. 2013; Tanaka et al. 2020).

4.3.4 Nuclear Cosmochronometry

The material produced in the NSM can act as a source of enrichment for a nearby stellar environment, i.e. the final abundance of an *r*-process-producing event can be taken as the initial abundance of a star. These can then be compared with spectral observations of stars, and a relation between the time of the enrichment event and the time of observation can be obtained by comparing the measured decay timescales and abundances of radioactive species (Butcher 1987). To this end, we compile a selection of five *r*-process-enhanced ($[\text{Eu}/\text{Fe}] > +1.0$), metal-poor ($[\text{Fe}/\text{H}] < -2$) stars of varying actinide richness, listed in Table 4.2.

From these observations, we use the measurements of europium ($Z=63$), thorium ($Z=90$), and uranium ($Z=92$). We take the initial abundances to be those produced in a NSM and remaining 1 Gyr post-merger. Running the calculations out this long allows us to only rely on the theoretical abundances of the long-lived isotopes of thorium (^{232}Th) and uranium (^{238}U), which have half-lives of 14 Gyr and 4.47 Gyr, respectively. We compare these with the final abundances of the two most stable isotopes of

euroeuropium (^{151}Eu and ^{153}Eu).

If the NSM is taken to be the sole source of *r*-process enrichment, and is interpreted as occurring at $t=0$, then the observed spectra can be interpreted as being taken at time t given by the following relations:

$$t = 46.67 \text{ Gyr} [\log_e(\text{Th/Eu})_0 - \log_e(\text{Th/Eu})_{\text{obs}}] \quad (4.12)$$

$$t = 14.84 \text{ Gyr} [\log_e(\text{U/Eu})_0 - \log_e(\text{U/Eu})_{\text{obs}}] \quad (4.13)$$

$$t = 21.80 \text{ Gyr} [\log_e(\text{U/Th})_0 - \log_e(\text{U/Th})_{\text{obs}}]. \quad (4.14)$$

These relate the initial abundances, $\log_e(X/Y)_0$, to abundances, $\log_e(X/Y)_{\text{obs}}$. This approach, while useful, has a tendency to yield inconsistent results, especially when applied to actinide-boost stars, which are overabundant in thorium and uranium (Holmbeck et al. (2019) classifies these as having $\log_e(\text{Th/Dy}) > -0.90$).

We explore the impact of changing the description of beta decay rates on the final abundance pattern where relevant for cosmochronometry calculations using the stars listed in Table 4.2, (all of which are notable for their detection of uranium). The abundance patterns we use to perform these calculations are constructed from the subset of individual trajectories using the FRDM2012 mass model, with initial electron fractions ranging from 0.01 to 0.35, as described in Section 4.3.1.

4.4 Effective Heating and Light Curve

We demonstrate the influence of beta decay rates on the effective heating and the light curve by first considering single trajectory models which have a single value of the initial electron fraction. We then turn to multi-trajectory models which account for ejecta which has a weighted range of initial neutron richness, as illustrated in Figure 4.2. In all cases, we take the total heating to be the summed contribution of the effective heating (as described in Section 4.3.2) from beta decay, spontaneous fission, and alpha decay reactions.

4.4.1 Single Trajectory

We begin with three different single trajectory models which are chosen to access different physics. The $Y_e = 0.02$ case is chosen to probe very neutron rich ejecta that experiences fission cycling, where the daughter products of the first nuclei which fission capture enough neutrons to make it back to very heavy nuclei that will fission again. The $Y_e = 0.18$ case is chosen because a significant number of nuclei fission, but there is limited cycling, since at this Y_e , the number of neutrons is not enough to allow nuclei to fission twice. Finally, the $Y_e = 0.21$ case was chosen because material with this neutron richness makes a full *r*-process but does not have enough neutrons for much fission to occur.

The first row of Figure 4.3 shows the range of total heating curves resulting from these single- Y_e trajectories of 0.02 (left), 0.18 (center), and 0.21 (right). The width of any one shaded band comes from the

use of different mass models, and corresponding fission barriers, with each band color corresponding to one set of beta decay rates from Figure 4.1. Overlap in the bands for different Y_e cases appear as a darker region on the plot. An immediately noticeable trend is that the two lower Y_e cases have a wider spread in the prediction of total heating than the highest Y_e simulation does. In these lower Y_e cases, the NES simulations (darkest blue region) tend to show the highest *total* heating rates, i.e. they provide an upper limit for the total heating. Conversely, the MKT simulations (light blue region) tend to show less total heating and therefore provide a lower limit for the same.

To explore the reason for these effects, in the next three rows of the figure, we plot the contribution to the effective heating that stems directly from beta decaying nuclei (second row), fissioning nuclei (third row) and alpha-decaying nuclei (bottom row). In all cases, the upper limit of the total heating shown in the top row is reproduced as a faint dashed line for comparison. The narrow width of the beta decay heating bands, as well as their overlap, indicates that uncertainties in total effective heating, seen in the top row, cannot *directly* be attributed to differences in the beta decay heating. The third and fourth rows of Figure 4.3 indicate that, in fact, the largest variation in total heating instead comes from differences in the contribution of spontaneous fission and alpha decay heating. Looking at the right-most column, the $Y_e = 0.21$ case, we see that the total heating is dominated by beta decay, with alpha decay and spontaneous fission making up a relatively small portion of the total heating. As a consequence, the total heating for this case (top right) exhibits the least variation with different beta decay rates. At about 1 day, this variation spans only about a factor of 2. However, looking at the left-most column ($Y_e = 0.02$), we see that fission can substantially affect both the total heating and the uncertainty in the total heating. The choice of beta decay rates is *indirectly* but strongly influencing the total heating.

For some low Y_e simulations, the contribution of fission is sub-dominant, but for others, fission is the majority contribution, leading to the substantial spread in the results. Alpha decay plays a similar role in the middle Y_e cases (second column), where it largely controls the width of the band. The NES simulations contribute the upper limit in alpha decay in the middle Y_e simulations as well as the upper limit to the heating at a day. Finally we note that the lower limits on the total heating, which are very similar between the three sets of beta decay rates, occur in simulations with minimal alpha decay and fission, and are determined primarily by the beta decay rates.

The shape and peak luminosity of the late-time ("red") light curve are expected to be substantially influenced by the evolution of the nuclear heating (Zhu et al. 2021; Barnes et al. 2021)). Thus, as described in Section 4.3.3, we compute the evolution of the light curve on a timescale of days, out to 40 days post-merger. Analogous to Figure 4.3, we show the ranges of these results in Figure 4.4. We see that the beta decay rates which produce the upper limit in the overall heating produce a corresponding upper limit in the light curve. Similarly, the range of uncertainty follows the pattern of heating bands with the largest variations coming from the lowest Y_e cases. It is interesting to note that in the $Y_e = 0.21$ scenarios, the full range of variation is largely captured by the MLR rates.

While Figures 4.3 and 4.4 show the broad uncertainty in heating and light curve evolution that can be obtained by changing the beta decay rates, they do not show the specific simulations that are sensitive

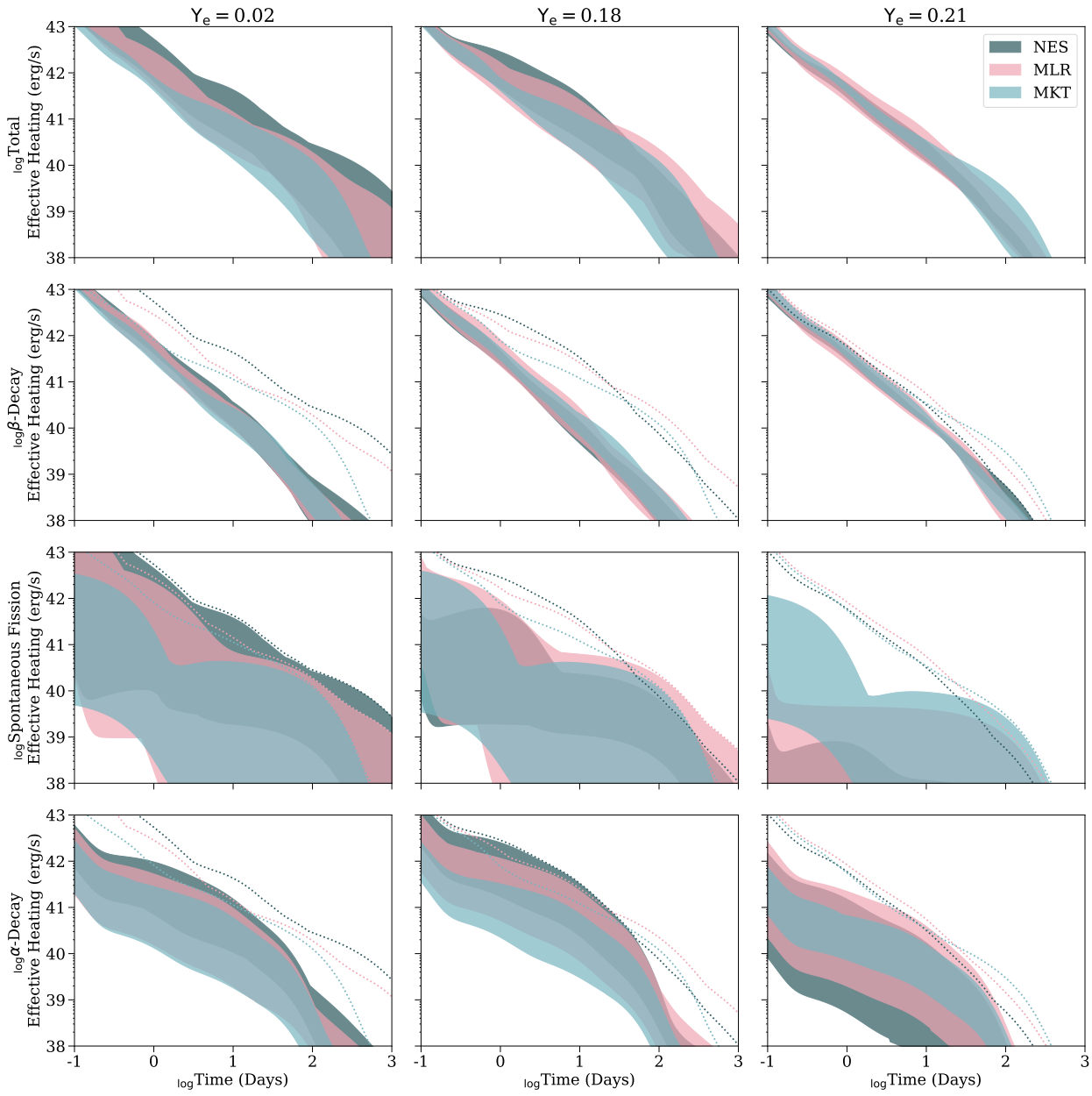


Figure 4.3: Range of effective heating rate predictions for all nuclear mass models from Table 4.1 when a single Y_e trajectory is considered. Looking at the columns from left to right, the initial electron fraction increases from 0.02 to 0.18 to 0.21. The width of each band corresponds to the range of heating predictions for the NES (dark blue), MLR (pink), or MKT (light blue) simulations with the nine different mass models and both 50/50 as well as K&T fission daughter product distributions for which we calculate heating. For comparison, the maximum total heating is shown for each set of simulations as a series of dotted lines.

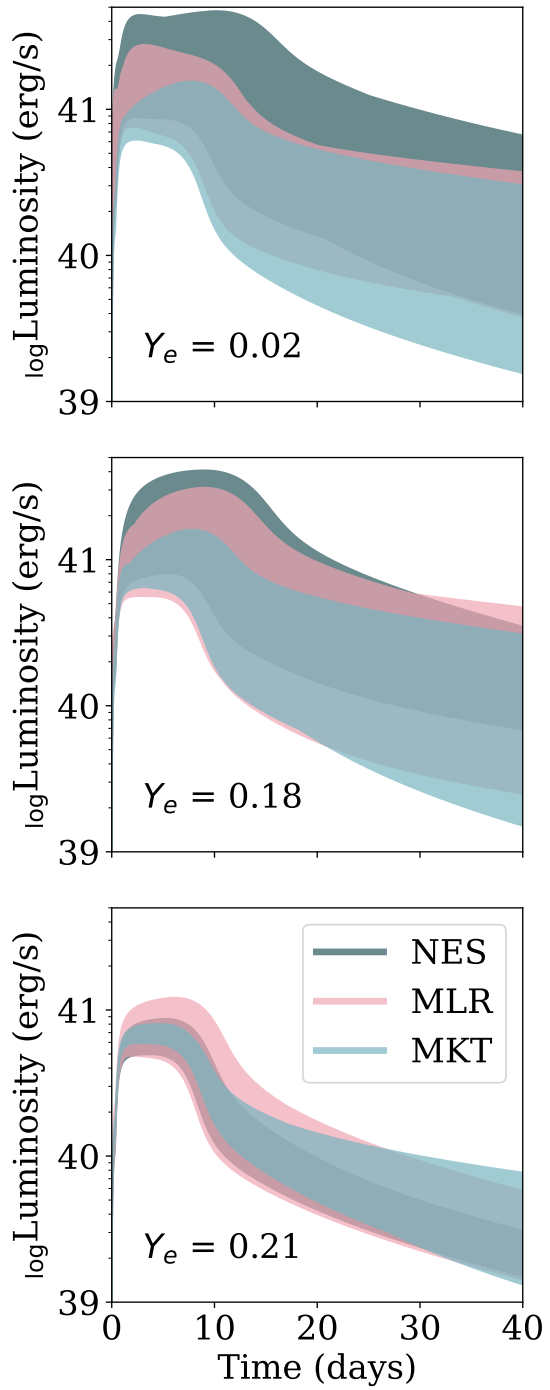


Figure 4.4: Uncertainty range of analytic light curve models for all nine theoretical nuclear models from Table 4.1, when a single Y_e trajectory is considered, with the calculation carried out to 40 days post-merger. The initial electron fraction increases from 0.02 to 0.18 to 0.21 from top to bottom. The width of each band corresponds to the range of luminosity predictions when the NES (dark blue), MLR (pink), or MKT (light blue) beta decay rates are used, and include both 50/50 and KT fission yields.

to these changes. The predictions of heating, and therefore of the light curve, for some mass models are relatively insensitive to the beta decay rates. On the other hand, the predictions from other mass models show substantial sensitivity to the beta decay rates. To illustrate this point, we have separated the total heating rate results by mass model in Table 4.3.

For easier comparison, we list the average ratio of total heating for NES:MLR and MKT:MLR. We also list the ratio of luminosity in parentheses, averaged over two different time periods: 1-10 days and 10-100 days. For both the average heating as well as the average luminosity, we highlight those instances where using a different set of beta decay rates results in a change of 50% or more in bold text. In the following discussion, we refer to these models with the format `nucarmodel.ye`.

The heating at the later timescale of 10-100 days is in many instances dominated by the spontaneous fission of the long-lived ^{254}Cf , which is a marker for actinide production. However, some models, such as the HFB models, facilitate the contribution from additional spontaneous fission heaters during this time. On the other hand, models with lower fission barrier heights tend to suppress these extra possible contributions to the fission heating, leaving only that of ^{254}Cf (Zhu et al. 2021; Barnes et al. 2021).

During the earlier time period of 1 - 10 days, the difference in total heating stems largely from competition between spontaneous fission, alpha decay, and beta decay heating. This highlights the sensitivity of some mass models to both Y_e and beta decay rates. For example, in the case of `sly4.18`, we find that the NES simulations show approximately 60% of the total heating coming from alpha decay by 5 days. Meanwhile, the corresponding MLR simulation is dominated by beta decay with a contribution from alpha decay that only rises to about 40% by 7 days. Similarly, in the case of `etfsi.18`, the MLR simulations show more than 80% of the total heating coming from alpha decay as early as 2 days. When the MKT rates are used, there is still a significant contribution from alpha decay, but only up to a maximum of about 64% around 6 days.

In both these cases, it was the alpha decays of ^{212}Po , ^{214}Po , or ^{216}Po that were among the top most significant contributors to the total heating. These lie in a region where nuclei undergo alpha decay on very short timescales and with a relatively large Q-value. Because of the very short timescales on which these decays occur, it is actually the populations of ^{224}Ra and ^{222}Rn (with half-lives of 3.6 and 3.8 days, respectively) that determine the overall contribution of the decays of their daughter polonium isotopes. The alpha decay feeders into, for example, ^{224}Ra and ^{222}Rn decay on timescales that are too slow (with half-lives of 1.9 years and 1600 years, respectively) to be directly responsible for differences in heating on a timescale of a few days. Thus we conclude that the main source of differences lies in the unmeasured beta decay rates feeding into ^{224}Ra and ^{222}Rn , as well as directly into $^{212-216}\text{Po}$ (highlighted in Figure 4.5); these are critical for determining the amount of material that is available for alpha decay heating, thereby determining the dominant source of total heating. We point out the consistency of this result with those of Wu et al. (2019).

We find that it is the cumulative effect of slight differences in the beta decay rates in the large feeder region, rather than any one specific feeder nucleus. The use of overall slower rates (NES) feeding into this alpha decay region resulted in a large enough heating contribution from alpha decay to dominate

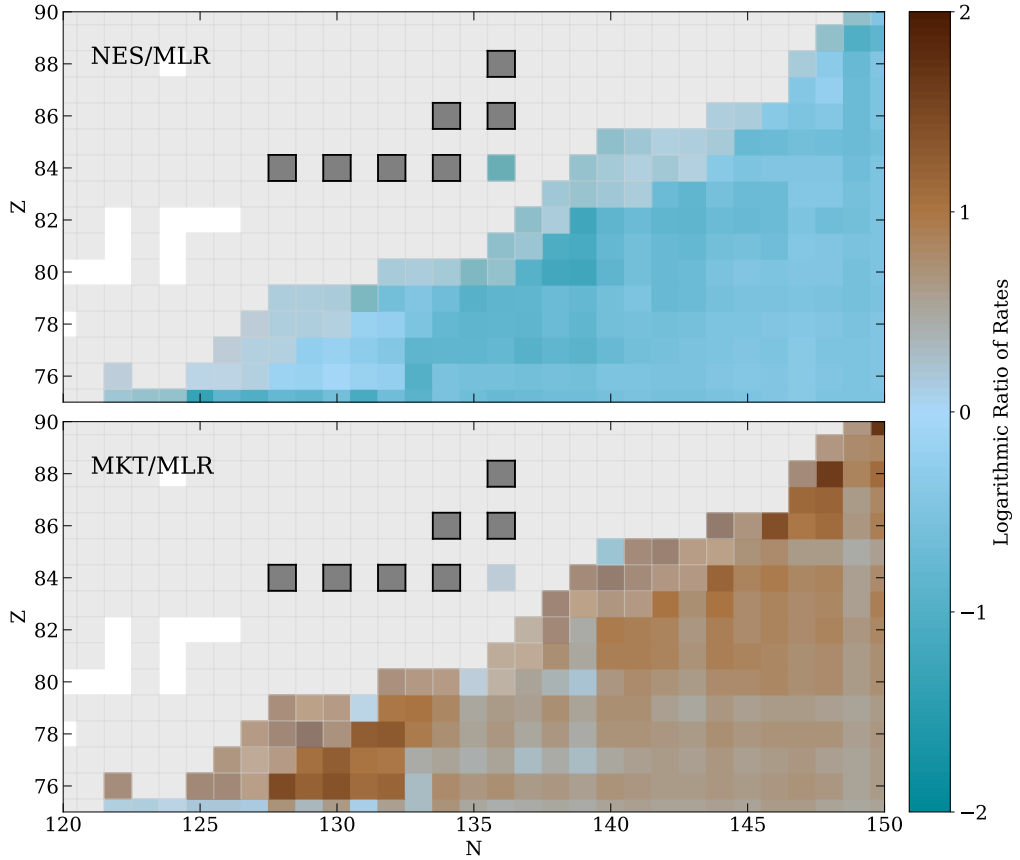


Figure 4.5: Ratio of beta decay rates used in NES:MLR (top) or MKT:MLR (bottom) calculations in the region feeding into important alpha decay heaters (outlined in black boxes) identified in, for example, sly4.18. We show here only the rates subject to theoretical models; those covered by the Nubase2016 data set are shown in grey.

significantly over the beta decay heating that determined the total heating (and light curve) at earlier times.

Spontaneous fission reactions occurring on time scales of days have the largest potential to make a significant difference in the overall heating, as well as the light curve, due to the large Q-values involved as well as the high thermalization efficiency of the reaction products. We find that, especially in the cases using the HFB theoretical nuclear models, spontaneous fission heating has the potential to dominate the total heating as early as 1 day post-merger. The enhanced heating seen in hfb22.02, hfb27.02, and hfb27.18, for example can be attributed largely to differences in the predicted spontaneous fission heating rates. However, there is still a great deal of variety.

By one day post-merger, hfb22.02 shows approximately 77% of the total heating as coming from spontaneous fission heating, compared to only 33% at the same time in the corresponding MLR simulation. By three days, the spontaneous fission heating in the MLR simulation loses out to beta decay heating, while the NES simulation shows it continuing to dominate the total heating out past ten days. There are two mechanisms largely responsible for this behavior. One involves directly competing theoretical branching ratios for potential fission heaters. The colored regions of Figure 4.6 indicate where this occurs, and show the theoretical branching ratios for alpha decay, spontaneous fission, and beta decay. We found that the isotopes ^{272}No and ^{271}Lr appeared to consistently be responsible for a large part of the total heating in NES simulations. The significantly slower beta decay rates predicted in these cases allowed for the spontaneous fission mechanism to compete with beta decay. Contrarily, the beta decay rates predicted in MLR and MKT are fast enough to yield a beta decay branching ratio of almost 100%.

The isotopes of rutherfordium ($Z=104$) appeared to contribute to different degrees in the NES and MLR calculations, yet were not among the top heaters in the MKT calculation. In NES calculations, the heavier isotopes ($N=168,169,172$) appeared to contribute the most to the total heating at early times. For example, the spontaneous fission of ^{273}Rf alone was responsible for approximately 28% of the total heating at one day post-merger. On the other hand, it was the "lighter" isotopes ($N=166,167$) that contributed the most to the total heating in MLR calculations, and did so for a more extended period of time in both MLR and NES calculations.

We attribute this to the second mechanism responsible for differences in the role of fission in our calculations: differences in feeder decay chains that build up different abundances available for decay. One very obvious example of this is that of ^{271}Db . This isotope only appears in the MLR calculation, as this is the only one in which decay into it is allowed. Furthermore, in the MLR calculation in which it appears, the heating from its decay via spontaneous fission competes with or even exceeds that of alpha decay, despite a very small fission branching.

Table 4.3: Average of the ratios of total effective heating using NES or MKT to total effective heating using MLR beta decay rates, over different time periods. In the 1-10 days column, the average ratio of bolometric luminosity is listed in parentheses. Bold-faced values indicate an average change of $\pm 50\%$ or more.

| Nuclear Model | Y_e | 1-10 Days | | 10-100 Days | |
|---------------|-------|----------------------|----------------------|--------------|--------------|
| | | NES | MKT | NES | MKT |
| SLY4 | 0.02 | 1.616 (1.338) | 0.856 (0.917) | 1.583 | 0.761 |
| | 0.18 | 1.797 (1.642) | 1.015 (1.217) | 2.662 | 0.937 |
| | 0.21 | 1.174 (1.112) | 1.469 (1.374) | 1.078 | 1.118 |
| UNEDF1 | 0.02 | 1.166 (1.231) | 0.823 (0.888) | 1.182 | 1.009 |
| | 0.18 | 1.517 (1.404) | 0.557 (0.657) | 1.027 | 0.454 |
| | 0.21 | 0.878 (0.904) | 1.167 (1.16) | 0.801 | 1.125 |
| DZ33 | 0.02 | 1.674 (1.459) | 0.678 (0.82) | 2.224 | 1.089 |
| | 0.18 | 1.631 (1.416) | 0.432 (0.549) | 0.938 | 0.849 |
| | 0.21 | 0.416 (0.504) | 0.656 (0.709) | 0.384 | 1.376 |
| ETFSI | 0.02 | 1.114 (1.042) | 0.553 (0.683) | 1.779 | 1.432 |
| | 0.18 | 1.24 (1.179) | 0.333 (0.499) | 1.799 | 0.841 |
| | 0.21 | 0.923 (0.914) | 1.241 (1.263) | 1.12 | 1.249 |
| FRDM2012 | 0.02 | 1.27 (1.089) | 0.548 (0.752) | 1.438 | 0.633 |
| | 0.18 | 1.377 (1.261) | 0.453 (0.556) | 0.785 | 0.333 |
| | 0.21 | 0.538 (0.589) | 0.642 (0.692) | 0.318 | 0.822 |
| HFB22 | 0.02 | 6.591 (2.806) | 1.215 (0.529) | 4.528 | 1.501 |
| | 0.18 | 1.069 (0.993) | 0.412 (0.551) | 0.437 | 0.333 |
| | 0.21 | 0.895 (0.902) | 1.177 (1.2) | 0.949 | 3.147 |
| HFB27 | 0.02 | 2.002 (1.74) | 0.26 (0.348) | 2.085 | 0.399 |
| | 0.18 | 1.177 (1.083) | 0.302 (0.462) | 0.697 | 0.299 |
| | 0.21 | 0.962 (0.952) | 1.264 (1.27) | 1.011 | 3.158 |
| TF | 0.02 | 1.25 (1.068) | 0.406 (0.761) | 1.171 | 0.406 |
| | 0.18 | 1.078 (1.11) | 0.586 (0.786) | 1.818 | 0.364 |
| | 0.21 | 0.642 (0.719) | 0.54 (0.634) | 0.584 | 0.282 |
| WS3 | 0.02 | 1.549 (1.277) | 0.729 (0.856) | 1.918 | 0.976 |
| | 0.18 | 1.293 (1.253) | 0.578 (0.664) | 0.709 | 0.828 |
| | 0.21 | 0.886 (0.893) | 1.389 (1.33) | 1.131 | 4.588 |

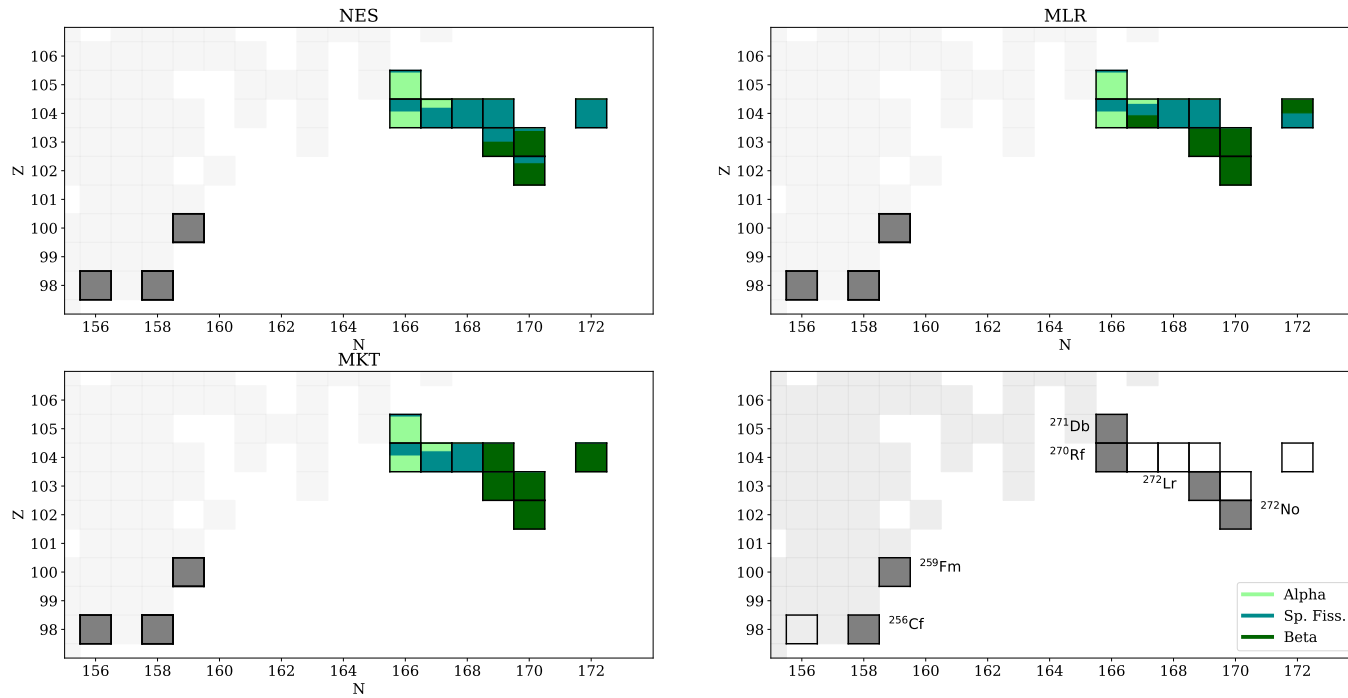


Figure 4.6: Theoretical branching ratios for a selection of key nuclei that have the potential to be important spontaneous fission heaters, as identified in, for example, hfb22.02. The grey-filled isotopes have experimentally determined values; the colored isotopes remain unmeasured. Light green, teal, and dark green represent the branchings expected for alpha decay, spontaneous fission, and beta decay, respectively. In the bottom right panel, we show the chemical names for highlighted isotopes for ease of identification.

This difference in populations also affects the extent to which fission heaters with measured rates are able to contribute to the total heating. These are also highlighted in Figure 4.6, and include ^{254}Cf , ^{256}Cf , and ^{259}Fm . In the MKT calculation, the population of ^{259}Fm is blocked via beta decay. The population of its alpha decay feeder, ^{263}No , is also blocked via beta decay, resulting in ^{259}Fm not being able to contribute significantly to the heating in MKT calculations. However, in NES calculations, enough material is able to decay into ^{259}Fm such that its contribution to the spontaneous fission heating is significant; alone it is responsible for roughly 38% of the total heating at 2 days post-merger.

While these calculations represent the results obtained by using a single- Y_e trajectory, they highlight the influence that the choice of mass model can have when combined with Y_e . The use of certain mass models with a given Y_e unlocked a wide variety of potential heaters that impacted the evolution of the light curve. We emphasize that experimental data for several of these unmeasured isotopes would prove highly valuable in constraining this uncertainty.

4.4.2 Combined Trajectories

Since it is expected that element synthesis will occur in outflows with a range of electron fractions, we now turn to the variation in outcomes that is produced by employing different sets of beta decay rates in scenarios with multiple trajectories but using a single mass model. Accordingly, Figure 4.7 shows the abundances for nuclei $Z > 50$ obtained at 10 GYr post-merger from the linear combinations of individual Y_e trajectories (*combined trajectories*) using *only* the FRDM2012 mass model, as described in Section 4.3.1. The coloring of the individual lines corresponds to those in Figure 4.2, i.e. more brown representing a combination weighted toward low- Y_e and bluer representing one weighted toward high Y_e . The left, center, and right columns represent NES, MLR, and MKT simulations, respectively. The top and bottom rows show results using 50/50 and K&T fission yields, respectively. We note that in all cases we have a substantial fraction of high Y_e ($Y_e > 0.2$) material that has little to no fission.

As in the previous section, we are interested in investigating the evolution of the nuclear heating for these combined trajectories and its impact on the light curve. The large panels of Figure 4.8 show the heating as a function of time for each of the combined trajectories. Similar to the ratios shown in Table 4.3, we compute the ratio of the heating for each combined trajectory when NES and MKT beta decay rates are used compared to MLR. We show these graphically in Figure 4.8. Because of the potentially large contribution from fission to the heating, we also perform a set of similar calculations using *only* the HFB22 mass model. Figure 4.9 shows the evolution of the heating when this mass model is used.

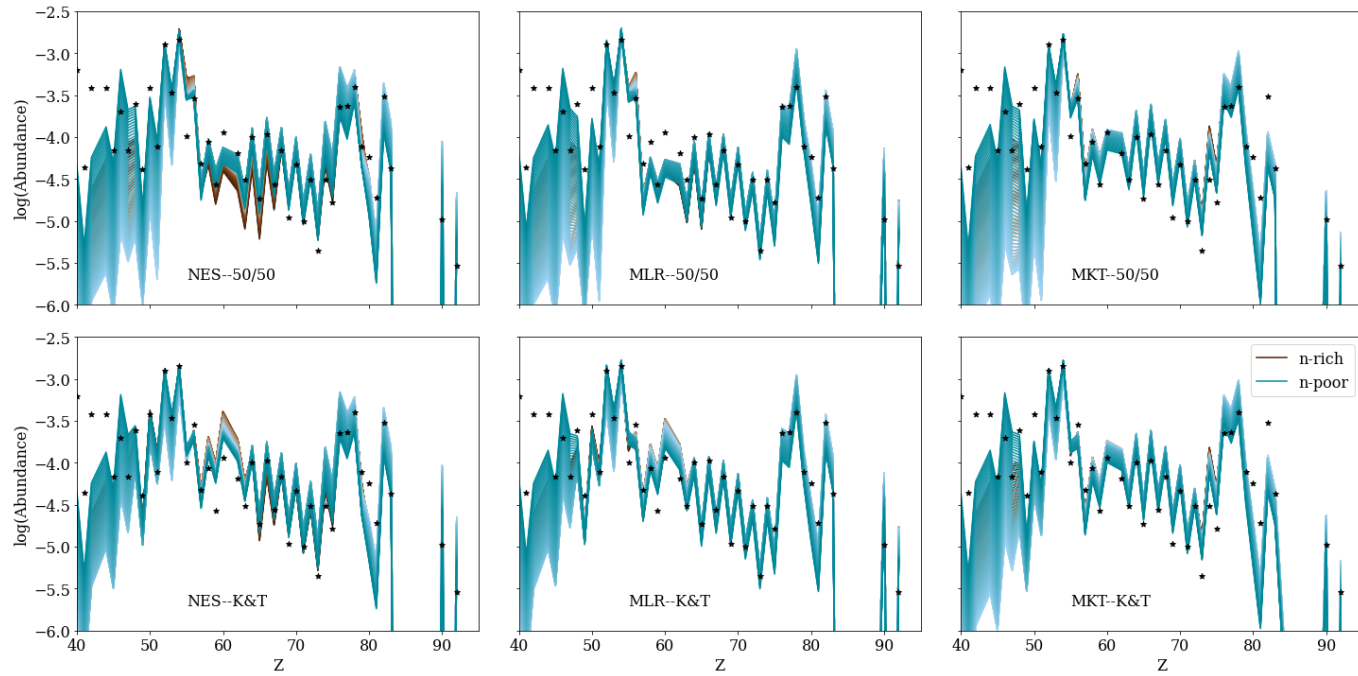


Figure 4.7: Abundance patterns at 10 GYr for combined trajectories displayed in Figure 4.2 using the FRDM2012 mass model, with the same coloring convention (brown representing more neutron-rich combinations, and blue more neutron-poor). Solar r-process residuals (Asplund et al. 2009) are plotted as black stars, scaled such that the abundance of bromine ($Z = 35$) is $10^{-2.5}$.

As in Figure 4.3, the top row of Figures 4.8 and 4.9 shows the total heating for each of the combined trajectories, with the ratio to MLR immediately underneath for NES and MKT calculations. Similarly, the second, third, and fourth rows show the individual contributions from beta decay, spontaneous fission, and alpha decay heating, respectively. As before, the total heating is shown as faint grey lines for comparison.

When the FRDM2012 mass model is used, we find the heating out to at least one day is dominated by beta decay for all three beta sets of beta decay rates. As expected, this varies more when the HFB22 model is used, and we find more of a dependence on the beta decay model used. Furthermore, in the FRDM2012 case, the beta decay heating is roughly independent of the combined trajectory, as can be seen from the relatively narrow width of the bands in the second row of Figure 4.8. The ratios of the beta decay heating with NES or MKT, compared to MLR, tend to stay close to one.

Each of the composite trajectories has a significant amount of high- Y_e material and this can "dilute" the heating contributions from spontaneous fission and alpha decay. Indeed, when the FRDM2012 model is used, the spontaneous fission heating does not appear to significantly dominate the shape of the total heating until tens of days, for any of the combined trajectories. We find the most potential for early-time (order days) contribution to the total heating from spontaneous fission in the low- Y_e weighted NES simulations. This is reflected in the cases where the HFB22 model is used; the lowest average Y_e NES calculations show the most robustly dominant contribution from spontaneous fission. Similarly, the effect of the alpha decay heating is diluted enough that for no combined trajectory does it ever dominate the total heating, whether the FRDM2012 or HFB22 model is used. However it is apparent from Figures 4.8 and 4.9 that the description of the total heating is not complete without accounting for both the spontaneous fission as well as the alpha decay heating.

We see the combined trajectories with the largest proportions of the lowest- Y_e material showing the most spontaneous fission heating. As a larger proportion of high- Y_e material is included, we begin to see this dilution effect, and the amount of spontaneous fission heating decreases accordingly. Section 4.4.1 also showed the largest amount of alpha decay heating in the "semi-neutron rich" (Y_e of 0.18) case. This behavior is reflected in the fourth rows of Figures 4.8 and 4.9, and is most apparent for the NES simulations. There is an increase in the contribution of alpha decay heating as more neutron-rich material is included until a point where the material becomes too neutron-rich and material is more efficiently deposited into the higher-Z fissioning region, thus contributing less to the alpha decay heating.

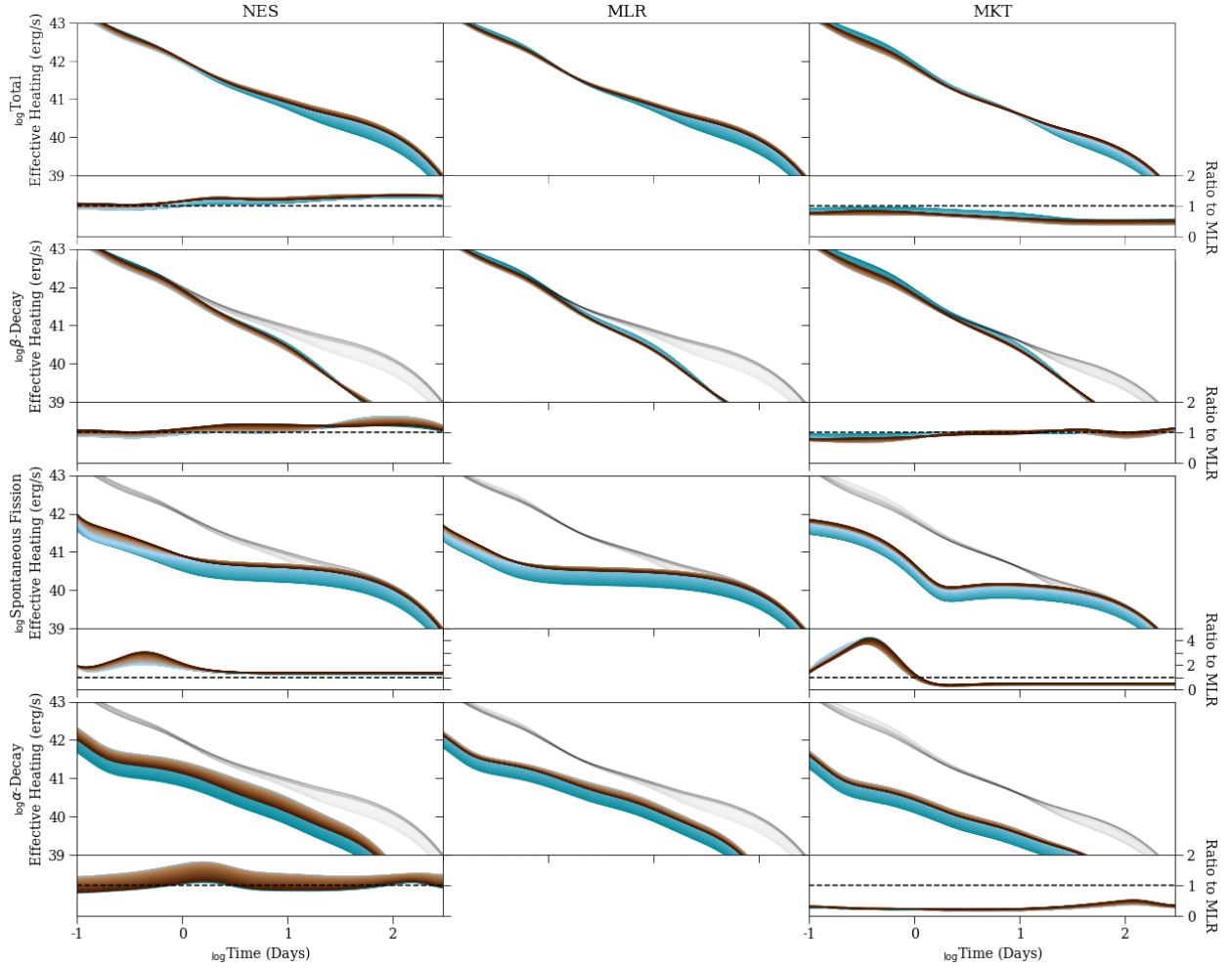


Figure 4.8: Range of effective heating rate predictions using the FRDM2012 mass model with 50/50 fission product yields when composite- Y_e trajectories are considered. From left to right, the beta decay description used is NES, MLR, MKT. The color scheme corresponds to that shown in Figure 4.2. As in Figure 4.3, we replicate the total heating curves shown in the top row in the bottom three rows as light grey lines for easier comparison.

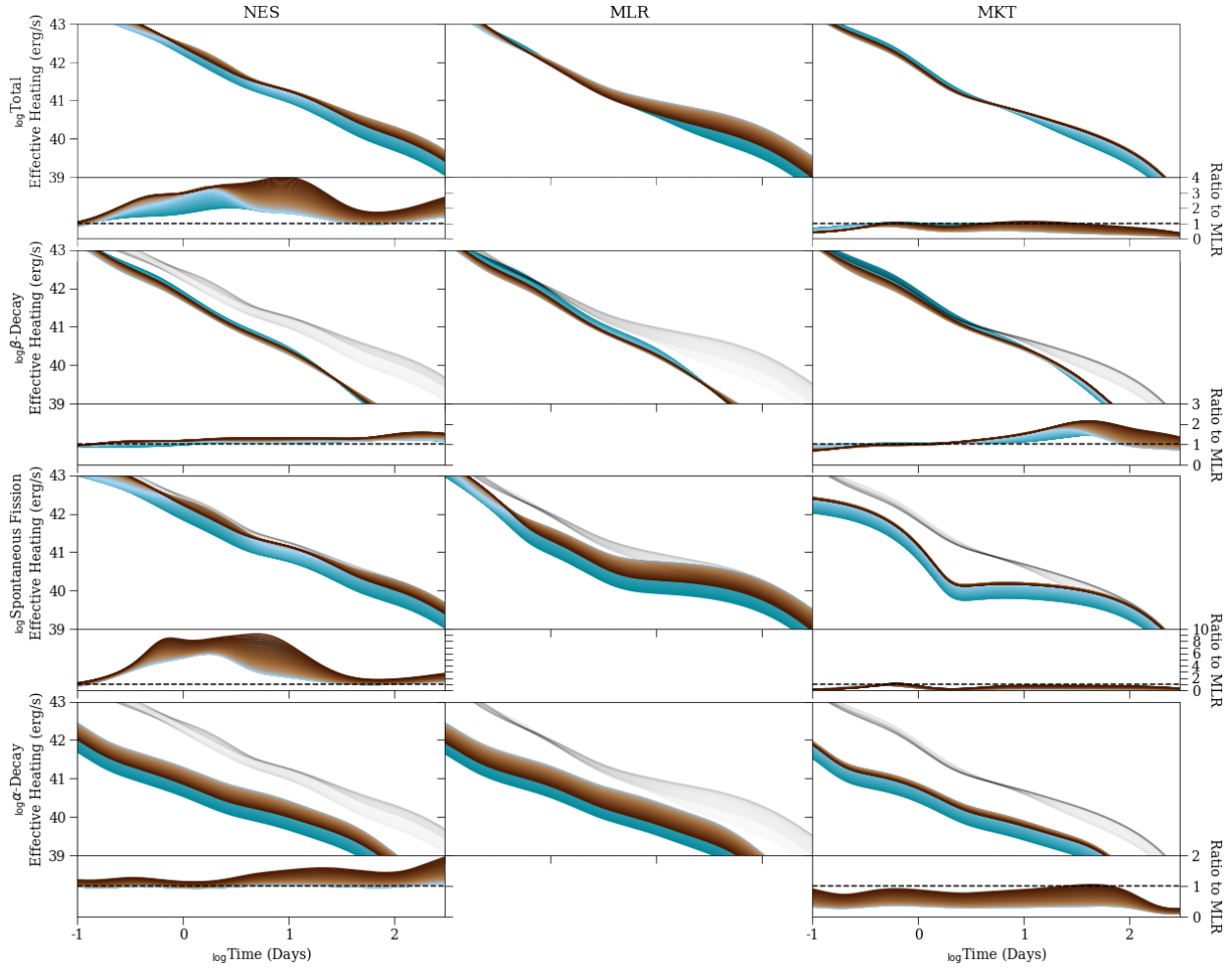


Figure 4.9: Range of effective heating rate predictions using the HFB22 mass model when composite- Y_e trajectories are considered with 50/50 fission product yields. From left to right, the beta decay description used is NES, MLR, MKT. The color scheme corresponds to that shown in Figure 4.2. As in Figure 4.3, we replicate the total heating curves shown in the top row in the bottom three rows as light grey lines for easier comparison.

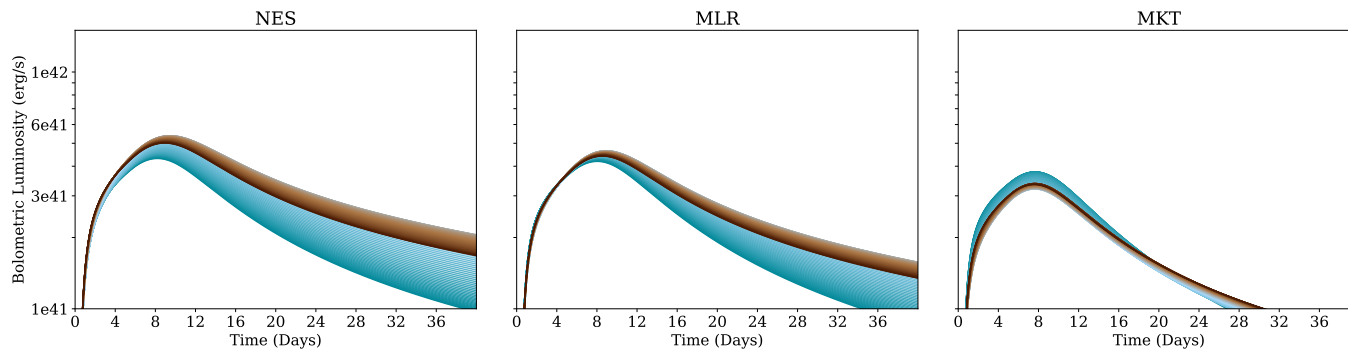


Figure 4.10: Uncertainty range of analytic light curve models for FRDM2012 nuclear model with multiple- Y_e composition using 50/50 fission product yields. From left to right, the beta decay description used is NES, MLR, MKT. The color scheme corresponds to that shown in Figure 4.2, with the most striking blue representing the behavior of the most neutron-poor material and the darkest brown that of the most neutron-rich material.

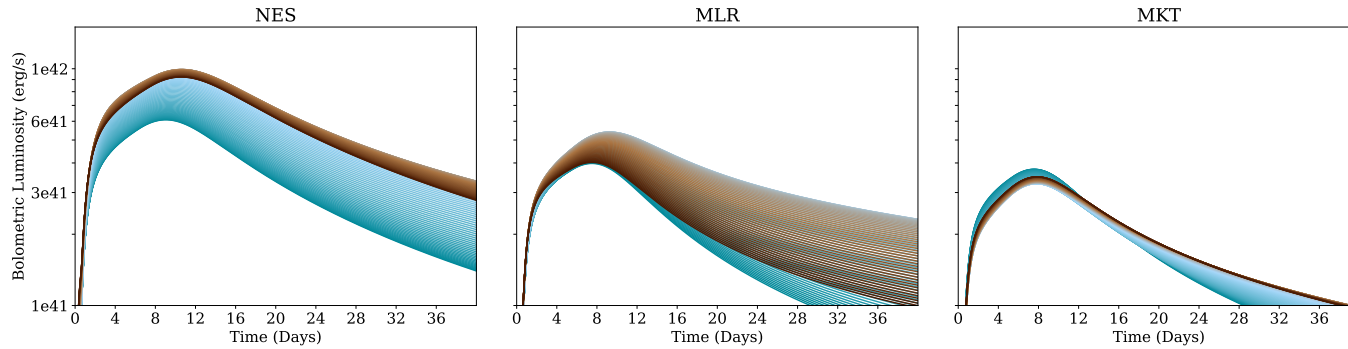


Figure 4.11: Uncertainty range of analytic light curve models for HFB22 nuclear model with multiple- Y_e composition using 50/50 fission product yields. From left to right, the beta decay description used is NES, MLR, MKT. The color scheme corresponds to that shown in Figure 4.2, with the most striking blue representing the behavior of the most neutron-poor material and the darkest brown that of the most neutron-rich material.

In the case of both spontaneous fission and alpha decay, the point in time at which all these effects occur depends on the beta decay rates. For example, the number of days after the merger at which beta decay no longer closely approximates the total heating occurs sooner in NES simulations than MLR, which in turn occurs sooner than in MKT simulations. We find that the contribution of alpha decay heating has the most potential to be significant in NES simulations that are more heavily weighted toward the middle of our Y_e range. There is also a more significant difference between the potential for significant alpha decay heating for mid- Y_e combined trajectories compared to those weighted toward low Y_e for NES simulations than both MLR and MKT simulations. In these latter cases, there is more similarity between low- and mid- Y_e weighted combined trajectories. This is consistent with the result obtained in Section 4.4.1, where we found the largest contribution to alpha decay heating to be in the $Y_e = 0.18$ case in NES simulations.

We find that the use of a different set of beta decay rates changes the time scales on which these differences appear, and the extent to which they affect the total heating. However, when these differences are propagated through the light curve calculations, we find that the differences are more subtle. We show the light curves resulting from the combined trajectory effective heating results in Figures 4.10 (for the FRDM2012 case) and 4.11 (for the HFB22 case), following the same coloring convention as the heating. The left, middle and right panels show the light curves for NES, MLR and MKT simulations, respectively. In all three cases, we find that the overall shapes of the light curves are consistent for all three sets of beta decay rates, e.g. there are no plateaus or bumps present in some but not others.

When comparing beta decay rates, for a given mass model, the most apparent difference in the light curves lies in the behavior after approximately 4 days. The NES and MLR simulations show similar behavior with the NES simulations yielding a higher peak luminosity for mid to high- Y_e weighted combined trajectories. In addition to a smaller peak magnitude, the low- Y_e weighted combinations show an earlier peak than the more neutron rich trajectories. Furthermore, these tend to decay more quickly. The MKT calculations yield slightly different results, with the lowest- Y_e material yielding the largest peak magnitude. This is consistent with the total heating behavior observed in the MKT simulations, shown in the top row of Figure 4.8. We attribute this to the dominant heating mechanisms in MKT calculations being beta decay for a longer period of time, which is largest in the higher- Y_e weighted trajectories. Thus the alpha decay heating contribution, which is largest for low- Y_e dominated trajectories, is unable to compete until later in time. This point is reflected in the MKT light curves, in which there is a flip, and the low- Y_e trajectories have the highest luminosity. This is also apparent when comparing between mass models. The combined effect of the NES beta decay rates and the HFB22 model facilitating a large contribution from fission heating yield a significantly larger peak magnitude in the light curve than the same beta decay rates and the FRDM2012 model. Contrarily, even with the HFB22 model, the use of the MKT beta decay rates yields a comparatively small contribution from fission, and the light curve predictions do not vary much between mass models.

4.5 Applications for Nuclear Cosmochronometry

Using the same combined trajectories described in Section 4.3.1, and using only the FRDM2012 mass model, we calculate the ages² of a selection of *r*-process-enhanced, metal-poor stars, as described in Section 4.3.4. We show the range of results of these calculations in Figure 4.12. We emphasize that the choice of mass model will quantitatively influence the results shown in Figure 4.12 and the analysis here is presented only for FRDM masses. The left and right columns of Figure 4.12 use the 50/50 and K&T fission yields, respectively. Each row shows the results for a different star, with actinide-richness increasing from HE1523 (most actinide-deficient) to J0954 (most actinide-boosted). To obtain these ranges, we use the quoted observational values in Table 4.2 for $\log_{\epsilon}(X/Y)_{\text{obs}}$ and the theoretical abundances obtained at 1 GYr post-merger from each individual combined trajectory for $\log_{\epsilon}(X/Y)_0$. For the purposes of Figure 4.12, we have not included observational uncertainties. We do so later in this section.

Theoretical beta decay rate predictions are a critical component of parameterized cosmochronometry studies (Goriely, S. and Arnould, M. 2001; Schatz et al. 2002; Holmbeck et al. 2018b, 2019; Eichler et al. 2019). For example, the use of theoretically calculated lanthanide *and* actinide abundances can yield age estimates that show a substantial spread depending on the choice of beta decay rates (Holmbeck et al. 2018b). We show this effect using our calculations in Figure 4.12. We show the maximum uncertainty in age for the five stars in Table 4.2 from NES (dark blue), MLR (pink), and MKT (light blue) calculations using all three chronometer pairs.

Use of the rare earth - actinide chronometer pairs with NES or MLR simulations tends to produce age estimates that are high relative to the actinide-only chronometer. This effect is most pronounced in actinide deficient stars, as can be seen from top row of Figure 4.12.

We attribute this to an overproduction of actinides relative to rare earths, as shown in Figure 4.13, where we have plotted the composite, i.e. for the combined trajectories, abundances of europium (red), thorium (teal), and uranium (pink). The overproduction is largest for the 50/50 fission yields. This effect is ameliorated with the use of the K&T fission yields since this model spreads out the fission daughter nuclei over a larger range of mass number. In all cases, for a more actinide deficient star, the amount of time that is necessary for the overproduced actinide content to decay to match observed abundances is larger. We see this reflected in Figure 4.12, where the stars are sorted in order of increasing ratio of actinide to rare earth abundance.

In contrast, the use of MKT beta decay rates in some astrophysical conditions yields theoretical initial production (Th/Eu) values that are lower than those observed in some stars. This results in lower ages when Equations 4.12 and/or 4.13 are applied, as compared with the actinide-only chronometer pair. As can be seen in Figure 4.13, MKT tends to produce simultaneously less actinides and more rare earths than do other theoretical formulations of beta decay rates. This effect is most pronounced for stars with a larger actinide enrichment, such as CS31082 and J0954. Again, the effect is mitigated slightly

²We use "age" as a concise way to refer to the time since the enrichment event- not *necessarily* the time since the formation of the star itself.

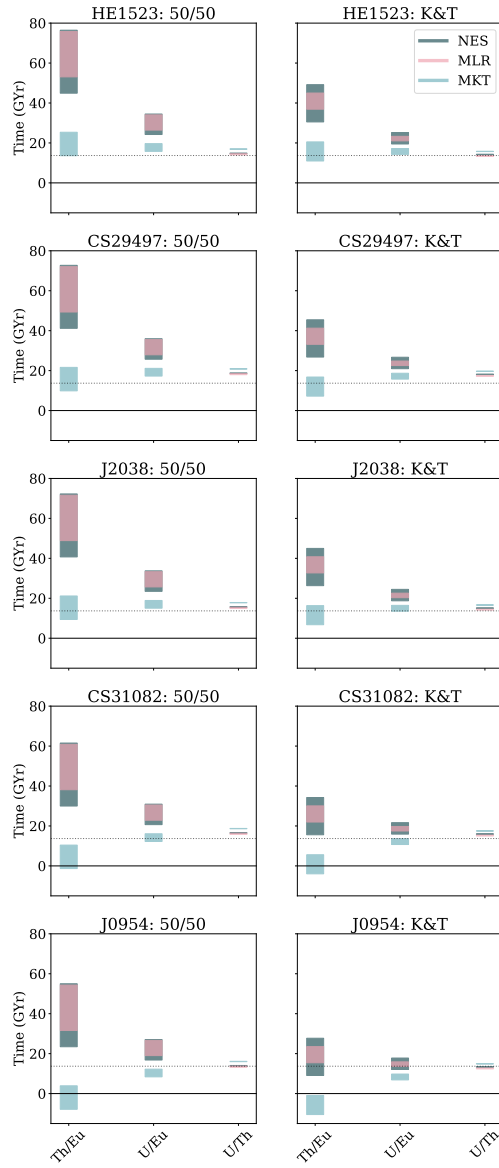


Figure 4.12: Maximum uncertainty from the use of different beta decay rates for the stars listed in Table 4.2, with each row corresponding to a different star. The left column shows ages computed using the 50/50 fission yields, while the right column contains those obtained using the K&T fission yields. As throughout this work, NES calculations are shown in dark blue, while MLR and MKT calculations are shown in pink and light blue, respectively. The regions are filled in to show the range of values obtained using the three different chronometers, as described in Equations 4.12-4.14. Dashed horizontal lines indicate a value of 13.7 GYr; solid horizontal lines indicate a value of 0 GYr.

when using the more diverse fission daughter product distribution (K&T), which increases somewhat the predicted europium yield, as well as the yields between $57 < Z < 63$. Indeed, europium production in K&T simulations shows less sensitivity to beta decay rates than simulations with the 50/50 fission daughter product distribution. The lower actinide population in MKT calculations is consistent with previous works (Holmbeck et al. 2018b; Eichler et al. 2019; Zhu et al. 2021; Barnes et al. 2021), where the relatively fast MKT beta decay rates above the $N = 126$ shell closure (which can be seen in Figure 4.1) were found to inhibit the buildup of a significant actinide population.

4.5.1 Actinide Constraint

While the actinide:lanthanide ratios yield a large spread of results, thorium and uranium are generally produced concomitantly (as can be seen, for example, in their abundance behavior in Figure 4.13), resulting in smaller uncertainties. This feature, and the resulting usefulness of the U/Th chronometric pair has long been discussed in the literature; see, for example, Goriely, S. and Arnould, M. (2001), Ren, J. et al. (2012), Holmbeck et al. (2018b).

In Figure 4.14 we focus on this uncertainty; these results were obtained solely from using variation in the theoretical values of $\log_{\epsilon}(U/Th)$ in our models. Each colored bar corresponds to the range of results we obtain using NES (dark blue), MLR (pink), and MKT (light blue) simulations, along with the 50/50 (plotted on the left) and K&T (plotted on the right) fission yields. We find from this figure that there is more star-to-star variation, than variation from the use of different beta decay rates, fission descriptions, or combined trajectory sets.

We also find here that similar actinide abundances are produced in NES and MLR simulations, while MKT shows consistently different behavior. The NES and MLR simulations produced comparable amounts of thorium as well as uranium, with NES simulations never exceeding a factor 0.8-1.3 times the corresponding MLR simulation abundance. The result of this is largely overlapping age estimates stemming from the actinide chronometers, as seen in Figure 4.14.

In comparison, the MKT simulations yielded roughly only one third the actinide abundances compared to MLR. However, the difference between thorium and uranium production within MKT simulations was small, as can be seen in the bottom panel of Figure 4.13. The overall effect of this translates into larger age estimates for MKT simulations, as shown by the light blue error bars in Figure 4.14 being consistently centered at larger values than the pink or dark blue. We point out, though, that the ratio is not necessarily smaller because either uranium or thorium specifically is less effectively produced. Rather both are inefficiently produced yielding overall smaller abundances.

4.5.2 Chronometric Agreement

An important assumption in Equations 4.12-4.14 is that of a single enrichment event, i.e. that the lanthanide and actinides observed in the r-process enhanced star stem from the same event which occurred at time t_0 . Beyond this, the chronometry equations make no other assumptions and are derived

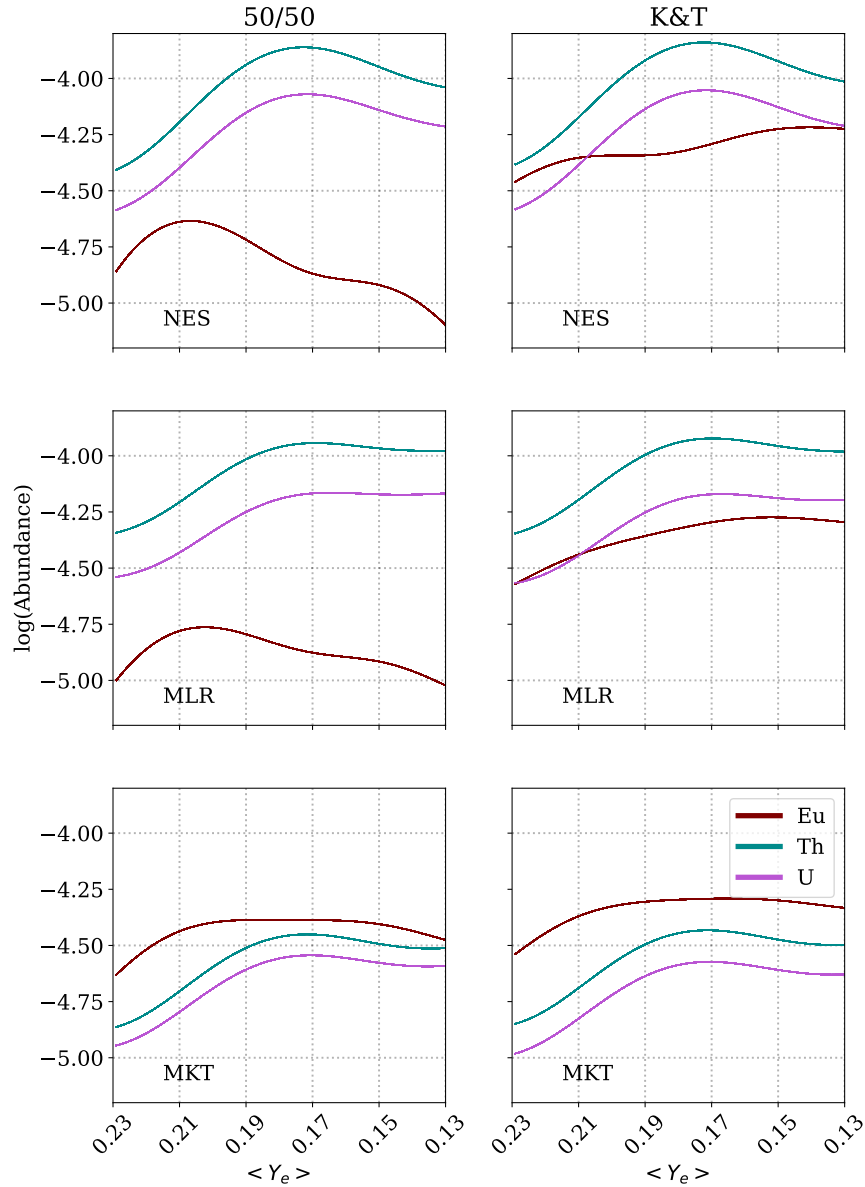


Figure 4.13: Composite values of initial production abundances of europium (red), thorium (teal), and uranium (pink), separated out by beta decay rates used. NES, MLR, and MKT simulations are shown in the top, middle, and bottom rows, respectively. The left column shows results obtained using the 50/50 fission yields, and the right column shows those obtained using the K&T fission yields. The horizontal axis shows average Y_e (with increasing neutron richness) of the combined trajectories.

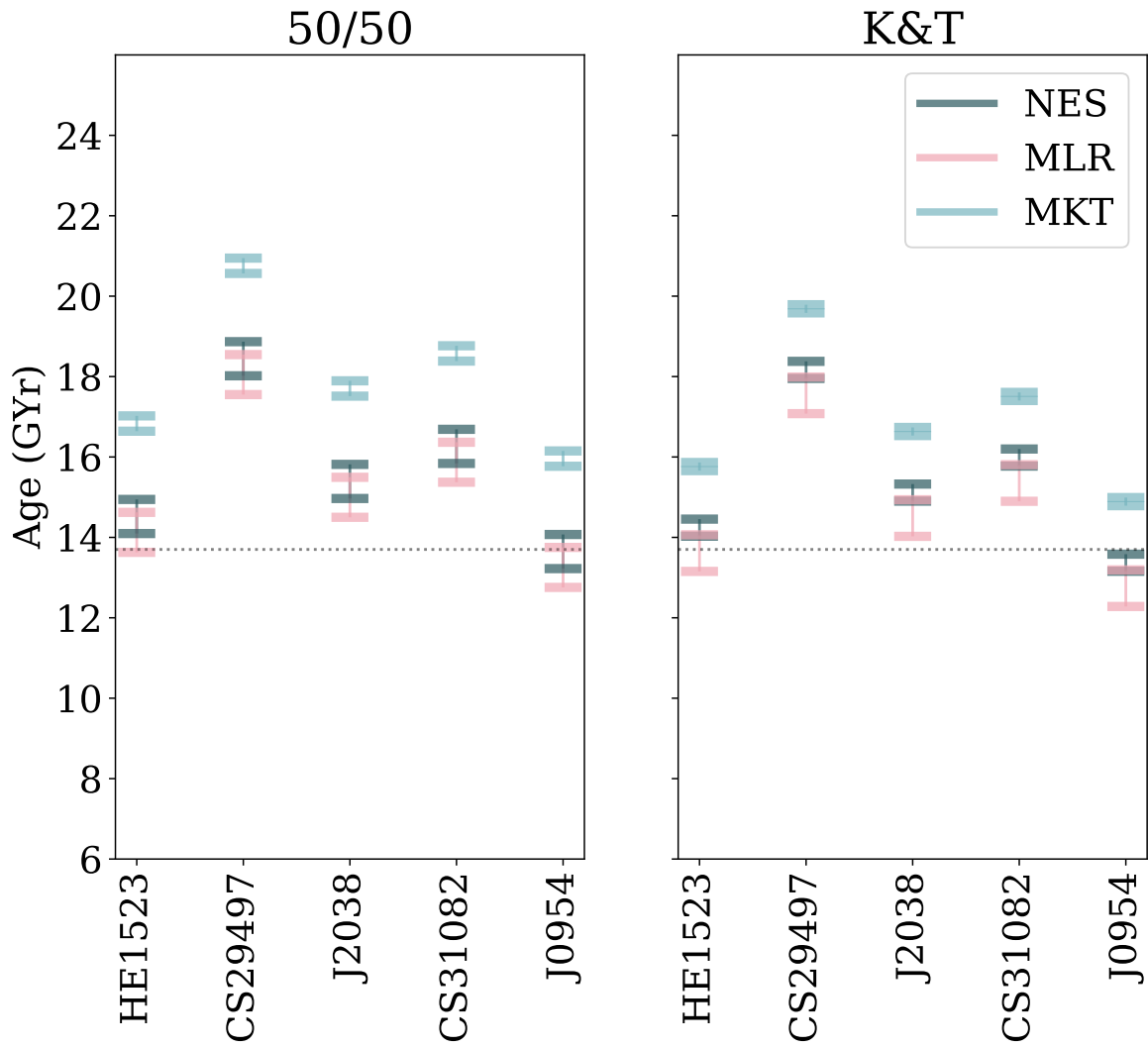


Figure 4.14: Uncertainty in age estimates due to uncertain nuclear physics and Y_e for fixed stellar observations. The ages in this figure are calculated solely using the U:Th abundance. A horizontal dotted line indicates the value of 13.7 Gyr. NES, MLR, and MKT calculations are shown as dark blue, pink, and light blue bars, respectively. The left panel shows results obtained using the 50/50 fission yields while the right panel shows those obtained using the K&T fission yields.

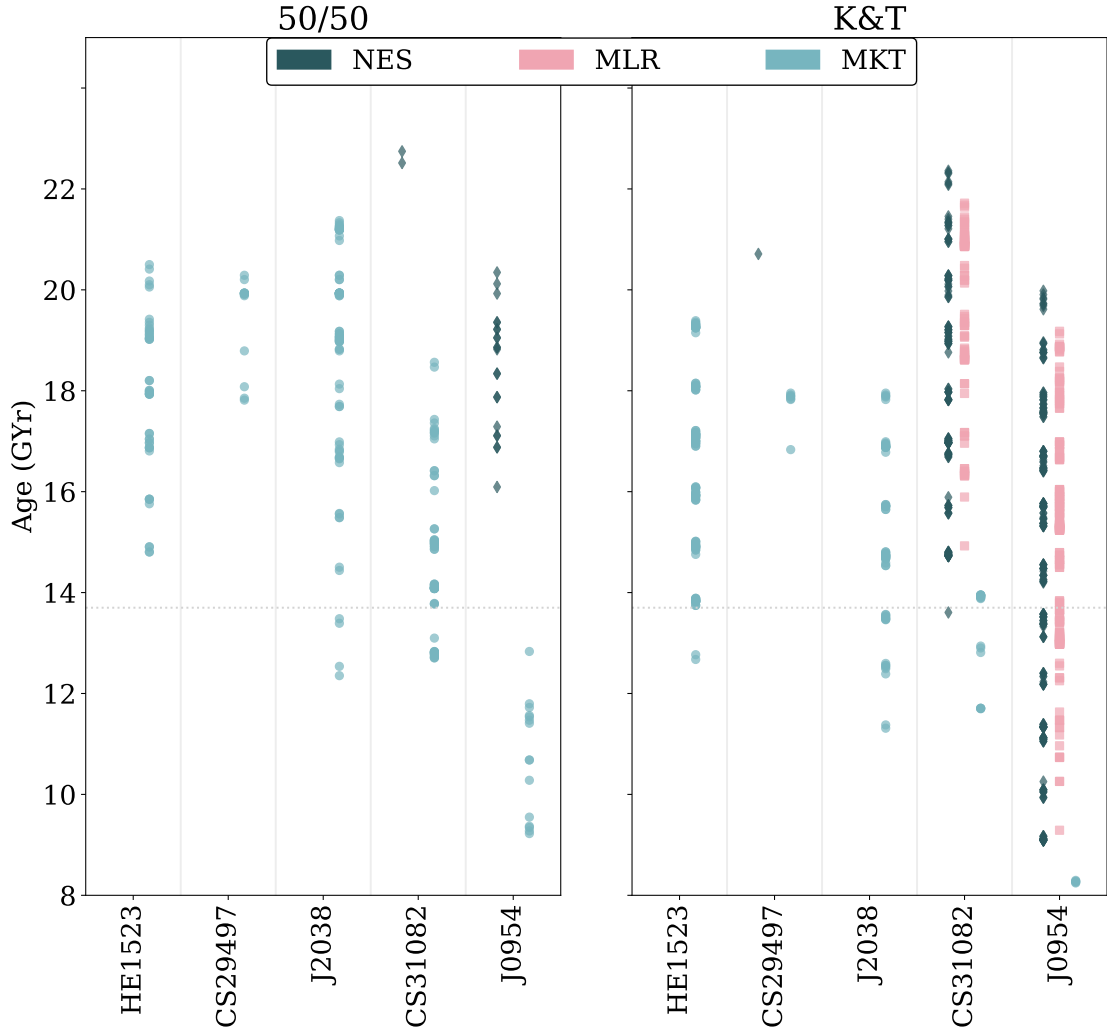


Figure 4.15: Full range of predicted age values for each star when the full range of observational error bars plus the full uncertainty from the composite trajectories are used. Each point represents an age predicted by an individual composite trajectory that shows agreement between all three chronometer pairs. Results in the left and right panels use 50/50 and K&T fission yield descriptions, respectively. NES calculations are represented as dark blue diamonds, MLR as pink squares, and MKT as light blue circles.

from the nuclear decay equation. Hence if the r-process elements in a given star come from a single event and if the abundances from this event have been correctly predicted, then the three chronometers should provide the same age estimates within observational uncertainty.

With this in mind, we begin with our model set which includes all the combinations of trajectories shown in Figure 4.2, each computed for all three different beta decay rates. We then select *only* those models for which each of the chronometers yield the same age within the quoted observational error bars, terming this "chronometric agreement" (or simply "agreement"). We obtain error bars from the observation by calculating the largest and smallest possible values of $\log_e(A/B)$ from the individual error bars for isotopes A and B. We show the results of this procedure in Figure 4.15. We see that for many stars no chronometric agreement exists for our selection of combined trajectories with the MLR and NES rates, consistent with the results of Figure 4.12. However we caution that all our simulations for this analysis were performed with the FRDM mass model, and this conclusion may change when a wider variety of theoretical predictions for off-stability masses are considered.

Furthermore, we have used only the combined trajectories from Figure 4.2, i.e. many of the extremely large values resulting from actinide:lanthanide pairs shown in Figure 4.12 are eliminated from our analysis. Other combinations, particularly those weighted towards even higher values of Y_e (or simply more heavily weighted toward the higher- Y_e range of our selection) could produce agreement for these stars.

On the other hand, for all stars there are some simulations with the MKT rates that produce chronometric agreement, again due to their more limited production of actinides as compared to the rare earths. For each star the range of ages that are in agreement is larger in Figure 4.15 than in Figure 4.14. This is because we have taken into account observational uncertainty in the former.

It is interesting to see what sort of distribution of electron fraction is needed to produce the chronometric agreement. We show instances in which this occurs in Figure 4.16 for all three sets of beta decay rates. As is consistent with Figure 4.15, we find that a very large range of the MKT calculations yield chronometric agreement when observational error bars are taken into account. In the case of the most actinide-poor star, HE1523, both high average Y_e and low average Y_e calculations which make use of the MKT beta decay rates yield chronometric agreement, independent of fission yield. Contrarily, for the stars with the largest actinide enhancement (CS31082 and J0954), the use of MKT beta decay rates only yields agreement when the material is more heavily weighted toward mid and/or low- Y_e values.

For CS31082 and J0954, there is overlap in the NES and MLR calculations that agree when the K&T fission yields are used. This is consistent with previous work that showed agreement with K&T fission yields for J0954 using the MLR and FRDM combination as long as the average Y_e was sufficiently high, and the actinides were "diluted" (Holmbeck et al. 2018b). However, if the fission daughter product distribution is taken to be 50/50, none of the MLR trajectories we have considered yield agreement, as do only a selection of NES calculations with trajectories weighted towards high Y_e . This is in stark contrast to the aforementioned behavior of the MKT calculations, which favor low Y_e weighted trajectories. This contrast is consistent with the abundance patterns resulting from these calculations, as seen in

Figure 4.13. NES calculations more effectively reproduce a large actinide population, to the point of overproducing actinides. Thus only a small amount of low Y_e material is sufficient to produce a large actinide abundance.

We carry our analysis one step further by selecting instances of calculations yielding agreement from those shown in Figure 4.16. For each star, we select a pairing of beta decay description and combined trajectory from those shown in Figures 4.15 and 4.16 in order to directly compare their late-time abundance pattern with both stellar and solar observations. We show the resulting abundances from each of these nucleosynthesis calculations in Figure 4.17. The time to which each individual set of nucleosynthesis calculations is evolved is shown in each subpanel of Figure 4.17. Additionally, we show the trajectory which yielded the particular abundance pattern (as well as the corresponding average Y_e) in the upper right corner of each panel. We find some cases of rare-earth over or underproduction. However, in general we find good agreement with the overall solar or stellar observed abundance patterns above $Z = 60$.

4.6 Conclusion

We performed a targeted study to specifically investigate the impact of global beta decay rates on key aspects of *r*-process nucleosynthesis and kilonova modeling. We combined three sets of beta decay rates with nine different mass models and two fission daughter product distributions for our nucleosynthesis calculations. Furthermore, we considered three single- Y_e trajectories for the full suite of nuclear inputs in order to specifically probe the role of fission heating in our calculations. We also considered several ensembles of trajectories, meant to approximate a multi-component ejecta, for a subset of nuclear inputs. We compared the late-time abundances for these ensembles (obtained at various times) to astronomical observations for five *r*-process-enhanced, metal-poor stars.

For the single Y_e trajectory cases, we found a substantial difference in the predicted total heating from different mass models. The magnitude of this difference was sensitive to the value of Y_e , and almost entirely due to differences in the predicted alpha decay and spontaneous fission heating. This was especially the case in trajectories with initial electron fraction at or below 0.18, as this was where a significant amount of fission or alpha decay could occur. We provided a closer investigation of some instances where the change in beta decay rate translated to an increase of 50% or more in the bolometric luminosity averaged over one to ten days, and identified key nuclei responsible for these differences. We found these increased luminosities could be attributed to both unmeasured nuclei that feed into known nuclei (such was the case for the population of, for example, ^{224}Ra), as well as unmeasured nuclei directly responsible for heating (as was the case, for example, for several isotopes of Rf).

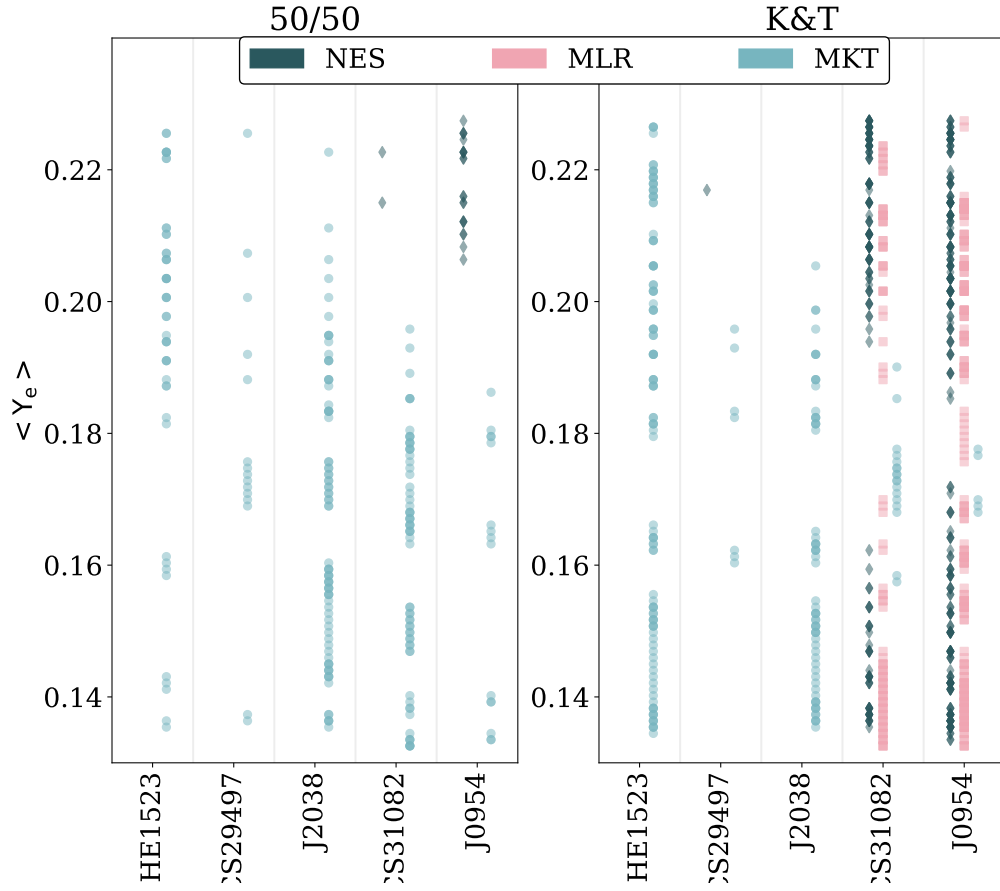


Figure 4.16: Combined trajectories (as described in Section 4.3, represented on the vertical axis by average Y_e) which yield chronometric agreement for each of the stars in our sample. The different beta decay rates are indicated by the marker colors as in Figure 4.14.

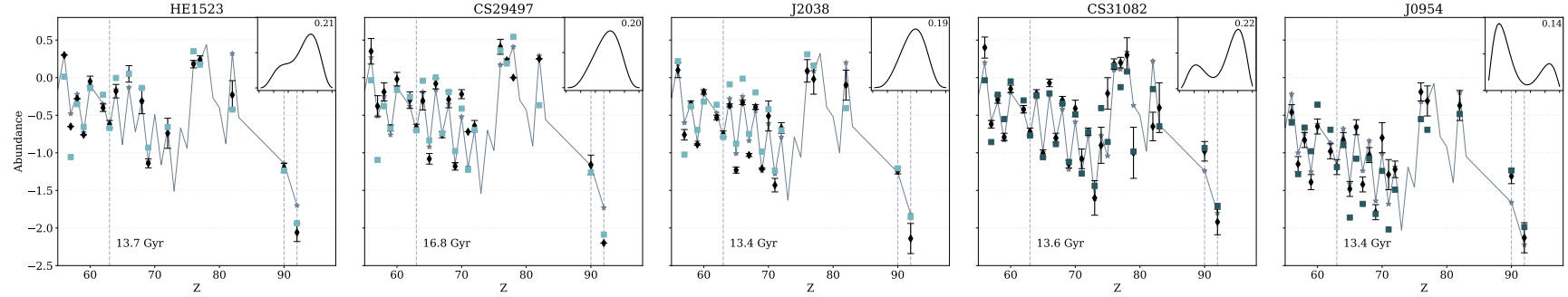


Figure 4.17: Representative theoretical abundance pattern compared to stellar and solar observations when nucleosynthesis calculations are carried out to the times indicated in each panel. The color of the squares representing the theoretical abundances indicate the set of beta decay rates used for that particular calculation, i.e. light blue for MKT and dark blue for NES. In the upper right corner of each panel, we include the weight distribution (as could be extracted from Figure 4.2) used for the specific calculation for which the abundance is shown. The stellar observational values plus their error bars are shown as black diamonds, and the solar r -process residuals from Asplund et al. (2009) are shown as a solid grey line. We additionally show solar r -process abundances as grey stars when those same data points exist for the stellar observation. We highlight the elements europium ($Z=63$), thorium ($Z=90$), and uranium ($Z=92$) with vertical dashed lines, as these were the elements we used to carry out our analysis. For each star, all data is scaled to europium.

We found the behavior of the single trajectory calculations was reflected in the combined trajectories using the FRDM2012 and HFB22 mass models. In these cases, the competition between alpha decay and spontaneous fission with beta decay was not as large as in the single-trajectory cases, as all our combined trajectories had a substantial amount of material with electron fractions above 0.18. However, even in these circumstances, the description of the heating past one day is still incomplete without the contribution from fission and alpha decay. Furthermore, the point in time at which alpha decay and fission begin to influence the overall magnitude of the heating differs, with NES contributions becoming relevant prior to one day, MLR at approximately one day, and MKT predicting a significant contribution closer to ten days.

Finally, we used our calculated abundances of the longest-lived isotopes of europium, thorium, and uranium to perform cosmochronometry calculations for a sample of five *r*-process-enhanced metal-poor stars. We found a larger uncertainty when we used actinide to europium ratios, as opposed to uranium:thorium ratios. This is to be expected given the larger separation between europium and the actinides in the nuclear chart. This is consistent with the general consensus that actinide-pair chronometers are more reliable than actinide:lanthanide pairs. We do consider, however, that the actinide:lanthanide pairs can provide valuable insight, and despite the large uncertainty they contribute, we were able to draw interesting conclusions.

One is that the use of different beta decay rates predicted disparities in the age estimated even from the actinide abundances alone. While there was significant overlap between the predictions resulting from NES and MLR actinide abundances, these differed from the MKT abundances, hinting at the extent to which these different beta decay rates hinder or facilitate actinide production. Secondly, we were able to use the lanthanide abundances, together with the observational uncertainties to place a constraint on the age predictions, in the context of our model. We expand upon previous studies of chronometric dating (Holmbeck et al. 2018b, 2019; Kullmann et al. 2022) using theoretically calculated initial abundances by carefully taking into consideration observational error bars together with multiple chronometer pairs. By doing so, we were able to find theoretically calculated abundances that yielded "chronometric agreement", meaning that all three chronometer pairs yielded the same age. We showed that chronometric agreement depends on the beta decay rates.

We look forward to additional experimental efforts to measure beta decay properties (Gade and Sherrill 2016; Aprahamian et al. 2018; Tain et al. 2018; Horowitz et al. 2019; Savard et al. 2020; Allmond et al. 2020; Wu et al. 2020; Schatz et al. 2022), which will greatly help to reduce this source of uncertainty in the predictions of kilonova light curves and of abundance predictions. We also look forward to new theoretical predictions of the thermodynamic conditions in merging neutron stars, of fission yields and daughter products, and of neutron capture and alpha decay rates, all of which have an important role to play.

CHAPTER
FIVE

MAGNETIC FIELD STRENGTH EFFECTS ON NUCLEOSYNTHESIS FROM
NEUTRON STAR MERGER OUTFLOWS

KELSEY LUND

with

GAIL MC LAUGHLIN, JONAH MILLER, MATTHEW MUMPOWER

The following chapter was published in The Astrophysical Journal, Vol. 964, Number 2 (2024). Some figures have been modified from their original versions to fit dissertation format.

5.1 Abstract

Magnetohydrodynamic turbulence drives the central engine of post-merger remnants, potentially powering both a nucleosynthetically active disk wind and the relativistic jet behind a short gamma-ray burst. We explore the impact of the magnetic field on this engine by simulating three post-merger black hole accretion disks using general relativistic magnetohydrodynamics with Monte Carlo neutrino transport, in each case varying the initial magnetic field strength. We find increasing ejecta masses associated with increasing magnetic field strength. We find that a fairly robust main *r*-process pattern is produced in all three cases, scaled by the ejected mass. Changing the initial magnetic field strength has a considerable effect on the geometry of the outflow and hints at complex central engine dynamics influencing lanthanide outflows. We find that actinide production is especially sensitive to magnetic field strength, with overall actinide mass fraction calculated at 1 Gyr post-merger increasing by more than a factor of 6 with a tenfold increase in magnetic field strength. This hints at a possible connection to the variability in actinide enhancements exhibited by metal-poor, *r*-process-enhanced stars.

5.2 Introduction

The detection of the electromagnetic transient accompanying the binary neutron star merger (NSM) GW170817 lent strong support to these sites as primary sites for the production of the heaviest elements via the rapid neutron-capture process (*r*-process; (Abbott et al. 2017b,c; Alexander et al. 2017; Cowperthwaite et al. 2017; Villar et al. 2017)). The decay of radioactive species produced through the *r*-process powers the electromagnetic transient that follows the merger event (Lattimer and Schramm 1974; Lattimer and Schramm 1976; Li and Paczyński 1998; Metzger et al. 2010; Roberts et al. 2011; Barnes and Kasen 2013; Grossman et al. 2014; Wollaeger et al. 2018; Fontes et al. 2020). Interpretation of the multiwavelength electromagnetic signal, AT2017gfo, points to at least two components to the ejecta (Chornock et al. 2017; Cowperthwaite et al. 2017; Nicholl et al. 2017; Perego et al. 2017). An early, rapidly decaying signal observed peaking at shorter wavelengths is generally attributed to ejecta with negligible lanthanide abundances (Metzger et al. 2010; Roberts et al. 2011; Evans et al. 2017; Miller et al. 2019b; Ekanger et al. 2023). Meanwhile, a dim, slowly decaying component observed at longer wavelengths points toward an underlying “red” component generally attributed to a composition of high-opacity, lanthanide-rich ejecta (Barnes and Kasen 2013; Tanaka and Hotokezaka 2013; Kasen et al. 2017; Tanvir et al. 2017).

One such site considered to be capable of producing these atomically complex lanthanides is material that is unbound from the accretion disk formed around a remnant black hole (Ruffert et al. 1997; Popham et al. 1999; Shibata et al. 2007; Surman et al. 2008; Fernández and Metzger 2013; Fernández et al. 2014; Janiuk, Agnieszka 2014; Foucart et al. 2015; Just et al. 2015; Sekiguchi et al. 2015). As the material is driven off the disk, it is subject to numerous physical processes, each contributing its own uncertainty to the final outcome. One such uncertainty lies in the magnetic fields imprinted on the

post-merger system; magnetic fields have long been recognized as playing an essential role in black hole accretion disks (Blandford and Znajek 1977; Balbus and Hawley 1991; Narayan et al. 2003, 2012), and more recently their importance has been recognized in the role of post-NSM merger disks (Fernández and Metzger 2013; Christie et al. 2019; de Haas et al. 2023). They influence the dynamics of the accretion process, energy transport, and outflow properties.

The magnetorotational instability (MRI) of the magnetized plasma (Velikhov 1959; Balbus and Hawley 1991) leads to the generation of turbulence, enhances angular momentum transport, and is one of the main drivers of the outflow (Shakura and Sunyaev 1973). The magnetic field strength can impact the time it takes for this instability to set in, thereby affecting the accretion rate of material onto the black hole as well as the outflow timescales of material off the disk. These outflow timescales are particularly important for the nucleosynthetic yields of the disk when they come into competition with other timescales, especially weak interaction timescales.

In this work, we aim to investigate the effect of variable initial magnetic field strength on the evolution and nucleosynthetic outcome of the post-merger disk. In Section 5.3, we describe the methods we employ to evolve the post-merger disk as well as to carry out nucleosynthesis. We build upon work carried out in Miller et al. (2019b) and Sprouse et al. (2024) using three-dimensional, general relativistic neutrino radiation magnetohydrodynamics ($\text{GR}\nu\text{MHD}$) to evolve the disk. In Section 5.4, we present the results of our simulations and investigate differences in mass outflow as influenced by initial magnetic field strength, as well as the impact of these differences on the conditions in which nucleosynthesis takes place. In Section 5.5, we show the results of our nucleosynthesis calculations and investigate the contributions to the total abundances from different spatial components of the mass outflow. Finally, in Section 5.6, we interpret the broader implications of our results and provide some concluding remarks.

5.3 Method

We seek to quantify the effect of variable initial magnetic field strength on the mass ejection as well as the nucleosynthesis of heavy elements that occurs in the black hole accretion disk formed after an NSM.

5.3.1 Post-Merger Disk Evolution

We use `nubhlight`, which solves the equations of general relativistic magnetohydrodynamics (GRMHD) with neutrino radiation transport, to evolve the post-merger disk. `nubhlight` builds on a long history of methods spanning almost two decades (Gammie et al. 2003; Dolence et al. 2009; Ryan et al. 2015; Porth et al. 2019). The methods used in `nubhlight` are detailed in Miller et al. (2019a); we include a summary here for convenience and context.

`nubhlight` solves the equations of ideal GRMHD via finite volume methods with constrained transport, and uses Monte Carlo methods to perform neutrino radiation transport. The two are coupled via first-order operator splitting. We use a radially logarithmic quasi-spherical grid in horizon-penetrating

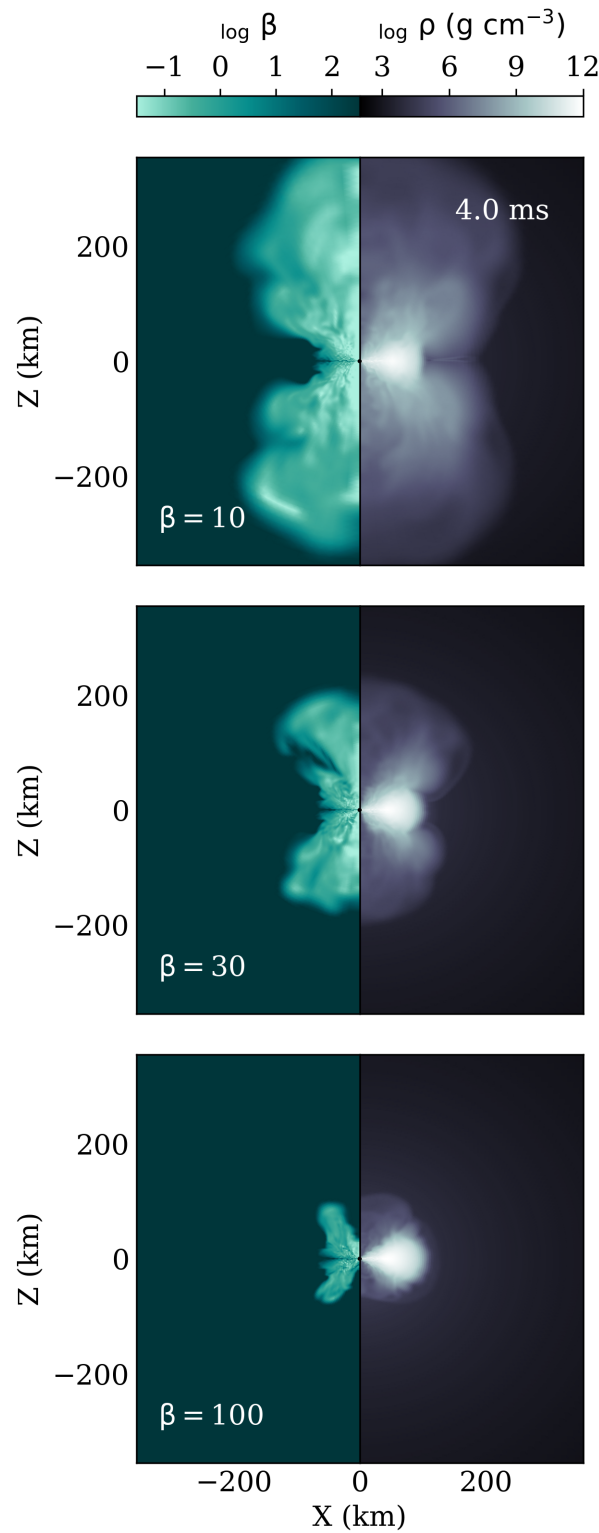


Figure 5.1: The value of β (left) and density (right) for the three different disks with decreasing field strength from top to bottom. The disks are shown at 4 ms physical time post-merger.

coordinates, as first described in McKinney and Gammie (2004), the WENO reconstruction first described in Tchekhovskoy et al. (2007), the primitive variable recovery scheme described in Mignone and McKinney (2007), and the drift-frame artificial atmosphere treatment described in Ressler et al. (2017).

For microphysical data, we use the SFHo EoS, tabulated in stellar collapse format (O'Connor and Ott 2010a,b) and described in Steiner et al. (2013). For neutrino opacities and cross sections, we use the charged and neutral current interactions as tabulated in Skinner et al. (2019) and described in Burrows et al. (2006). Our neutrino-scattering implementation uses a biasing technique to ensure all processes are well sampled, as described in Miller et al. (2019a).

We construct three separate Fishbone and Moncrief (1976) torii, representing post-merger disks, each with a single poloidal magnetic field loop, the strength of which we vary by varying the initial value of the dimensionless parameter, β :

$$\beta = \frac{P_{\text{gas}}}{P_{\text{magnetic}}}, \quad (5.1)$$

using values of 10, 30, and 100, corresponding to the initial value of β at the point of highest pressure. Throughout the text, we refer to these as b10, b30, and b100, respectively, and highlight that a smaller value of β corresponds to a stronger initial magnetic field.

In all three cases, the initial conditions of the disk are chosen to be consistent with the disk presented in Miller et al. (2019b); (which here corresponds to the b100 disk). We begin each simulation with a $0.12 M_{\odot}$ accretion disk surrounding a Kerr (1963) black hole with mass $2.58 M_{\odot}$ and dimensionless spin parameter $a = 0.69$. Each disk is initialized with a uniform $Y_e = 0.1$ throughout. We use a radially logarithmic grid of dimensions $N_r \times N_{\theta} \times N_{\phi} = 192 \times 128 \times 66$ and run the simulation out to $10^4 GM_{BH}/c^3$, which corresponds to 127 ms of physical time given this geometry. At any given time, there are roughly 3×10^7 Monte Carlo packets in the radiatively active region of the simulation.

A post-merger disk simulation must be sufficiently resolved in both the grid and Monte Carlo particles to both capture the MRI and the neutrino-matter interactions. The resolution requirements depend on the fastest-growing wavelength of the MRI and the time scale of weak interactions. Broadly, resolution requirements become more severe for weaker initial magnetic fields (and for nonpoloidal field topologies). Our systems are all as resolved, or better, than the model presented in Miller et al. (2019b). We briefly describe our quality factors in Appendix B.

In Figure 5.1, we show each of the disks colored by the value of β on the left and density on the right, as they appear 4 ms into each simulation, showing the more rapid time evolution exhibited by the stronger magnetic field.

Tracers

We uniformly sample (by volume; see Bovard and Rezzolla 2017) approximately 1.5×10^6 Lagrangian fluid packets (tracer particles) at the beginning of each simulation everywhere there is physical fluid, i.e., not artificial atmosphere. These tracers are passively advected with the fluid throughout the simulation and provide the thermodynamic evolution that is used to calculate the nucleosynthesis (see Section 5.3.2).

Of these tracers, we select those that have reached a radius of at least 250 gravitational radii (corresponding to approximately 10^3 km in this geometry) by the end of the simulation, and that furthermore have a Bernoulli parameter (Novikov and Thorne 1973):

$$Be = -u^0 \left(1 + \varepsilon + \frac{P}{\rho} + \frac{B^2}{\rho} \right) - 1 = -u^0 h - 1 > 0, \quad (5.2)$$

where h is the specific enthalpy, described by the energy density (ε), pressure (P), square of the magnetic field (B^2), and density (ρ). This ensures that the material we capture is unbound by the end of the nubhlight simulation. This selection process results in 195,288, 135,901, and 74,643 tracers for the b10, b30, and b100 disks, respectively. When referring to the time at which an individual tracer crosses this boundary, we use the notation t_{ex} . When referring to properties recorded at this same time, we use the same subscript, e.g. θ_{ex} .

At some point in the evolution of the disk, each of the tracers in our sample falls below a temperature of 10 GK for the last time, at which point we record their properties as a starting point for nucleosynthesis. We label this time t_{10} , and any associated tracer property recorded at this time with the same subscript. We emphasize that both the values of t_{ex} and t_{10} can be different for each individual tracer. We further emphasize that both t_{ex} and t_{10} refer to times after the start of the simulation.

5.3.2 Nucleosynthesis

We compute abundances for each of the nubhlight tracers out to 1 Gyr post-merger.

Thermodynamic Evolution

We use the portable routines for integrated nucleosynthesis modeling (Sprouse et al. 2021, PRISM) to perform nucleosynthesis calculations using the trajectories of the tracer particles that emerge from the selection of tracers described in the previous section. For each tracer, beginning at t_{10} , we extract the temperature and density as inputs for PRISM. Given that our nubhlight calculations are only run out to 127 ms, we extrapolate the tracers assuming homologous expansion past 127 ms out to at least 1000 s.

We further use $Y_{e,10}$ together with the SFHo EoS (Steiner et al. 2013) to determine the initial nuclear abundances.

Nuclear Model Set for Nucleosynthesis

PRISM is designed to take input files describing the decays and reactions to which nuclei involved in the r-process are subjected. We use the JINA Reaclib library (Cyburt et al. 2010) for charged particle and light nuclei interactions. We utilize the theoretical β decay rates from Möller et al. (2019) and compute both β -delayed neutron emission as well as β -delayed fission probabilities using Mumpower et al. (2016a).

Our neutron-capture and neutron-induced fission rates are calculated using the statistical Hauser-Feshbach code CoH (Kawano et al. 2016). We use the barrier-height-dependent prescription from

Karpov et al. (2012) and Zagrebaev et al. (2011) to calculate spontaneous fission rates using the FRLDM barrier-height description (Möller et al. 2015). Our theoretical alpha decay rates were computed using the Viola-Seaborg relation. Finally, where experimental or evaluated data exist, we overwrite theoretical values with data from the 2020 version of NuBase (Kondev et al. 2021) and the Atomic Mass Evaluation (Wang et al. 2021).

We note that the *r*-process relies on theoretical models that describe unknown nuclear physics far from stability. The choices we make here do not comprise the only possible ensemble of models. Rather, they correspond to a set of nuclear models often chosen as a baseline against which to compare nucleosynthesis calculations using different nuclear models. Several works have highlighted the potential for a wide variety of very large uncertainties in *r*-process modeling stemming from uncertain nuclear physics. These uncertainties can include the extent of the *r*-process pattern (whether third-peak or actinide material is produced), lanthanide mass fractions (predictions of which can span more than an order of magnitude), peak bolometric luminosities of resulting kilonova light curves (predictions of which can also span over an order of magnitude). Given the sensitivity of the *r*-process to the unknown physics of nuclei far from stability, many works have tackled this important question (see, e.g., Goriely et al. (2005); Arcones and Martínez-Pinedo (2011); Mumpower et al. (2012); Eichler et al. (2015); Vassh et al. (2019); Zhu et al. (2021); Barnes et al. (2021); Kullmann et al. (2023); Lund et al. (2023), and many others). In this work, we choose a single set of standard nuclear models in order to more closely investigate uncertainties stemming from the GR γ MHD simulations of the disk itself and to avoid degeneracies stemming from the use of different nuclear physics models.

Angle Dependence

We are interested in identifying and distinguishing material that is ejected at small angles above the equator (equatorial material) from material that is ejected at larger angles above the equator. In particular, the formation of a relativistic jet can eject material on very short timescales. In contrast, viscously driven material remains in the disk and evolves on slower timescales. Additionally, there may be a thermally or magnetic-torque-driven wind that can launch outflows on higher-latitude trajectories more rapidly than viscous driving (Blandford and Payne 1982; Fernández and Metzger 2013; Siegel and Metzger 2017; Fernández et al. 2018; Miller et al. 2019b; Fahlman and Fernández 2022; Kiuchi et al. 2023; Sprouse et al. 2024).

These differences in timescales can result in vastly different conditions for the material as it begins to undergo nucleosynthesis. Traditionally, the faster-evolving polar material tends to be associated with very poor lanthanide production and almost no actinide production. On the other hand, the equatorial, viscous material tends to be associated with a higher opacity, due to a more lanthanide-rich composition.

To probe these different regimes, we define criteria for classifying individual tracers as part of the equatorial viscous bulk, part of the polar bulk of material, or something in between. We classify a tracer as being polar if its spatial position at t_{ex} lies 45° or more *above* the midplane. Alternatively, we classify a

tracer as being equatorial if its spatial position at t_{ex} lies 15° or *less* above the midplane. All tracers that do not satisfy either of these criteria fall into the “intermediate” category.

5.4 Outflow Properties

We describe the properties of the material as it begins to undergo nucleosynthesis, as well as its properties as it becomes unbound from the system.

5.4.1 Mass Ejection

We record the properties of the Lagrangian tracers as they pass through a sphere of 250 gravitational radii (r_{ex} , corresponding to roughly 10^3 km in this geometry). By the end of the simulation, the total mass that we consider to be unbound is the mass that has passed through this surface. We found that the total mass ejected was largest for the b10 disk, and decreased as the relative field strength decreased, as can be seen by the end point of the curves in the top panel of Figure 5.2.

The total ejecta masses from each disk are listed in the topmost row of Table 5.1. By the end of the b100 simulation, the total mass ejected was roughly $2 \times 10^{-3} M_\odot$. Decreasing β to 30 increased the total ejected mass to $\sim 4 \times 10^{-3} M_\odot$; decreasing β to 10 further increased the ejected mass by almost a factor of 2, unbinding the largest mass of $7 \times 10^{-3} M_\odot$.

The bottom three panels of Figure 5.2 show the time evolution of the angular distribution of material as it passes through r_{ex} , with increasing β (and therefore decreasing field strength) from top to bottom. We include vertical lines showing the angular cuts described in Section 5.3.2 as a guide to the eye. Increasing the magnetic field strength results in a more quickly evolving system. This can also be seen in Figure 5.1, where the b10 disk is further along in its evolution by 4 ms compared to the b100 disk at the same time.

All three disks showed an early-time (by 20 ms) outflow at elevations above 20° . However, it was the b10 disk that showed a large burst of material escaping the system early on- the b100 disk only saw a trace amount of material escape in this time. Specifically, the b10 disk had ejected more than 4% of the total mass ejected by the time the simulation reached 20 ms. For comparison, the b30 disk at the same time had ejected roughly 2% of the total ejected mass, and the b100 disk only about 0.4%.

The disks with a higher magnetic field tended to evolve more quickly and therefore ejected a greater proportion of their mass more quickly. Just after the halfway point of the simulation, around 67 ms, the b10 disk has already ejected half its material, with b30 following closely at 70 ms and b100 at 87 ms. This trend toward earlier overall mass ejection as a function of increasing field strength represents at least two effects. The first is the relative mass ejected in this early (< 20 ms) transient, while the second is the behavior of hotspots of increased mass ejection, such as can be seen after about 80 ms in the b100 disk in Figure 5.2.

We note that these values represent lower limits to the total mass ejected from the system. The top panel of Figure 5.2 shows a cumulative mass ejection curve that has not reached a plateau by the end of

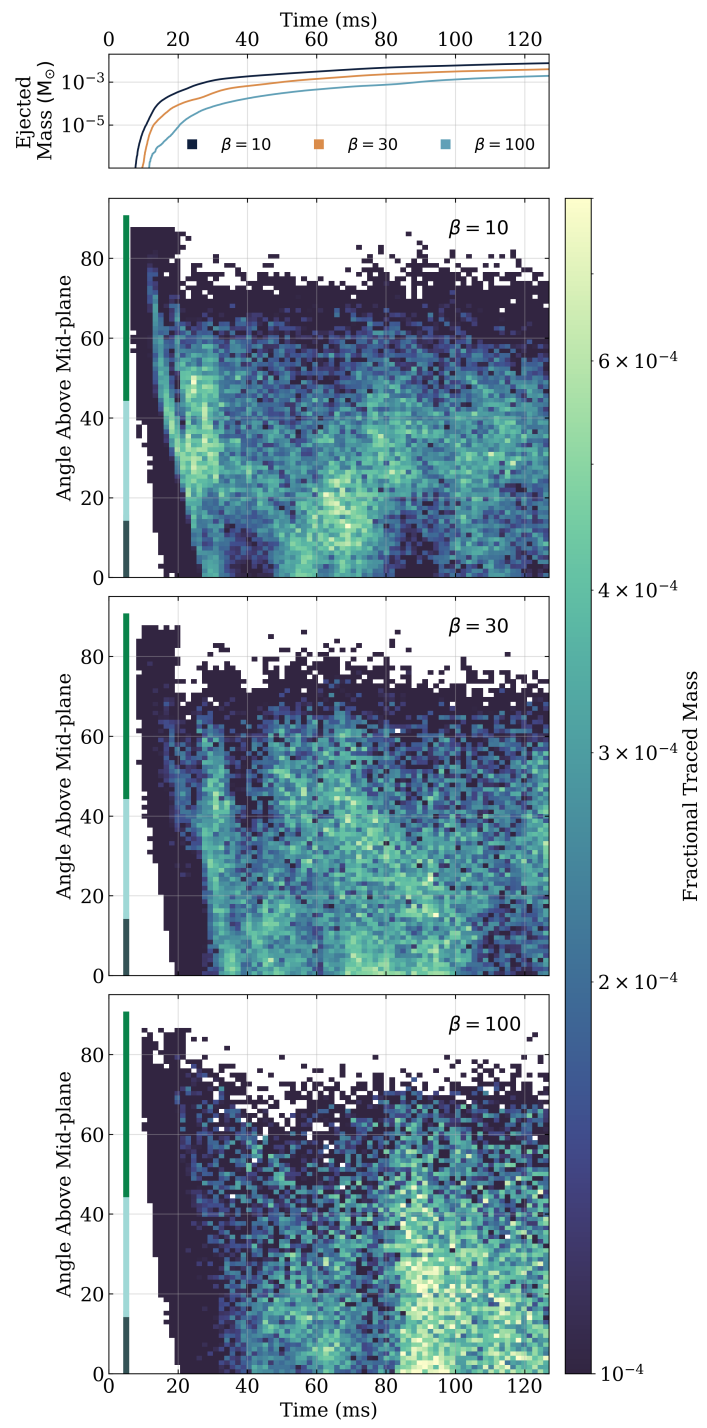


Figure 5.2: *Top panel:* Cumulative mass ejected for each disk as a function of time. *Bottom panels:* Relative (fractional) mass ejected through r_{ex} as a function of time and angle above the mid-plane for each disk outflow. In each case, the values of the histograms sum to one.

Table 5.1: *Top*: Global outflow properties for each disk. *Bottom*: Mass and composition properties for each angular cut within each disk.

| | b10 | b30 | b100 | | | | | | |
|-----------------------------------|-----------------------|-----------------------|-----------------------|------|-------|------|------|------|-------|
| Total Mass (M_{\odot}) | 7.31×10^{-3} | 3.83×10^{-3} | 1.89×10^{-3} | | | | | | |
| $M_{\text{Lan}} (M_{\odot})$ | 2.79×10^{-4} | 1.0×10^{-4} | 6.65×10^{-5} | | | | | | |
| $X_{\text{Lan}} (\times 10^{-2})$ | 3.82 | 2.62 | 3.52 | | | | | | |
| $M_{\text{Act}} (M_{\odot})$ | 5.03×10^{-5} | 7.84×10^{-6} | 2.07×10^{-6} | | | | | | |
| $X_{\text{Act}} (\times 10^{-3})$ | 6.88 | 2.05 | 1.1 | | | | | | |
| $M_{\text{Lan}}/M_{\text{Act}}$ | 5.5 | 12.8 | 32.2 | | | | | | |
| | Equatorial | Intermediate | Polar | | | | | | |
| | b10 | b30 | b100 | b10 | b30 | b100 | | | |
| Total Ejecta Mass (%) | 19.8 | 23.5 | 27.5 | 53.8 | 48.3 | 48.8 | 26.4 | 28.2 | 23.8 |
| Lanthanide Mass (%) | 50.8 | 64.8 | 48.8 | 41.7 | 23.8 | 48.8 | 7.46 | 11.4 | 2.4 |
| Actinide Mass (%) | 62.6 | 68.6 | 36.7 | 30.1 | 13.5 | 60.6 | 7.34 | 17.9 | 2.80 |
| $X_{\text{Lan}} (\times 10^{-2})$ | 9.79 | 7.24 | 6.26 | 2.96 | 1.29 | 3.53 | 1.08 | 1.06 | 0.353 |
| $X_{\text{Act}} (\times 10^{-3})$ | 21.7 | 5.98 | 1.46 | 3.84 | 0.573 | 1.36 | 1.91 | 1.30 | 0.129 |
| $M_{\text{Lan}}/M_{\text{Act}}$ | 4.5 | 12.1 | 42.9 | 7.7 | 22.5 | 26.0 | 5.6 | 8.2 | 27.3 |

the simulation, i.e. the ejected mass could be expected to continue to increase. We direct the reader to Sprouse et al. (2024) for a recent study on the b100 disk evolved an order of magnitude longer, which found a total ejected mass that was roughly 18 times, more than an order of magnitude, larger.

5.4.2 Nucleosynthetic Conditions

The values recorded at t_{10} set the conditions for nucleosynthesis. We show the electron fraction ($Y_{e,10}$) and entropy (s_{10}) recorded at t_{10} in Figure 5.3. The top row of the figure shows the absolute mass distribution, i.e. in units of M_{\odot} . The bottom row shows the fractional mass distribution, thereby showing the relative spread in values of Y_e and entropy.

Given that the electron fraction determines the number of free neutrons available for capture, it is the property most readily associated with producing a more robust *r*-process pattern. A key quantity of interest is the amount of material with $Y_{e,10} \lesssim 0.25$ given that this is a rough threshold below which a full *r*-process pattern is considered accessible, although the exact Y_e threshold varies according to the entropy and outflow timescale of the material. For all three disks, the tracers with $Y_{e,10} < 0.25$ accounted for more than half the total ejecta, with values of roughly 63%, 54%, and 66% for $\beta = 10, 30$, and 100, respectively.

Material that begins nucleosynthesis with a Y_e above 0.3 is very unlikely to produce a full *r*-process. Because it does not have the high opacity associated with actinides and lanthanides, this ejecta on its own is bluer and more quickly evolving than the lanthanide or actinide-rich outflows. Additionally, if material of this type is mixed in with ejecta that *does* produce lanthanides or actinides, it could serve to

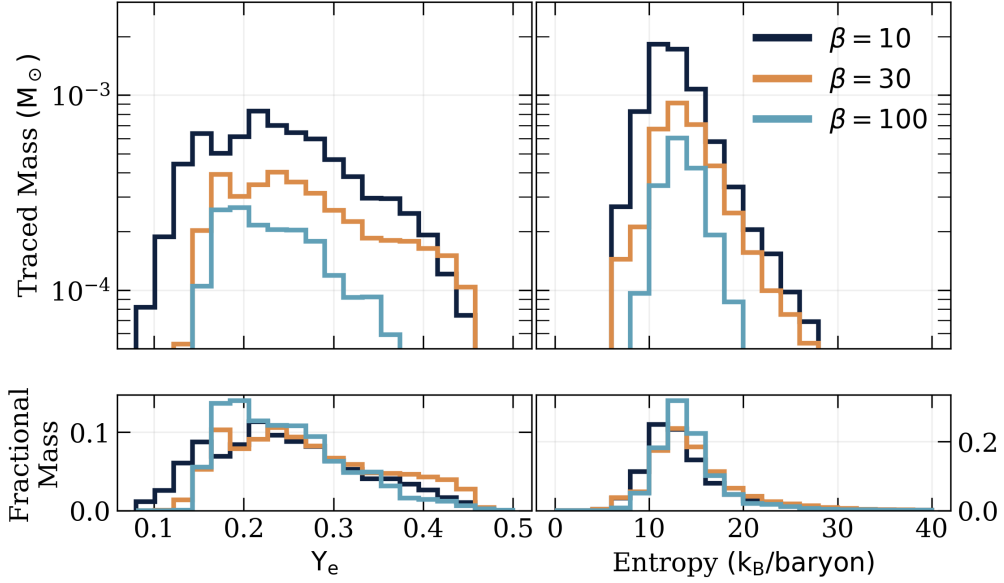


Figure 5.3: *Top row:* Distribution of electron fraction (left), and entropy (right) at t_{10} , showing total mass in each bin in units of M_\odot . *Bottom row:* The same as the top row but showing the fractional mass distribution.

dilute this outflow, leading to a bluer component. The fraction of higher Y_e outflow ranged from 31% for the highest magnetic field, b10 disk to 18% for the lowest magnetic field, b100 disk. As can be seen in the left column of Figure 5.3, the b10 disk produces the widest range of initial electron fractions, spanning the range from 0.1 to 0.45. This is consistent with it producing both the largest mass fraction of low Y_e material *and* a large mass fraction of high Y_e material.

Nucleosynthetic Conditions by Angle

More subtle differences in the conditions for nucleosynthesis emerge when we investigate these conditions as a function of angle. Figure 5.4 shows similar information as Figure 5.3, but in this figure our results are separated into the angular cuts described in Section 5.3.2.

For all three disks (shown in ascending order of β in the three rows of Figure 5.4), the lowest Y_e material is ejected from the equatorial ($r_{\text{ex}} \leq 15$) region, with the majority of the equatorial material falling into a range of $Y_{e,10}$ values at or below 0.25. However, the bulk of the material tends to sit at slightly higher Y_e with decreasing magnetic field, i.e. increasing β . At polar angles, the typical electron fraction is highest with the bulk of the material being between 0.3 and 0.4, and a tailing off of the distribution above $Y_e \sim 0.4$. Both the b10 and b30 polar ejecta show a sub-dominant peak on the low Y_e end of the distribution. The intermediate angle material, which tends to make up the majority of the outflow in each disk also has intermediate Y_e values. The Y_e distribution of the intermediate-angle material shows less of a dependence on β , although the b10 material shows a sub-dominant low- Y_e peak around 0.15.

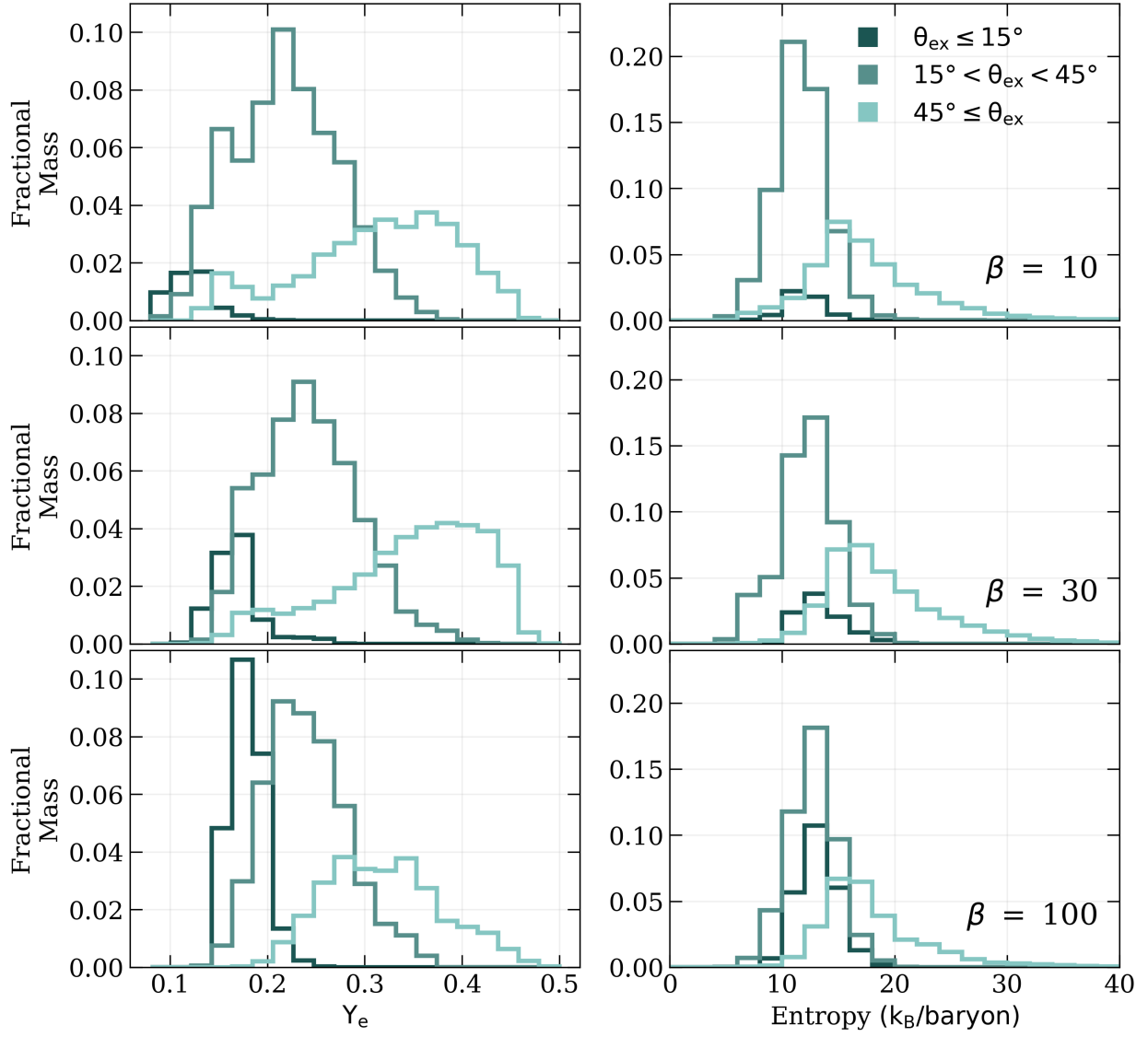


Figure 5.4: Fractional mass distributions of key properties divided into angular cuts for b10 (top row), b30 (middle row), and b100 (bottom row). The left column shows electron fraction while the right column shows entropy.

5.5 Nucleosynthesis Results

5.5.1 Global Results

We compare the overall nucleosynthetic outcomes for all tracers from the b10, b30, and b100 disks. We discuss both the overall results as well as the behavior of the cuts described in Section 5.3.2.

The top-most panel of Figure 5.5 shows the isotopic masses produced by the tracers from the b10 (dark blue), b30 (orange), and b100 (light blue) disks, while the second panel shows the overall, mass-weighted abundances produced by the tracers from each disk in the same colors. These scaled abundances are scaled to the abundance of $A=120$ in b10, and the scaled solar abundances (Arlandini et al. 1999; Goriely 1999) are shown as grey points. We find broad agreement in the overall shape of the abundance patterns, though with notable differences in the scale of the patterns and in particular regions.

By scaling the abundances produced in each disk, we are able to compare the relative abundances in different regions to $A=120$. As noted in the last section, the highest magnetic field disk (b10), has the largest fraction of low Y_e material. As expected, the outflow from this disk is most effective at producing lanthanide, third peak and actinide material relative to the second peak. One might similarly expect that the b10 disk is also most effective at producing the relative amounts of light r-process elements but in fact, it is the intermediate magnetic field disk that does this. This is consistent with Figure 5.3 where the b30 disk has the largest fractional ejected mass at high Y_e .

The top section of Table 5.1 lists the total mass unbound for each of the three simulations, as well as what mass fraction of that outflow was composed of lanthanides or actinides.

We find that there is not a significant impact on the *total* lanthanide mass fraction ejected from each of the three disks; all three exhibit X_{Lan} values close to 3×10^{-2} . The mass of lanthanides ejected from each disk was more heavily influenced by the disk's total ejecta mass, rather than the ability of each disk to actually produce lanthanides, i.e. the lanthanide mass fraction.

In contrast, the magnetic field strength has a strong impact on actinide production. As listed in Table 5.1, increasing the initial field strength by a factor of ten, i.e. from b10 to b100, results in more than a factor of six larger actinide mass fraction.

5.5.2 Angular Dependence

One of the most striking features of Figure 5.5 are the differing contributions to the overall *r*-process patterns from each angular part of the outflow from the three different disks. We plot the percentages of the total ejecta mass, total lanthanide mass, and total actinide mass originating from each angular cut in Figure 5.6. We also list these values in bottom half of Table 5.1 for convenience.

As can be seen by the solid medium blue line on the top left panel of Figure 5.6, the largest total mass component was the one ejected at intermediate angles for all three disks; in each case, it accounted for roughly half the ejecta by mass. The other half of the mass was roughly evenly split between the polar

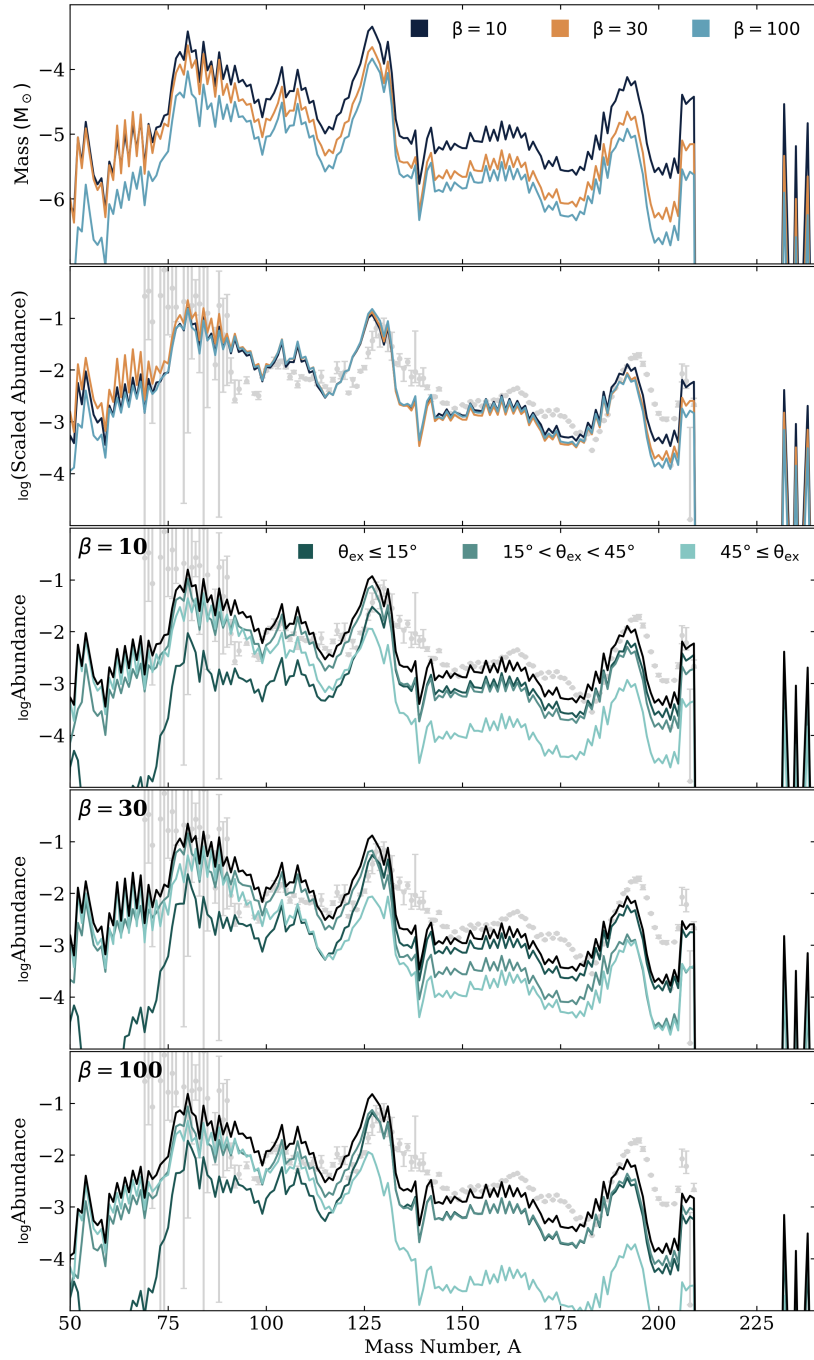


Figure 5.5: *Top panel:* Isotopic mass for all three disk outflows. *Second panel:* Abundances for all three disk outflows, compared to solar (grey points). All abundances are scaled to the value of $A=120$ from b10. *Bottom panels:* Total abundance for b10 (third panel), b30 (fourth panel), b100 (bottom panel) outflows as well as the contribution from the material in each angular cut.

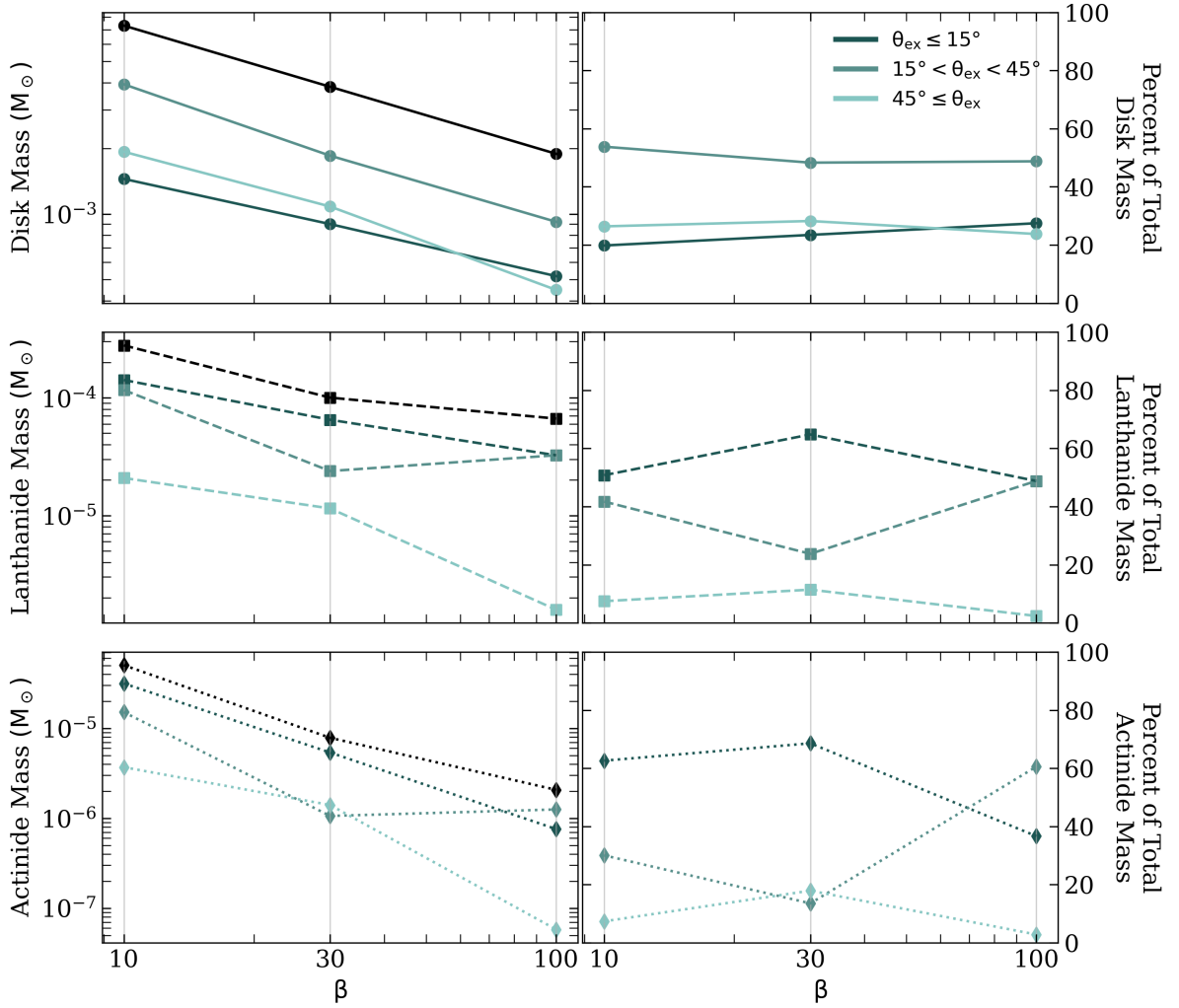


Figure 5.6: *Left:* Ejecta mass (top, solid), lanthanide mass (middle, dashed), and actinide mass (bottom, dotted) produced in each of the angular components. The total (top) disk mass, total lanthanide (middle) mass, and total actinide (bottom) masses are shown in black for each disk. *Right:* Percent values of the contribution to the total ejecta mass (top, solid), the total lanthanide mass (middle, dashed), and the total actinide mass (bottom, dotted) for the initial value of β characterizing each disk, for each angular component. In all panels, the light, medium, and dark blue lines show the contribution from the polar, intermediate, and equatorial outflow, respectively.

and equatorial ejecta, with the b10 and b30 disks showing slightly more polar outflow and the b100 disk showing slightly more equatorial outflow.

Lanthanide Outflows

Since lanthanides are a critical component of opacity as well as stellar abundance patterns, we now turn from *total* mass outflow to *lanthanide* mass outflow. The dashed dark blue line on the left central panel of Figure 5.6 indicates that the largest lanthanide mass emerges from equatorial angles, and this mass increases with increasing field strength. This figure also shows that the lanthanide mass ejected from polar angles contributes the least to the total lanthanide mass in all three disks, contributing less than or around 10% of the total lanthanide mass in the b10 and b100 disks.

The intermediate angle component produces a lanthanide mass that is intermediate to the polar and equatorial lanthanide ejecta in all disks, as can be seen by the medium blue dashed line in the left central panel of Figure 5.6. However it does not follow the same pattern of lanthanide mass increasing monotonically with increasing magnetic field strength. In both the b10 and b100 disks, the lanthanide ejection from intermediate angles is comparable to that from the equatorial region. However, in the b30 disk, the intermediate angle lanthanides are only 24% of the total lanthanide mass, compared to 40-50% in the other two disks. This can be seen by comparing the medium blue squares (dashed lines) in the right central panel of Figure 5.6. The decreased lanthanide ejecta from intermediate angles in the b30 disk causes the overall lanthanide mass fraction produced in the b30 disk to be the smallest of all three disks. While difficult to see on the log scale of the second panel of Figure 5.5, the total lanthanide mass fraction in the b30 disk is almost one and a half times smaller than the other two disks.

At first glance, it would appear that these patterns reveal a simple decrease in lanthanide production with increasing angle. Indeed, this is true: the total lanthanide mass fraction in the equatorial ejecta is largest, followed by the intermediate angle ejecta, and the smallest lanthanide mass fraction coming from the polar ejecta. However, this does not tell the whole story.

Figure 5.7 shows the relation of t_{ex} , θ_{ex} , lanthanide mass fraction, and average entropy in the form of a cube with shared axes. The teal color maps are two-dimensional mass histograms showing the fractional mass in each bin. The purple surface shows the same bins but colored by average entropy of the material in those bins. We included dotted red lines at values of $\theta_{ex} = 15^\circ$ and $\theta_{ex} = 45^\circ$ as a guide. Furthermore, we note that only tracers which resulted in $-1.6 < \log_{10}(X_{Lan}) < -0.5$ are included in this sample.

In all three disks, there is a transient-type component emerging early in time, at high angles. This initial transient is composed of on-average high entropy material, as shown by the dark values on the purple surface corresponding to an early time slice. The majority of the mass that emerges at high angles is ejected in this early ejection event, though the b10 disk shows subsequent mass ejection around $t_{ex}= 80$ ms. By examining the same high-angle slice on the sides showing $\log_{10}(X_{Lan})$, one can see that this material tends to result in fairly large lanthanide mass fraction, indicating that despite the overall higher Y_e of the polar ejecta shown in Figure 5.4 some of the higher entropy polar ejecta is very effective

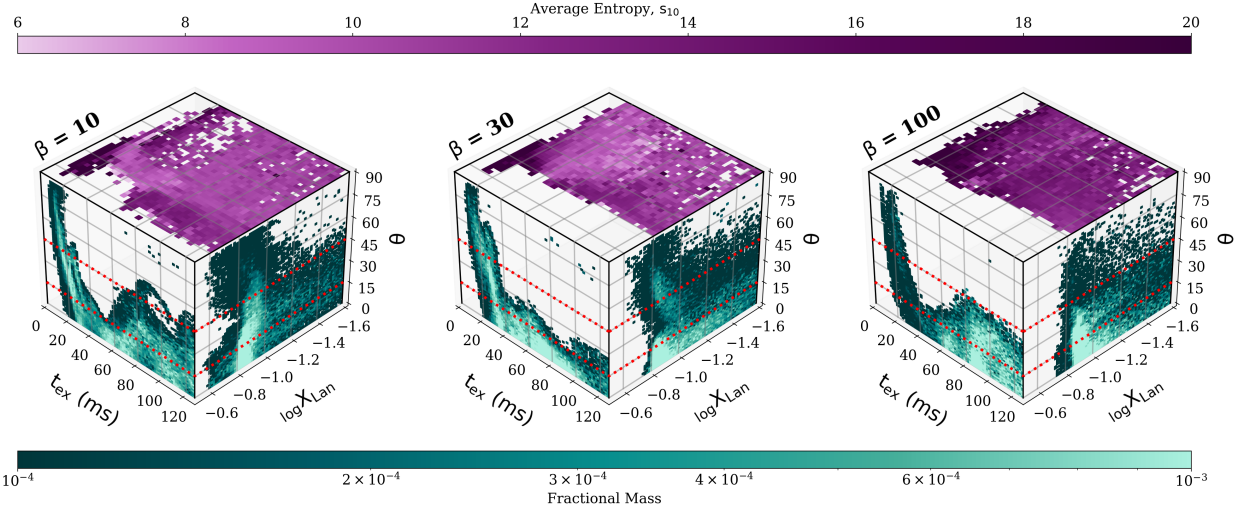


Figure 5.7: *Teal*: Two dimensional histograms showing the fractional mass binned by t_{ex} (x-axis, left) or $\log_{10}(X_{\text{Lan}})$ (y-axis, right) and angle above the mid-plane (vertical axis). The color map shows the fraction of the total mass, i.e. all values sum to one on each face. *Purple*: Mapping of the average entropy as a function of t_{ex} and X_{Lan} . The disks are shown with increasing β from left to right.

at producing lanthanides.

Additionally, all three disks show equatorial ejection consistent with that shown in Figure 5.2, indicating that the equatorially-ejected material fairly consistently produces lanthanides. This is further supported by the right faces of Figure 5.7, which show the majority of the mass concentrated between $\log_{10}(X_{\text{Lan}})$ values of -0.8 and -1.0 .

As noted earlier in this section, the most variable lanthanide ejection in each of the disks is that which occurs at intermediate angles, and as can be seen from Figure 5.7, these intermediate angles capture natural variability in mass outflow in the form of pulsations in the ejecta. Following the initial transient, the ejection angle of all three disks tends towards lower values. At some point following this, each disk shows another excess starting at around 50 ms. In the b10 disk, this second excess sees lanthanides getting ejected at angles as high as 60° . After this excess, the beginning of another appears around 110 ms and again sees trace amounts of lanthanides being ejected above 45° . The b100 lanthanide outflow also shows material being pushed up to high angles, though not as high as the b10 case.

The periodicity of these outflows roughly tracks the Keplerian orbital period of horizon-scale material in the disk, perhaps indicating a connection to low wave-number oscillation modes in the disk (Abramowicz et al. 2006), such as those caused by the magnetic dynamo (Heinemann and Papaloizou 2009).¹

Once again, the b30 behaves rather differently. Following the initial transient event, lanthanides are only ejected around or below 30° above the mid-plane. Furthermore, beyond around 100 ms, only

¹For a review of these phenomena, see Abramowicz and Fragile (2013).

fairly small amounts of lanthanides are ejected from any angle. This leads to the previously noted lower overall abundance of lanthanides coming from this disk.

We note that the variety seen in the maximum angle reached during the different lanthanide outflow pulsations reveals a dependence of our analysis on the choice of angle cuts we have made. For example, as can be seen in Figure 5.7, a relatively large lanthanide mass is ejected from the b30 disk with a maximum angle of $\sim 30^\circ$ around 60 ms. Our choice of setting the cutoff angles at 15° and 45° results in a larger relative lanthanide mass being contributed to the equatorial category rather than the intermediate category. We simply caution that some part of our interpretation is dependent on choices made during our analysis.

Actinide Outflows

While increased lanthanide mass ejected in disks with stronger magnetic fields is more a consequence of larger ejecta masses overall, this is not the case for the actinides: in addition to disks with stronger fields ejecting more actinide mass, one can see from Table 5.1 that increasing the magnetic field tenfold results in more than a factor of six larger actinide mass fraction. This is also apparent from the scaled total abundance patterns shown in the top panel of Figure 5.5, where the third peak and actinide abundances show some of the largest variability.

The largest contribution to the actinide outflow at higher magnetic field comes from the equatorial region as one might expect, but as can be seen in the left panel of Figure 5.6, the largest contribution to the total actinide mass in the lowest magnetic field disk comes not from the equatorial region but from the intermediate angle ejecta. However, in this b100 disk, the vast majority of the remaining actinide production does come from the equatorial outflow. In b30, the sub-dominant ejecta is divided reasonably similarly between the intermediate and polar ejecta, while in the b10 disk the polar actinide outflows play only a small role. These angular patterns indicate a much higher variability in actinide production depending on magnetic field strength as compared to lanthanide production.

5.6 Conclusion and Outlook

We performed three separate GR ν MHD simulations representing a NSM black-hole accretion disk. For each disk, we varied the parameter β as a proxy for varying initial magnetic field strength. We followed the evolution of each disk out to $10^4 \text{ GM}_{\text{BH}} \text{ c}^{-3}$, or roughly 127 ms. We extracted more than 400000 Lagrangian tracer particles from these simulations to compute nucleosynthetic yields.

Our results indicated that a stronger initial magnetic field resulted in larger total ejecta mass as well as total lanthanide and actinide masses. We found that increasing the initial magnetic field strength by a factor of ten resulted in the disk ejecting half its mass more than 10 ms earlier. Furthermore, doing so resulted in almost a factor of 4 larger total ejecta mass. In each case, roughly half the material was ejected between 15° and 45° .

We performed nucleosynthesis on each of the unbound tracer particles and found broad agreement: all three disks produced a full *r*-process pattern including actinides. In each case, the total lanthanide mass fraction was between $2-4 \times 10^{-2}$; the total lanthanide mass roughly scaled as the total ejecta mass. The smallest contribution to the lanthanides came from polar material ejected higher than 45° above the mid-plane. This polar lanthanide-rich material was mostly ejected during an early-time transient and consisted of on-average high entropy material. We find that the nature of the early-time transient is sensitive to the initial conditions of the disk: by changing the magnetic field strength, the outflow pattern and composition of this transient change correspondingly.

We found large variation in the actinide production as a function of magnetic field strength. In the stronger field cases of the b10 and b30 disks, more than half of the actinide content produced originated from equatorial ejecta. Meanwhile, the largest percentage of actinide mass in the b100 disk emerged from the intermediate angle ejecta. We found that decreasing β from 100 to 10 resulted in more than a factor of 6 larger total actinide mass fraction.

One particularly exciting connection is that to *r*-process-enhanced metal-poor stars. The low metallicity ($[Fe/H] < -2$) these stars exhibit is indicative of their very old age; exhibiting comparatively high *r*-process abundances ($[Eu/Fe] > +1$) makes these stars excellent targets for interpreting early galactic *r*-process enrichment. Given that these stars do not produce *r*-process elements in their own lives, any *r*-process material is understood to have originated in an *r*-process-producing event, such as a NSM. Spectroscopic observations of these types of stars are often used to demonstrate the robustness of the *r*-process pattern as most observations yield lanthanide patterns very similar to those measured in the Sun (within error bars). However, a broader range of actinide enhancement have been observed that do not agree with measurements of actinides in the Sun, thus creating a spectrum ranging from actinide-poor (Frebel et al. 2007) to actinide-boost (Holmbeck et al. 2018a). Our observation that changing the initial magnetic field strength in the three disks resulted in roughly similar lanthanide mass fractions but very different actinide mass fractions hints at a possible connection to this wide variability in actinide enhancements exhibited in stellar observations of *r*-process-enhanced, metal-poor stars. We point the reader to, for example, Holmbeck et al. (2018b, 2020b); Lund et al. (2023); Kullmann et al. (2023) for recent studies addressing this question².

Differences in the evolution of the isotopic composition of the ejecta (and therefore the nuclear heating) can imprint distinct signatures in kilonova light curve predictions caused by specific nuclei (Zhu et al. 2018; Vassh et al. 2019; Even et al. 2020; Zhu et al. 2021; Barnes et al. 2021; Lund et al. 2023; Kedia et al. 2023). We therefore expect that recording the nuclear heating profile based on the angle dependence of the ejecta we have found in this work would yield similar consequences for angle-dependent kilonova predictions. Due to the computational cost of running such a large number of nucleosynthesis calculations, we extracted the abundances at a (single) late time in order to investigate broadly what abundance patterns these systems could produce. A complete picture of the impact of magnetic fields on kilonova observables requires passing nucleosynthetic yields and outflow morphology

²See section 4.2 of Holmbeck et al. (2023b) for a review.

through a full radiative transfer calculation, where we expect as rich a phenomenology in the light curves and spectra as we have found in the nucleosynthesis.

CHAPTER
SIX

KILONOVA EMISSIONS FROM NEUTRON STAR MERGER REMNANTS:
IMPLICATIONS FOR NUCLEAR EQUATION OF STATE

KELSEY LUND

with

RAHUL SOMASUNDARAM, GAIL McLAUGHLIN, JONAH MILLER, MATTHEW MUMPOWER, INGO
TEWS

**The following chapter will be submitted as a Letter to The Astrophysical Journal. Some
figures have been modified from their original versions to fit dissertation format.**

6.1 Introduction

The nuclear equation of state (EoS) describes the properties of dense nuclear matter, such as its pressure as a function of density, temperature, and composition. Probing the nuclear EoS as a function of density and isospin asymmetry represents a significant challenge in nuclear physics given the difficulties associated with creating high densities and very asymmetric systems in terrestrial laboratory experiments (Danielewicz et al. 2002; Russotto et al. 2016). Neutron stars, however, explore matter up to several times nuclear saturation density at high neutron-to-proton asymmetry, and hence provide an excellent astrophysical laboratory for studying the nuclear EoS (Lattimer 2012). Explosive astrophysical events involving neutron stars are particularly important as they offer an additional avenue via which to probe extreme nuclear conditions Abbott et al. (2017c, 2018). A great amount of effort is being dedicated toward building statistical frameworks to be used in the inference of EoS properties from astronomical multi-messenger observations, including binary neutron star mergers Pang et al. (2023). These statistical models rely on piecing together different stages of the merger, making assumptions at each step.

In particular, the nuclear EoS affects the behavior of neutron stars during the in-spiral phase of a neutron star merger (NSM; Takami et al. 2014; Abbott et al. 2018; Most et al. 2019) and therefore also affects the properties of the post-merger system. This post-merger system can generally be characterized by an accretion torus surrounding a central remnant, either a hypermassive ($\gtrsim 2M_{\odot}$) neutron star or a black hole (Baumgarte et al. 1999; Kiuchi et al. 2012; Bauswein et al. 2013a; Lippuner et al. 2017; Metzger et al. 2018; Radice et al. 2018a; van Putten and Valle 2019; Ciolfi and Kalinani 2020; Beniamini and Lu 2021). The winds of material coming off this accretion disk are a promising site for the nucleosynthesis of the heaviest elements via the rapid neutron capture process (r-process), the decays of which power an electromagnetic transient. Thus recent decades have seen immense efforts towards understanding the relation between the formation of the disk, its evolution, and the amount of material (especially r-process-producing material) that becomes unbound from the disk (Ruffert et al. 1997; Popham et al. 1999; Shibata et al. 2007; Surman et al. 2008; Fernández and Metzger 2013; Fernández et al. 2014; Janiuk, Agnieszka 2014; Foucart et al. 2015; Just et al. 2015; Sekiguchi et al. 2015; Siegel and Metzger 2017; Fernández et al. 2018; Miller et al. 2019b; de Haas et al. 2023; Sprouse et al. 2024; Lund et al. 2024).

The nuclear EoS plays a role in determining the distribution of material during and after the merger, affecting such quantities as the remnant disk mass and ejecta masses as well as the behavior of the late-time electromagnetic signal (the *kilonova*; KN) that accompanies the merger event (Abbott et al. 2018; Coughlin et al. 2018; Malik et al. 2018; Radice et al. 2017, 2018b; Gamba et al. 2019; Krüger and Foucart 2020). In particular, the mass of the wind ejected off the disk is a key quantity involved in interpreting the KN signal attributed to the disk. While many early works have used the inspiral to constrain the EoS, increasingly more works use both electromagnetic plus gravitational wave signals to constrain the EoS (Bauswein et al. 2017; Dietrich and Ujevic 2017; Margalit and Metzger 2017; Radice et al. 2017; Pang et al. 2023).

In this work, we evaluate important physical considerations and potential degeneracies involved in

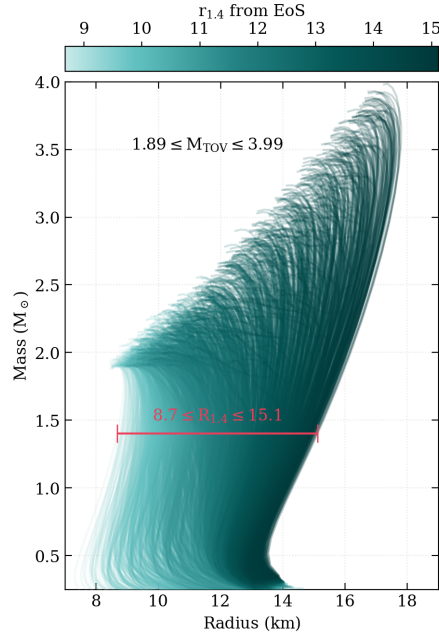


Figure 6.1: Mass radius curves for equations of state. The total sample of 2000 EoSs results in a range of $8.7 \leq R_{1.4} \leq 15.1$ and $1.89 \leq M_{\text{TOV}} \leq 3.99$.

several common steps in the inverse problem of using electromagnetic neutron star merger observables to infer the EoS. When considering the accretion disk's contribution to the KN light curve, it is common to use formulae derived from fits to simulation data to estimate a disk mass, which is then estimated to eject a certain amount of material in the form of a wind. This wind mass can then be used as input parameters for light curve calculations whose results serve to inform the interpretation of light curve features (Bulla 2019).

Here, we revisit this procedure and re-analyze disk masses from numerical relativity (NR) simulations of neutron star mergers published in the literature. From these, in Section 6.3, we introduce a novel fitting formula aimed at predicting the disk mass resulting from an NSM. In Section 6.4, we make connections between the predicted disk masses with the mass of the wind ejected from the disks informed by general relativistic magnetohydrodynamics (GRMHD) simulations. In Section 6.5, we connect the nuclear physics involved in the nucleosynthesis occurring in these winds to observable properties of the KN light curve. We use Section 6.6 to employ our disk mass formula to a set of chiral effective field theory (χ EFT) informed nuclear EoSs for binaries consistent with the inferred binary properties of GW170817 in order to constrain the nuclear EOS using observations of AT2017gfo. We conclude in Sections 6.7 and 6.8 with a discussion of our results and concluding thoughts.

6.2 Equations of State

We use the family of equations of state (EoS) presented in Capano et al. (2020). The details of the construction of this family of EoSs are included in the original publication; we include a summary of the methods used for convenience.

The construction of the EoS sample we use in this work begins with microscopic quantum Monte Carlo calculations for neutron-matter EoSs based on two nuclear Hamiltonians from χ EFT up to $2 \cdot n_{\text{sat}}$, and fit to nucleon-nucleon scattering data, the α -particle binding energy, and neutron-alpha scattering properties, as in Tews et al. (2018). The neutron-matter EoS results were then extended to β -equilibrium, and a crust was added in order to obtain neutron star EoSs. The high-mass neutron star regime was accessed by computing the speed of sound, c_s , up to either n_{sat} or $2 \cdot n_{\text{sat}}$ for the microscopic calculations, then performing a six-point extension of the speed of sound calculation up to $12 \cdot n_{\text{sat}}$, with the constraint that $0 < c_s < c$. This procedure is carried out for both Hamiltonians for $\sim 10,000$ EoSs, which are then further constrained by a lower bound on the maximum NS mass of $1.9M_\odot$. This initial data set is further reduced to 2000 EoSs selected such that the prior on the radius of a $1.4M_\odot$ NS ($R_{1.4}$) is roughly uniform.

In this work, we begin with the sample of 2000 EoSs in the form of the number density, pressure, and energy density spanning baryon number density $n_b \lesssim 2 \text{ fm}^{-3}$ for each EoS. We solve the Tolman-Oppenheimer-Volkoff (TOV) equations (Oppenheimer and Volkoff 1939) to obtain solutions for the neutron star mass-radius relation for each EoS. Across the resulting EoSs, whose mass-radius curves are shown in Figure 6.1, the maximum TOV mass is $3.99 M_\odot$, and the radius of a $1.4M_\odot$ neutron star lies between 8.67 and 15.12 km.

6.3 Post-Merger Disk Mass

The EoS describes the properties of dense matter, which is a crucial input for understanding the behavior of neutron stars when subjected to external forces. Hence, it is a key input in NR simulations of neutron star mergers, as the EoS of the material that makes up the neutron star plays a large part in determining the dynamics of the merger system as well as the properties of the post-merger system. These post-merger system properties are a starting point for GRMHD simulations, which serve to model the evolution of the post-merger system.

In this section, we evaluate existing data from NR efforts, including those in Radice et al. (2018b) and Kiuchi et al. (2019), and those compiled by Camilletti et al. (2024). The compilation from Camilletti et al. (2024) includes data from Nedora et al. (2019), Perego et al. (2019), Bernuzzi et al. (2020), Endrizzi et al. (2020), Nedora et al. (2021), Cusinato et al. (2022), Perego et al. (2022), and Camilletti et al. (2022). This results in a total of 112 NR simulation data points from 11 sources¹. We discuss some of the proposed methods for using these data to analytically compute a remnant disk mass in Appendix C. Given that the combined data set we use is larger than the sets used to derive past fits, we take the opportunity to

¹These data points are listed and shown graphically in Appendix D

re-evaluate these suggestions. We find that the dependence on the compactness of the lightest neutron star, C_{light} , continues to yield a reasonably good fit, albeit with a slightly different functional form than Equation C.12. We are able to obtain a good degree of accuracy using the following:

$$\log_{10}(m_{\text{disk}}) = \alpha \tanh(\beta C_{\text{light}} + \gamma) + \delta, \quad (6.1)$$

with best-fit parameters $\alpha = -1.27$, $\beta = 69.02$, $\gamma = -11.90$, and $\delta = -1.98$.

We show the disk mass predictions from our result in the top panel of Figure 6.2. The top panel also shows results obtained from the analytical forms from Radice et al. (2018b, Rad18), Krüger and Foucart (2020, KF20), and Dietrich et al. (2020, D+20). The bottom panel shows, as a function of C_{light} , the ratio of the different disk mass predictions to the NR results. Overall, we find that our formulation provides a slightly better fit, with an overall RMS error of 0.041, compared to 0.067, 0.057, and 0.048 from Rad18, D+20, and KF20, respectively. We also note that our fit has a rather simple form without the need for an artificial termination point or cutoff.

6.4 Disk to Wind Mass

The ejecta from the neutron star merger system may be classified into two different categories. The first is the dynamical ejecta caused primarily by tidal and shock interactions during the merger phase. The second is the secular ejecta most commonly associated with neutrino-driven winds and viscous processes within the remnant accretion disk.

Within each of these components, a wide variety of nucleosynthetic conditions and yields are possible. This, of course, leads to an uncertainty in the contribution of each to the red component of the KN. While some models predict large ($\mathcal{O}(10^{-2} M_{\odot})$) dynamical ejecta masses, others predict negligible masses (see, for example, Table 1 of Dietrich and Ujevic (2017)). Proposed fit formulae intended to predict this mass result in uncertainties that are of order the ejecta mass itself.

The role of outflow from the remnant accretion disk is comparatively less studied, with detailed three-dimensional GRMHD simulations being applied to the merger scenario relatively recently. Recent works have shown that not only can a rather large mass be ejected from these accretion disks, but enough r-process material can be synthesized to account for the entire red component of the KN (Siegel and Metzger 2017). Motivated in part by these results, we focus solely on the *disk* ejecta, and further make the simplifying assumption that the disk ejecta alone is responsible for the entire red component of a kilonova, thus exploring a limiting scenario of the effect of the total merger ejecta on the kilonova. Proceeding under our limiting-case assumptions, once equipped with a disk mass, our next question becomes that of the amount of material that is ejected from the disk in the form of a wind.

GRMHD simulations provide the most detailed evolution of material in the post-merger accretion disk system by combining the effects of magnetically-driven turbulence, radiation transport, and neutrino interactions. In Table 6.1, we list the results of a sample of ejecta masses from recent GRMHD

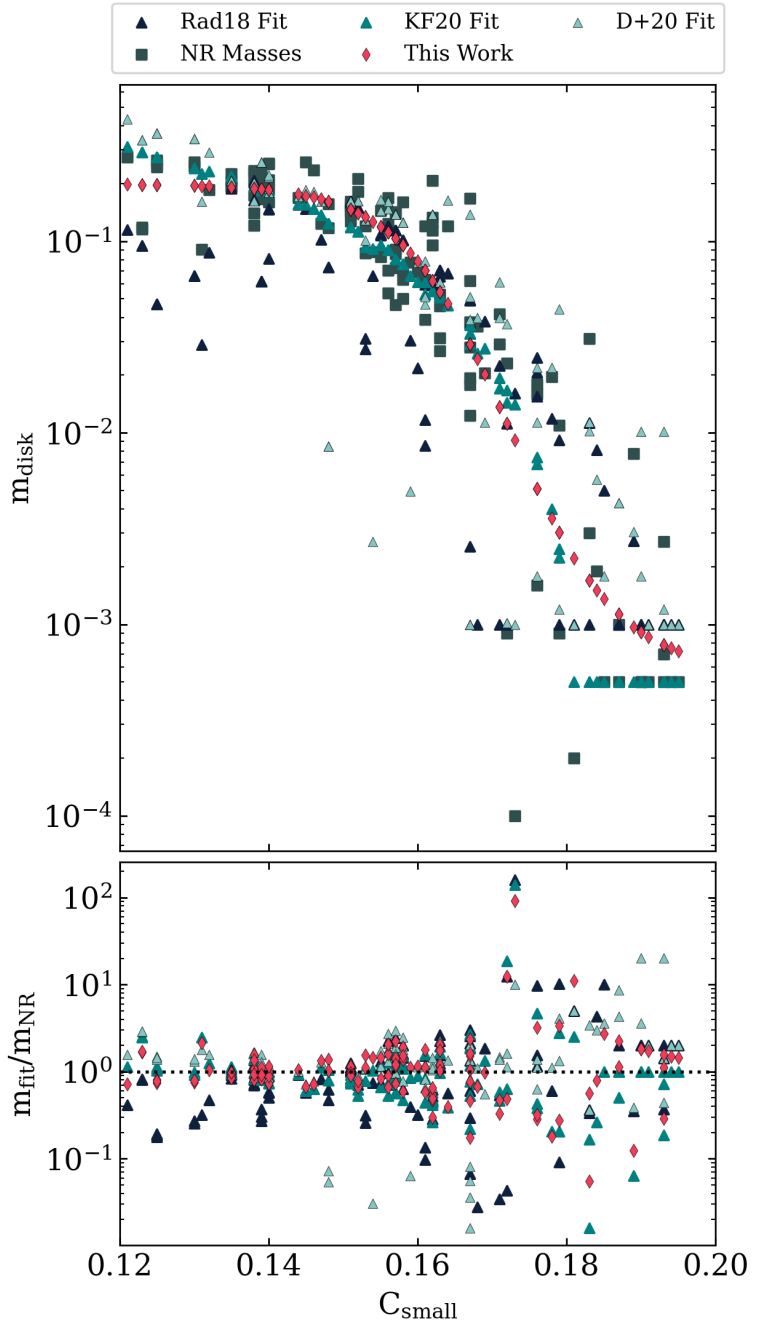


Figure 6.2: *Top:* Compilation of disk masses, as a function of the smallest NS compactness, C_1 for the 112 NR simulation points described in the text (dark squares). We show as triangles the results from the fitting formulae presented in Rad18 (dark blue, Radice et al. 2018b), KF20 (teal, Krüger and Foucart 2020), and D+20 (light blue Dietrich et al. 2020). The results from the fit proposed in Equation 6.1 are shown as pink diamonds. *Bottom:* Ratio between the masses obtained from the fit formulae to the NR data points.

Table 6.1: Wind masses from GRMHD simulations of NS-NS or NS-BH mergers, shown in solar masses as well as a percentage of the initial disk mass. In the first column, the remnant black hole masses are included in parentheses.

| Disk (BH) Mass (M_{\odot}) | Wind Mass $10^{-3} M_{\odot}$ | Wind Mass (% Disk Mass) | Reference(s) |
|-----------------------------------|----------------------------------|----------------------------|---|
| 0.42 (5) | 1.3 | 3.1 | Curtis et al. (2023) |
| 0.25 (7) | 3.9 | 1.56 | Curtis et al. (2023) |
| 0.143 (6) | 3.2 | 2.2 | Curtis et al. (2023) |
| 0.12 (2.58) | 1.89-33.3 | 1.6-28 | Miller et al. (2019b); Sprouse et al. (2024) |
| 0.12 (2.58) | 1.89-7.31 | 1.6-6 | Lund et al. (2024) |
| 0.082 (10) | 2.3 | 2.8 | Curtis et al. (2023) |
| 0.033 (3) | 8.9-13 | 27-40 | Fernández et al. (2018); Christie et al. (2019) |
| 0.020 (3) | > 3.2 | > 16 | Siegel and Metzger (2017) |

post-merger disk simulations. We discuss some of the differences across these different works and the implications for the interpretation of their results.

The results from Curtis et al. (2023) and Lund et al. (2024) specifically highlight that the amount of material ejected from the disk is dependent on physical properties of the post-merger disk (torus) itself. The disks evolved in Curtis et al. (2023) were meant to model BH-NS mergers. However, the simulations themselves began with a central black hole and do not directly include any of the physics involved in the merger itself, rather they are informed by the physics involved in the merger. Therefore, while the initial conditions of the disk are unlikely to emerge from binary neutron star mergers, they still provide insight into mass ejection from black-hole accretion disk systems. The results from these simulations highlight that a variety of parameters could affect the wind mass ejected from the disk, including black hole mass and spin. In all cases, although the parameters of the simulation changed, the percentage of mass ejected from each of the disks was between 1.5 – 3%, with no obvious correlation between the percentage of mass ejected and either disk or remnant (black hole) mass.

It should be noted that the description of the magnetic field in the post-merger disk are unclear. Both Christie et al. (2019) and Lund et al. (2024) investigate this uncertainty, with the former investigating magnetic field configuration and the latter magnetic field strength. A stronger initial magnetic field was found to facilitate more mass ejection over the same period of time than a disk with the same initial mass but weaker magnetic field.

Sprouse et al. (2024) highlights the uncertainty in total ejected mass that comes from finite simulation time, and represents an upper limit to the smallest ejecta mass data point from Lund et al. (2024). Indeed, due to the computational costs of the detailed physics utilized in these simulations, all the other values listed in Table 6.1 represent a significantly conservative *lower* limit². Unfortunately, the long simulation time that allowed this insight into the mass ejection of the disk simulation of Sprouse et al. (2024) has

²We refer the reader to Figure 12 of Sprouse et al. (2024) and its accompanying explanation for why these values should be taken as lower limits

not yet been applied to the other two disks in Lund et al. (2024), or to the BH-NS merger disks from Curtis et al. (2023)³. Therefore it is currently impossible to know for certain how much of the disks would eventually become unbound, i.e. whether the larger percentage of unbound mass due to the stronger initial magnetic field can be extrapolated to later times, or whether the larger magnetic field simplyunbinds more mass earlier with little to no effect on the total unbound mass. Therefore, we consider the 28% of the ejected disk mass to be a reasonable upper end of a *lower bound* for the total wind mass from this set of simulations.

One hint into the late-time behavior and upper limit of the percentage of mass ejected from the disk can be found in the long-time simulation of Fernández et al. (2018) and Christie et al. (2019). They find that the mass outflow peaks around one second, after which the outflow sharply declines. By the end of the simulation, roughly 9.3 seconds post-merger, the mass ejection has virtually ended⁴. Thus, by this time, 39% of the disk matter has been ejected, and running the simulation even longer would provide minimal returns on mass outflow.

Based on these works, we proceed assuming the following range of disk wind masses as a working estimate. On one end, early GRMHD simulations contribute a data point for a single disk mass, showing an *upper* limit of roughly 40% of the disk being ejected. On the other end, we take the *lower* limit to be 30% based on GRMHD simulations with more sophisticated neutrino physics and a larger variety of disk parameters.

6.5 Kilonovae from Disk Winds

The combined electromagnetic and gravitational wave observations from GW170817 remain the most closely investigated and scrutinized multi-messenger event in recent years. Thus we next turn to the wealth of observation and analysis from this event for two key observables: the peak luminosity of the light curve, and the time at which this peak occurs. We are specifically interested in obtaining the peak luminosity from the disk as an energy source. To do this, we continue with the simplifying assumption that the total bolometric luminosity can be taken as being composed of two components, one of which is the “red” component attributed predominantly to the wind material from the disk and describes the behavior of the light curve after ~ 4 days. Our goal in this section is to make the connection between properties of the light curve and the wind (ejecta) mass.

For this, we draw upon the work carried out in Zhu et al. (2021), which explored the wide variety of nuclear physics uncertainties and their effect on kilonova light curve modeling. Two specific models were created using different theoretical nuclear mass models in each case, and a linear combination of single- Y_e trajectories⁵ to obtain a final abundance that resembled the solar pattern. We include key

³These are grouped together in this discussion as they were all evolved using the same numerical methods.

⁴Following the criterion that $d\ln M_{ej}/d\ln t \simeq 0.03$. We refer the reader to section 3.3 of Fernández et al. (2018) for the full discussion.

⁵“Trajectories” refers to the time evolution of the temperature and density, which is a key ingredient for nucleosynthesis calculations.

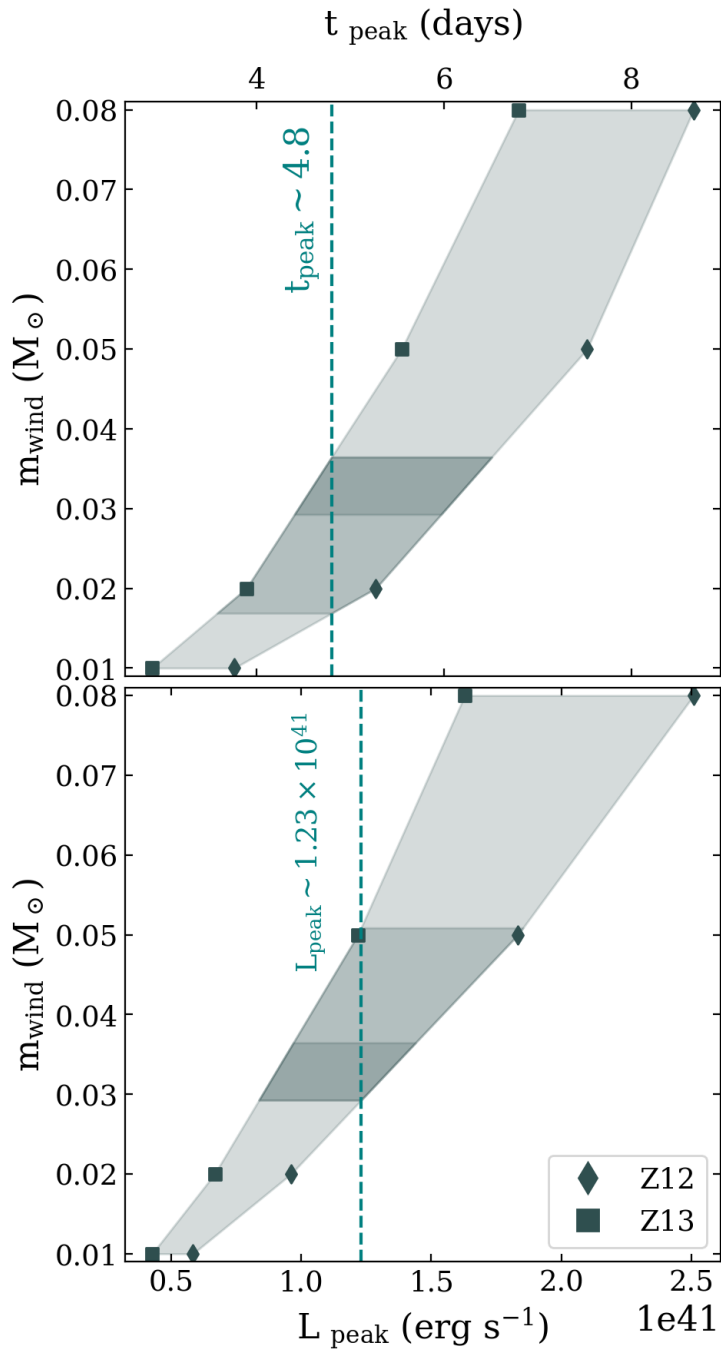


Figure 6.3: Inferred peak luminosity and times from the late-time, red component assuming a two-component model to explain the GW170817 electromagnetic signal (dashed vertical lines). Shaded regions highlight variation of these quantities with respect to ejecta mass from the Z12 and Z13 models of Zhu et al. (2021). The second darkest shaded region shows the region through which the peak time (top) and luminosity (bottom) overlaps, while the darkest shaded region shows the values through which both of the inferred observed quantities overlap.

parameters of these two models, which we refer to as Z12 and Z13, in Table 6.2 for convenience.

The purpose of selecting these two models is to gauge the uncertainty one might obtain from solely changing the ejecta mass, under the assumption that an event like GW170817 produced an abundance pattern resembling the solar one. It is important to highlight that the trajectories in these models, though producing very similar patterns, undergo different nuclear heating histories, which result in different light curve evolution. In Zhu et al. (2021), light curves were computed based on the nuclear heating and using ejecta masses of 0.01, 0.02, 0.05, and 0.08 M_{\odot} , with the results shown in Figure 12(a) of the original work. For each model, and for each of the masses previously listed, we show the times at which the peak bolometric luminosities occurred and the peak bolometric luminosities themselves as connected points in the top and bottom panels, respectively, of Figure 6.3. From the connecting of the sets of points from these two models, we are able to gauge a level of uncertainty in the properties of the kilonova from the nuclear physics uncertainties listed in Table 6.2.

We highlight two observations from this work. The first is that a single ejecta mass can result in differences of 1-2 days in the peak luminosity times due to uncertainties from nuclear physics effects. Similarly, the peak luminosity for a given ejecta mass is also subject to these same uncertainties stemming from unknown nuclear physics off-stability. The second observation is a consequence of the first: for a single peak luminosity and time inferred from an observation, a range of ejecta masses can be inferred.

We show this by selecting a luminosity of $1.23 \times 10^{41} \text{ erg s}^{-1}$ occurring at roughly 4.8 days post-merger. We select these quantities based on the two-component model shown in Waxman et al. (2018) (Figure 13 in the original work), itself based on the models of Kasen et al. (2017) and with the combined data from GW170817 (Cowperthwaite et al. 2017; Drout et al. 2017; Villar et al. 2017). We plot vertical lines where these quantities lie in Figure 6.3. By combining these quantities and the uncertainties in each from Zhu et al. (2021), we estimate that such a peak luminosity and time resulted in the ejecta from disk winds with mass $(1.688 - 3.645) \times 10^{-2} M_{\odot}$. Returning to our assumption that this wind mass corresponds to 30-40% of the original disk mass, this implies a disk mass range of $(4.22 - 12.2) \times 10^{-2} M_{\odot}$. We note that the use of these two models likely underestimates the true uncertainty from nuclear physics as these models were constructed in such a way that the resulting abundance roughly matched the solar pattern. However, the observations of GW170817 only indicate the production of lanthanides, with no direct proof that a solar pattern was produced. We emphasize that the use of these two models is to highlight the different possible nuclear histories resulting in similar abundance patterns, not the abundance patterns themselves.

6.6 Kilonova Constraints on Nuclear EoS

The final step in this puzzle is to use our inferred ejecta and kilonova properties to interpret implications for the nuclear EoS. Thus, we return to our sample of EoSs, described in Section 6.2, and combine them with the properties inferred from observation. For this, we select four possible binaries consistent with the literature values for the masses involved in GW170817 by selecting a smaller neutron star mass

Table 6.2: Key parameters of models 12 (here Z12) and 13 (here Z13) from Zhu et al. (2021) used in this work. These include the theoretical nuclear mass model fission rates and daughter production distributions used. Given that these models were constructed from combinations of single- Y_e trajectories, we also include the average electron fraction for each case.

| Model Name | Mass Model | Fission Rates | Fission Yields | \bar{Y}_e |
|------------|------------|---|----------------|-------------|
| Z12 | DZ33 | Karpov et al. (2012); Zagrebaev et al. (2011) | K&T | 0.138 |
| Z13 | UNEDF1 | Karpov et al. (2012); Zagrebaev et al. (2011) | 50/50 | 0.216 |

between $1.16M_\odot$ and $1.36M_\odot$. We note that we could use the tight constraint of the chirp mass:

$$\mathcal{M} = \frac{(m_{\text{light}} \cdot m_{\text{heavy}})^{3/5}}{(m_{\text{light}} + m_{\text{heavy}})^{1/5}} = 1.186_{-0.001}^{+0.001} M_\odot \quad (6.2)$$

to obtain the mass of the larger companion. However, our proposed formulation in Equation 6.1 depends solely on the properties of the lighter neutron star.

For each binary, which we characterize by the lighter neutron star's mass, we compute the possible disk masses using Equation 6.1 for the 2000 EoSs we describe in Section 6.2. We show the compactness values (and therefore the EoSs) that result in $4.22 \times 10^{-2} M_\odot \leq m_{\text{disk}} \leq 12.2 \times 10^{-2} M_\odot$ in Figure 6.4.

One important result is that smaller values of m_{light} result in smaller compactness values, therefore favoring softer⁶ EoSs. This can be seen in the right column of Figure 6.4, which shows the mass-radius curves of the allowed EoSs in the left column panels. Although we did not use the mass of the larger neutron star in our analysis, the aforementioned tightly constrained chirp mass for GW170817 implies that a neutron star with smaller m_{light} will have a larger companion if it is to result in the same chirp mass. Thus it can be interpreted that a softer EoS is also favored for a more asymmetric binary.

Across all four sample binaries, one of the major outcomes of our analysis is a constraint on the $1.4M_\odot$ radius that characterizes the EoSs with which we work. Overall, the allowed EoSs (colored in shades of blue in Figure 6.4) predicted values of $10.19 \leq R_{1.4} \leq 13$ km and $M_{\text{TOV}} \leq 3.06M_\odot$.

6.7 Summary and Discussion

In this work, we take a closer look at the complex interplay between the nuclear EoS, post-merger accretion disks, and kilonova observations. We discuss some of the limitations and implications of what we consider to be different sources of uncertainty, as well as the results we obtain from the process.

We re-evaluated a number of existing fits from the literature that serve to predict a disk mass from a neutron star binary using the same data set composed of the results of numerical relativity simulations, from 11 different sources, for a total of 112 data points. Our results indicate that the compactness of the lighter binary component still remains the best parameter for fitting, which we quantify with the

⁶Here, "soft" refers to a particular EoS predicting a smaller radius for a given mass.

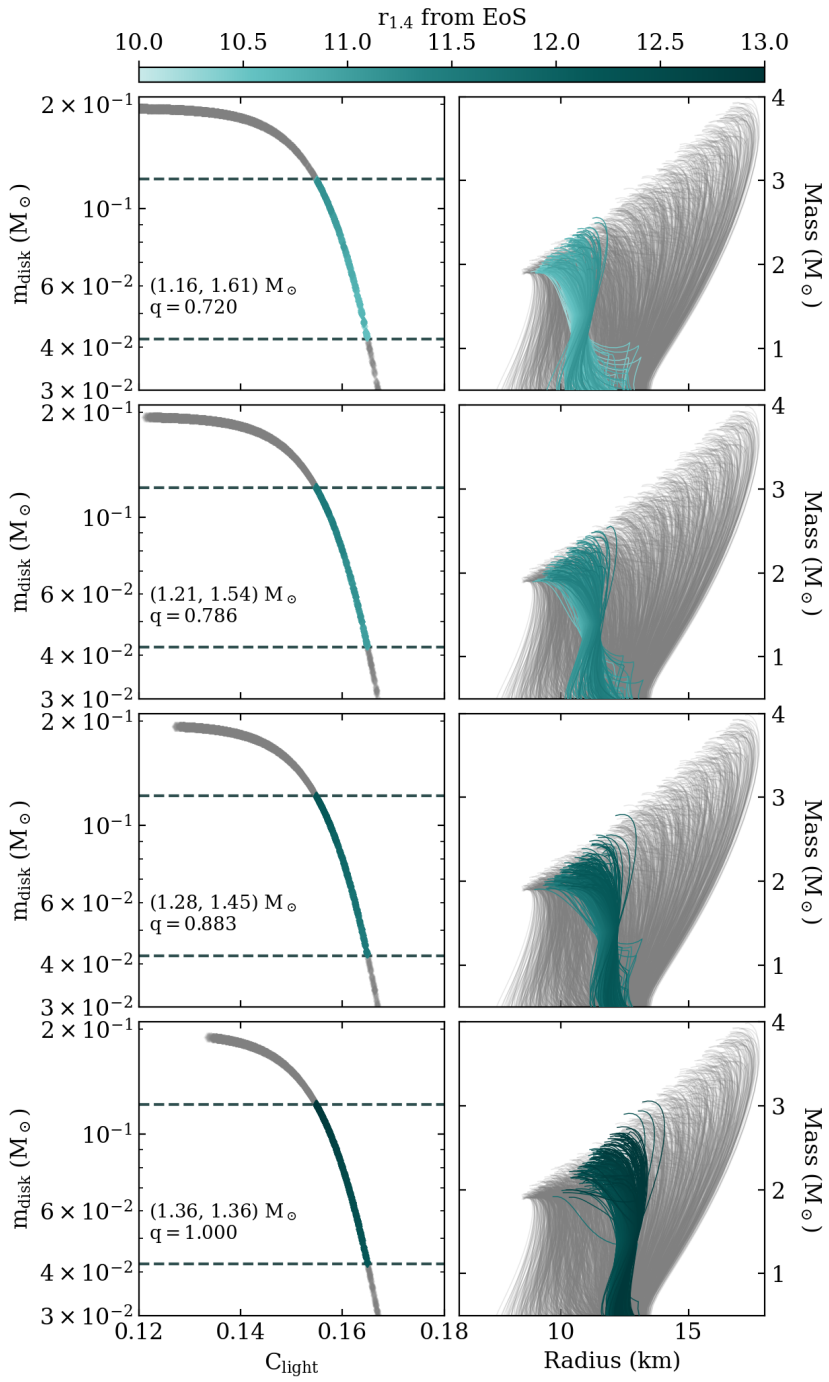


Figure 6.4: *Left:* Disk masses as a function of lightest neutron star compactness, C_{light} , for four binaries. *Right:* Mass-radius curves for allowed EoSs. *Both columns:* For each binary, EoSs that result in disk masses between the inferred values of $0.042 - 0.122 M_{\odot}$ (indicated with dashed lines in the left column) are shown colored according to the $1.4 M_{\odot}$ radius ($R_{1.4}$), as shown in the color bar. EoSs that do *not* result in masses within the aforementioned range are shown in grey for ease of comparison with Figure 6.1.

RMS error. We propose a different functional form than that of Krüger and Foucart (2020), as we find that the form of Equation 6.1 performs slightly better. As with existing fit formulae, ours is limited by the availability of simulation data, which exists for more symmetric binaries. The average mass ratio of our data sample was 0.91 with 58 of 112 simulations being equal-mass binaries. We expect that the inclusion of more data points, especially those from more asymmetric binaries, will result in better fits in the future.

Having suggested a way to predict a remnant disk mass, we turned to the question of the wind mass from that disk, under the assumption that it was this wind that was entirely responsible for the red component of a two-component light curve. For this, we turned to GRMHD simulations, which offer the most detailed insight into the disk evolution, as opposed to estimates from numerical relativity or hydrodynamical simulations. GRMHD simulations tend to predict higher wind masses due to the inclusion of magnetic field effects. However, there are a number of effects in play in these types of simulations.

In this work, we only included the mass percentage of the disk that became unbound by the end of each simulation, arriving at the conclusion that it was safe to assume that number to be 30-40%. In reality, it is likely that the evolution of the disk will contribute a degeneracy to the light curve evolution beyond simply an ejecta mass. For example, one of the main results of Lund et al. (2024) was to highlight the role of magnetic field strength on the time scale with which material was ejected, which we allude to in this text. This manifested also in the time scales of lanthanide ejection, which is expected to have a profound impact on the behavior of the light curve. Furthermore, the late-time results of Sprouse et al. (2024) compared to the same disk evolved a fraction of the time (Miller et al. 2019b; Lund et al. 2024) showed that the majority of the low- Y_e , lanthanide-rich material ejected close to the equator did so late in the simulation. It is thus entirely possible that the ~ 100 ms simulations of Miller et al. (2019b), Curtis et al. (2023), and Lund et al. (2024) underestimate the total lanthanide mass produced.

The use of the selected models from Zhu et al. (2021) are meant to emphasize that a single ejecta mass can be inferred from a variety of light curve behaviors which themselves are influenced by the unknown properties of nuclei far from stability. Thus, if one is attributing the late-time ($\gtrsim 1$ day) behavior of the kilonova to a disk wind, the interpretation of that late-time behavior depends to some extent on some combined assumption of both the nuclear heating history, the composition of the ejecta, and the ejecta mass itself. As demonstrated by even these two models, these effects can push the peak of the red light curve up (or down) in magnitude as well as shift the time of this peak towards earlier or later times.

Finally, we connected inferred values obtained from the multi-messenger analysis and work backwards through the steps we have laid out to make constraints on the nuclear EoS, resulting in a prediction of $10.19 \leq R_{1.4} \leq 13$ km and $M_{\text{TOV}} \leq 3.06 M_\odot$. It is apparent that the values we obtain result in error bars that are larger, but not entirely inconsistent, with other literature values.

We consider, for example, the results of Bauswein et al. (2017), who make predictions regarding the $1.6 M_\odot$ radius guided by fairly conservative assumptions about the properties of GW170817. Their analysis was driven mostly by the constraint provided by the EoS-dependent threshold mass, M_{thres} - the

same threshold mass used in the fits of Coughlin et al. (2018) and Dietrich et al. (2020). It was concluded that the minimum radius of a $1.6M_{\odot}$ neutron star must be $10.68^{+0.15}_{-0.04}$ km. Had we operated only under the assumption of an equal-mass binary, with each mass being $1.36M_{\odot}$ (which is the case for the bottom row of Figure 6.4), the allowed EoSs from our sample result in a similar prediction of $10.94 \leq r_{1.6}$.

Our analysis leads to results based on simple statistics informed by a single event. It is therefore not surprising that the width of our EoS error bars be larger than, for example, the results published in Koehn et al. (2024), which are based on Bayesian statistics of a wide variety of astronomical constraints. However, even their analysis of the combined gravitational wave + kilonova + gamma-ray burst data leads to an estimate of $R_{1.4} = 12.19^{+0.71}_{-0.63}$ km, which is in good agreement with the range of radii we obtain. It should be emphasized that the results of Koehn et al. (2024) are given in terms of 90% confidence levels; ours are meant to simply illustrate possible values given a detailed look at specific aspects of the analysis.

6.8 Conclusion

In this work, we took a close look at some of the key steps used in statistical models for EoS inference from observations of neutron star mergers. We highlight the importance of the underlying physics that is often overlooked in favor of fit formulae used to obtain single values of, for example, the remnant accretion disk mass or the wind mass from that disk. By propagating this uncertainty through the many degeneracies in a full inference, we hope to motivate studies aimed at probing these different physical problems. We look forward to our proposed fitting model being put to the test with new simulation data.

CHAPTER
SEVEN

SUMMARY & OUTLOOK

It is broadly accepted that roughly half the production of elements heavier than iron can be attributed to the rapid neutron capture process (*r*-process). The first multi-messenger observation of the binary neutron star merger, GW170817, cemented these sites as being capable of producing *r*-process elements up to and including the lanthanides ($57 \leq Z \leq 71$). To date, this has been the only observation of a lanthanide-producing event; our understanding of *r*-process production is otherwise subject to recording abundances in enriched sites in our galaxy such as *r*-process-enhanced metal-poor stars or the Solar System. Explaining the history of this galactic enrichment, at least to the extent that it comes from binary neutron star mergers, is a multi-physics question involving uncertainties across scales spanning several orders of magnitude in time and space.

Theoretical calculations and simulations, such as those contained in this dissertation, play a part in a cycle whereby observations constrain models, and models help motivate and inform the interpretation of future observations and experiments. In this work, I investigated questions stemming from both understanding the environment in which *r*-process production occurs as well as the uncertain nuclear properties involved in predicting nuclear pathways towards an *r*-process pattern.

One of the earliest time scales over which the question of nucleosynthesis in neutron star mergers occurs is in the initial deforming and redistribution of material that at one point existed in the form of two separate neutron stars. The nuclear equation of state describes the behavior of matter at or above nuclear densities when subjected to the stresses of a merger event, and therefore plays a large role in predicting where material ends up. In particular, numerical relativity simulations (see Appendix D) show that there is a relation between equation of state-informed variables, such as tidal deformability or compactness, and the mass of the disk resulting from the merger. Several works have identified these relations and have sought to determine a fit formula that best predicts the disk mass based on one of these variables. The compactness of the lightest neutron star in a binary proves a good predictor of the disk mass resulting from the merger, as shown in Chapter 6. As numerical relativity simulations of binary mergers continue to improve in resolution and sophistication, fit formulae such as Equation 6.1 will certainly be put to the test.

Relating equation of state and binary properties to the disk mass neglects mass emerging on earlier time scales of the merger, namely the dynamical ejecta. As discussed in Section 1.3.2, some amount of *r*-process material is expected to be produced in the dynamical ejecta; an understanding of the full extent of possible *r*-process production in neutron star mergers is not complete without including this component of the ejecta.

Only material that becomes unbound from the post-merger disk can be useful in enriching the galaxy with *r*-process material. Estimating the disk mass gives an idea of the scale of the mass outflow, e.g. how many solar masses of lanthanides can be produced in a single event. Beyond this, the evolution of the mass outflow and the nucleosynthesis that occurs as the disk evolves is the realm of GRMHD. Remnant magnetic fields seed the post-merger system and influence its evolution. Chapter 5 investigates this by exploring the uncertainty in the initial strength of these magnetic fields. This work found that varying the initial magnetic field strength resulted in two major effects. The first was the effect on the time

scale and magnitude of the outflow: a stronger magnetic field resulted in an ejecta mass almost 4 times greater than a weaker field. Furthermore, the mass ejection history varied with this changing magnetic field, with weaker fields resulting in delayed outflows.

Changing the initial magnetic field strength did not affect each disk's ability to produce a full *r*-process pattern, including the actinides. However, the differences in outflow time scales did have an effect on the resulting abundance patterns as well as the resulting geometry of the outflow. One of the most notable differences was in the production of actinides compared to lanthanides. Although the absolute lanthanide mass varied in each disk, the relative lanthanide abundances produced were roughly similar. This contrasts with the actinide patterns, which showed a greater sensitivity to magnetic field strength, decreasing in abundance with decreasing magnetic field strength.

Variety in the lanthanide to actinide abundance ratios naturally emerged from this work by simply changing the initial magnetic field strength. While still inconclusive, this represents an exciting prospect for explaining the same variation as it is observed in *r*-process-enhanced metal-poor stars. Given the variety of magnetic field strengths naturally occurring in neutron stars, it is not unlikely that a similar variety would exist in the systems resulting from their mergers. One possible future direction would be to more carefully investigate possible connections between magnetic field properties and the lanthanide to actinide ratio based on data from stellar observations.

The variation of the *final* abundance pattern resulting from the variation of magnetic field strength is likely accompanied by variation in the time-dependent abundance patterns, which could have profound impact on the kilonova signal. While this is alluded to in Chapter 5, it was not fully explored in this work and remains an opportunity for study. Differences in the time-dependent nucleosynthetic conditions in the outflow arising from differences in disk parameters such as magnetic field strength or geometry would then combine with uncertainties in the properties of nuclei far from stability, which was the main theme of the work contained in Chapter 4. In this work, uncertainties in the β -decay rates of off-stability nuclei were compared in nucleosynthesis calculations alongside other nuclear properties, such as mass and descriptions of fission.

One goal of nucleosynthesis studies where nuclear properties are varied is often the identification of key nuclei or regions where measurements are lacking, whose properties could have consequences on observable signals. Such was the case in this work as well; several nuclei were identified as potentially being important for setting the shape of the nuclear heating on a time scale that could impact the kilonova signal. This work found that slower β -decay rates above the N=126 shell closure resulted in larger heating rates between 1-10 days, largely due to two mechanisms. One was the influence of different β -decay rates on the branching ratios of individual nuclei around $Z \sim 104$. In some cases, larger β -decay time scales resulted in a dominance of decay via spontaneous fission, thereby changing not only the time scale, but also the energetics of the decays. The second effect was more indirect and saw the population of important α -decaying nuclei (with measured properties) being affected by unmeasured parent nuclei.

Identifying these key nuclei sets the stage for the incorporation of the results of both experimental and theoretical endeavors. The next several years will see heavy ion beam facilities, such as the Facility for Rare Isotope Beams (FRIB), experimentally probing more and more neutron rich isotopes, populating the neutron-heavy side of the chart of the nuclides with data, overlapping with some of the nuclei and regions in Chapter 4 (Surman, Rebecca and Mumpower, Matthew 2018). The $N = 126$ shell closure is another target for ongoing and upcoming nuclear experiment endeavors. While the $N = 8, 20, 50$, and even 82 shell closures have experimental data, the $N = 126$ closure remains relatively unpopulated, experimentally. In addition to insights into fundamental questions of nuclear structure, these experimental efforts will play a large part in reducing the uncertainty in nucleosynthesis predictions stemming from nuclear properties away from stability. Additionally, theoretical efforts can be targeted toward more accurately modeling nuclei still inaccessible by experimental efforts, hopefully refining our ability to predict observable signals caused by the behavior of individual nuclei; this will be vital for identifying signatures of specific element production in future kilonova observations.

Beyond the potential identification of features caused by the production of specific nuclei, the work in Chapter 6 shows broader implications for the combined effect of uncertainties starting from the merger itself out to the observation of kilonova features. This work only used multi-messenger data from GW170817 to provide constraints on the nuclear equation of state. While future multi-messenger observations will certainly allow for more robust constraints, the steps involved in interpreting these observations, as outlined in this work, are subject to the numerous sources of uncertainty, including the ones investigated in this dissertation. These are often simplified for ease of calculation, but as shown in Chapter 6, can rather profoundly impact the interpretation of observational data.

Finally, there is the question of stellar observations. In Chapter 4, uncertainties in abundance patterns stemming from the use of different β -decay rates were compared to observations of five *r*-process-enhanced, metal-poor stars notable for their uranium detections. Meanwhile, large observational campaigns such as those carried out by the *r*-process Alliance (RPA) continue to increase the amount of metal-poor star observations. Doing so provides the opportunity to paint a more complete picture of the history of *r*-process production in the Milky Way. Additional measurements of thorium and uranium will provide the possibility of using this chronometer pair to compare stellar observations to more complete simulations and nucleosynthesis studies from neutron star mergers.

Overall, the work in this thesis reinforces the 50-year old idea that neutron star mergers provide the conditions for *r*-process nucleosynthesis. Each individual work contained in this thesis probed different stages of the merger and predictions of the nucleosynthetic outcomes from secular ejecta. However, late-time abundance patterns, though influenced by a variety of uncertainties, consistently produced a full *r*-process pattern. This work closely investigated uncertainties ranging from the distribution of material during and after the merger to the variety of theoretical predictions of nuclear properties far from stability. It is the author's hope that this work will provide a useful addition to other contemporary works in motivating further experimental and theoretical endeavors as well as informing the interpretation of the wealth of data and observations that will surely come in the next few years.

APPENDICES

APPENDIX

A

VARIABLES

Table A.1: A summary of common acronyms and their abbreviations.

| Variable | Abbreviation |
|---|--------------|
| Kilonova (Kilonovae) | KN (KNe) |
| Neutron Star Merger | NSM |
| Equation of State | EoS |
| Magnetohydrodynamics | MHD |
| General Relativistic Magnetohydrodynamics | GRMHD |

Table A.2: A list of common physical variables used in this work.

| | |
|---------|------------------------------------|
| Y_e | Electron fraction |
| β | Ratio of gas to magnetic pressure. |
| s | entropy |

Table A.3: A list of common physical constants and their abbreviations.

| | |
|------------------------|-------|
| Gravitational Constant | G |
| Speed of light | c |
| Boltzmann constant | k_B |
| proton number | Z |
| neutron number | N |
| mass number | A |

APPENDIX
B

GRID SIZE AND RESOLUTION

In order to ensure that our grid resolution is sufficient to capture the MRI, we use the quality factors defined in Miller et al. (2019b), following both Sano et al. (2004) and Siegel and Metzger (2018). The first quality factor describes the number of grid points per minimum unstable MRI wavelength inside the disk:

$$Q_{MRI}^{(\theta)} = \frac{2\pi b^{(\theta)}}{\Delta x^{(\theta)} \sqrt{w + b^2 \Omega}}, \quad (\text{B.1})$$

where $b^{(\theta)}$ is the θ -component of the magnetic field, Δx is the grid spacing in the θ direction, w is the enthalpy of the fluid, and $b^2 = b^\mu b_\mu$ is the total magnetic field strength.

A similar quality factor can be defined using the strength of the magnetic field in the comoving frame rather than the lab frame:

$$Q_{MRI}^{(c)} = \frac{b}{b^{(\theta)}} Q_{MRI}^{(\theta)}, \quad (\text{B.2})$$

where $b = \sqrt{b^\mu b_\mu}$.

We plot the ϕ -averaged value of both these quantities in the midplane at 25 ms. in Figure B.1. We follow the coloring conventions for each of the three disks established in this work, and show the factor $Q_{MRI}^{(\theta)}$ as dotted lines and $Q_{MRI}^{(c)}$ as solid lines. We find that all three disks exhibit $Q_{MRI}^{(c)} \gg 10$ and $Q_{MRI}^{(\theta)} \gtrsim 10$ at this early time. Furthermore, we highlight that the behavior of our b100 disk (light blue lines) match that of the same disk as presented in Miller et al. (2019b), as can be seen by comparing the red and blue solid lines of Figure 8 in the same work.

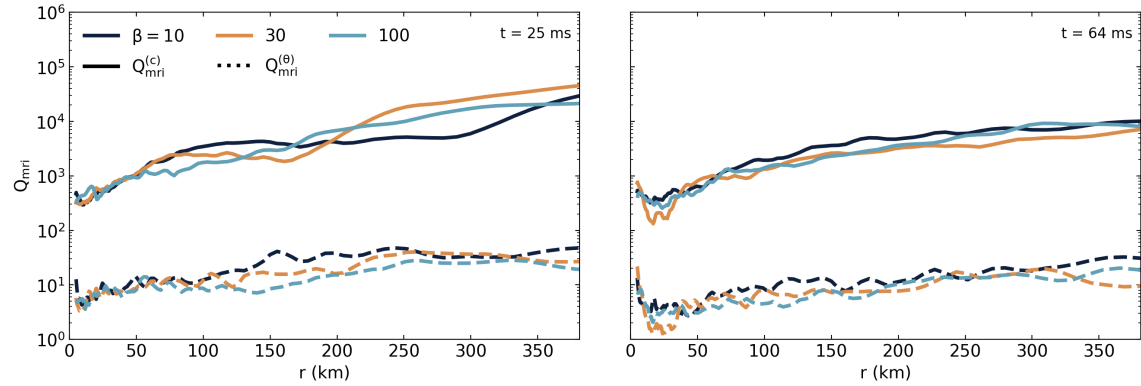


Figure B.1: Quality factor for the MRI, averaged over ϕ in the midplane at 25 ms (left) and 64 ms (right) for each disk. The quality factor for the lab frame, vertical component of the magnetic field is shown as dashed lines while the comoving field is shown as solid lines.

APPENDIX
C

DISK MASS FIT FORMULAE

In this Appendix, we describe some of the proposed methods for estimating the resulting disk mass from an NSM.

C.1 Binary Tidal Deformability

The tidal deformability of a binary system depends on the tidal deformability of the individual binary components (from De et al. (2018)¹):

$$\tilde{\Lambda} = \frac{16}{13} \frac{(12q + 1)\Lambda_{\text{heavy}} + (12 + q)q^4\Lambda_{\text{light}}}{(1+q)^5}, \text{ where} \quad (\text{C.1})$$

$$q = \frac{m_{\text{light}}}{m_{\text{heavy}}} \leq 1, \text{ and} \quad (\text{C.2})$$

$$\Lambda_{\text{light,heavy}} = \frac{2}{3}k_2 \left(\frac{R_{\text{light,heavy}}c^2}{Gm_{\text{light,heavy}}} \right)^5. \quad (\text{C.3})$$

Radice et al. (2018b) evaluated a grid of 35 numerical relativity (NR) simulations with 4 different EoSs. From the results of these calculations, they propose a best-fit formula for the disk mass that depends on the tidal deformability, $\tilde{\Lambda}$, of the binary:

$$\frac{M_{\text{disk}}}{M_{\odot}} = \max \left\{ 10^{-3}, \alpha + \beta \tanh \left(\frac{\tilde{\Lambda} - \gamma}{\delta} \right) \right\}, \quad (\text{C.4})$$

with $\alpha = 0.084$, $\beta = 0.127$, $\gamma = 567.1$, and $\delta = 405.14$.

¹The literature often uses subscripts (1,2) followed by a designation of each to either the lightest or heaviest NS in the binary. However, due to the lack of consistent designation of the smallest/largest component in the literature, throughout this work, we use subscripts "light" and "heavy" to avoid any confusion.

C.2 Prompt Collapse Threshold Mass

Coughlin et al. (2019) take the NR simulations from Radice et al. (2018b) (hereafter Rad18) and highlight that the lifetime of the post-merger remnant is related to the stability of said remnant, and this lifetime is strongly correlated with the resulting disk mass. Given the finding that the remnant lifetime prior to collapse is governed in large part by the ratio of the binary mass to the threshold mass (above which there is prompt collapse to a black hole). The threshold mass can be computed following Bauswein et al. (2013a):

$$M_{\text{Thresh}} = (-jC_{1.6}^* + a)M_{\text{TOV}}, \text{ where} \quad (\text{C.5})$$

$$C_{1.6}^* = \frac{GM_{\text{TOV}}}{c^2 R_{1.6}}, \quad (\text{C.6})$$

and best-fit parameters $j = 3.606$ and $a = 2.380$.

Based on the NR simulations from Rad18 and the correlation of the binary threshold mass with the resulting disk mass, Coughlin et al. (2019) propose the following relation:

$$\log_{10}\left(\frac{M_{\text{disk}}}{M_{\odot}}\right) = \max\left\{-3, a\left(1 + b \tanh\frac{c - M_{\text{tot}}/M_{\text{thr}}}{d}\right)\right\}, \quad (\text{C.7})$$

where $a = -31.335$, $b = -0.9760$, $c = 1.0474$, and $d = 0.05957$.

This relation removes dependence on the properties of the binary itself, but maintains a dependence on the tidal deformability via the compactness, and can therefore be used to characterize an EoS. However subsequent work (Dietrich et al. 2020) (hereafter D+20) compares results from 73 NR simulations performed by various groups resulting in a modified formulation of the resulting disk mass that incorporates a dependence on the binary mass ratio by modifying the parameters such that

$$a = a_0 + \delta a \cdot \xi \quad (\text{C.8})$$

$$b = b_0 + \delta b \cdot \xi, \quad (\text{C.9})$$

where the parameter ξ is given by:

$$\xi = \frac{1}{2} \tanh(\beta(\hat{q} - \hat{q}_{\text{trans}})). \quad (\text{C.10})$$

Here $\hat{q} = m_{\text{light}}/m_{\text{heavy}} \leq 1$ is the inverse binary mass ratio; \hat{q}_{trans} and β are free parameters. D+20 report best-fit parameters $a_0 = -1.581$, $\delta a = -2.439$, $b_0 = -0.538$, $\delta b = -0.406$, $c = 0.953$, $d = 0.0417$, $\beta = 3.910$, and $\hat{q}_{\text{trans}} = 0.900$.

C.3 Lightest NS Compactness

Additional efforts to continue to improve upon the results from Rad18 and Coughlin et al. (2019) were made by Krüger and Foucart (2020) (hereafter KF20) by incorporating disk masses from an additional 22 NR simulations from Kiuchi et al. (2019) that included asymmetric binary mass ratios. These efforts resulted in a formulation dependent on the compactness parameter:

$$C = \frac{GM}{c^2 R} \quad (C.11)$$

of the lighter of the two neutron stars, C_{light} :

$$M_{\text{disk}} = m_{\text{light}} \cdot \max \left\{ 5 \times 10^4, (aC_{\text{light}} + c)^d \right\}, \quad (C.12)$$

with best-fit parameters $a = -8.1324$, $c = 1.4820$, and $d = 1.7784$.

APPENDIX
D

NUMERICAL RELATIVITY SIMULATIONS OF BINARY NEUTRON STAR MERGERS

Compiled below are the 112 data points used in Section 6.3, sorted by EoS. Included in the table, for each binary with total mass, M , are the masses of each component, with m_l (m_h) referring to the lighter (heavier) companion. The mass ratio, q , is included and defined such that

$$q = \frac{m_{\text{light}}}{m_{\text{heavy}}} \leq 1. \quad (\text{D.1})$$

Also included is the compactness of the lighter neutron star, C_l . The resulting disk mass, m_{disk} and reference are also included. Figure D.1 shows the resulting disk mass from each simulation as a function of the binary tidal deformability (as defined in Equation C.1), the ratio of the binary to threshold mass, and C_{light} (as defined in Equation C.11).

Table D.1: Simulation data from numerical relativity simulations.

| EoS | m_l (M_\odot) | m_h (M_\odot) | M (M_\odot) | q | C_l | m_{disk} (M_\odot) | Reference |
|-------------|---------------------|---------------------|-------------------|-------|-------|---------------------------------|-----------------------|
| BHBA ϕ | 1.20 | 1.40 | 2.60 | 0.857 | 0.13 | 2.07e-01 | Radice et al. (2018b) |
| BHBA ϕ | 1.20 | 1.40 | 2.60 | 0.857 | 0.13 | 2.26e-01 | Radice et al. (2018b) |
| BHBA ϕ | 1.25 | 1.36 | 2.62 | 0.916 | 0.14 | 1.87e-01 | Radice et al. (2018b) |
| BHBA ϕ | 1.35 | 1.35 | 2.70 | 1.000 | 0.15 | 1.28e-01 | Radice et al. (2018b) |
| BHBA ϕ | 1.35 | 1.35 | 2.70 | 1.000 | 0.15 | 1.43e-01 | Radice et al. (2018b) |
| BHBA ϕ | 1.35 | 1.35 | 2.70 | 1.000 | 0.15 | 1.44e-01 | Radice et al. (2018b) |
| BHBA ϕ | 1.39 | 1.44 | 2.83 | 0.965 | 0.16 | 8.28e-02 | Radice et al. (2018b) |
| BHBA ϕ | 1.40 | 1.40 | 2.80 | 1.000 | 0.16 | 5.38e-02 | Radice et al. (2018b) |
| BHBA ϕ | 1.40 | 1.40 | 2.80 | 1.000 | 0.16 | 7.05e-02 | Radice et al. (2018b) |
| BHBA ϕ | 1.50 | 1.50 | 3.00 | 1.000 | 0.17 | 1.93e-02 | Radice et al. (2018b) |

| BHBA ϕ | 1.60 | 1.60 | 3.20 | 1.000 | 0.18 | 9.00e-04 | Radice et al. (2018b) |
|-------------|------|------|------|-------|------|----------|--------------------------|
| BLh | 1.07 | 1.77 | 2.84 | 0.602 | 0.13 | 2.44e-01 | Bernuzzi et al. (2020) |
| BLh | 1.07 | 1.77 | 2.84 | 0.602 | 0.13 | 2.54e-01 | Bernuzzi et al. (2020) |
| BLh | 1.07 | 1.77 | 2.84 | 0.602 | 0.13 | 2.65e-01 | Bernuzzi et al. (2020) |
| BLh | 1.10 | 1.70 | 2.80 | 0.649 | 0.13 | 2.45e-01 | Nedora et al. (2021) |
| BLh | 1.10 | 1.70 | 2.80 | 0.649 | 0.13 | 2.59e-01 | Nedora et al. (2021) |
| BLh | 1.18 | 1.58 | 2.76 | 0.746 | 0.14 | 1.66e-01 | Nedora et al. (2021) |
| BLh | 1.18 | 1.58 | 2.76 | 0.746 | 0.14 | 2.02e-01 | Camilletti et al. (2024) |
| BLh | 1.18 | 1.58 | 2.76 | 0.746 | 0.14 | 2.27e-01 | Nedora et al. (2021) |
| BLh | 1.36 | 1.36 | 2.73 | 1.000 | 0.16 | 9.55e-02 | Nedora et al. (2021) |
| BLh | 1.36 | 1.36 | 2.73 | 1.000 | 0.16 | 1.14e-01 | Perego et al. (2022) |
| BLh | 1.36 | 1.36 | 2.73 | 1.000 | 0.16 | 1.25e-01 | Nedora et al. (2021) |
| BLh | 1.36 | 1.36 | 2.73 | 1.000 | 0.16 | 1.33e-01 | Bernuzzi et al. (2020) |
| BLh | 1.36 | 1.36 | 2.73 | 1.000 | 0.16 | 2.08e-01 | Nedora et al. (2021) |
| BLh | 1.52 | 1.80 | 3.32 | 0.847 | 0.18 | 3.00e-03 | Camilletti et al. (2022) |
| BLh | 1.56 | 1.75 | 3.31 | 0.893 | 0.19 | 5.00e-04 | Camilletti et al. (2022) |
| BLh | 1.56 | 1.75 | 3.31 | 0.893 | 0.19 | 1.00e-03 | Camilletti et al. (2022) |
| DD2 | 1.08 | 1.80 | 2.88 | 0.599 | 0.12 | 2.75e-01 | Camilletti et al. (2024) |
| DD2 | 1.20 | 1.40 | 2.60 | 0.857 | 0.13 | 1.93e-01 | Radice et al. (2018b) |
| DD2 | 1.20 | 1.40 | 2.60 | 0.857 | 0.13 | 1.95e-01 | Radice et al. (2018b) |
| DD2 | 1.25 | 1.36 | 2.62 | 0.916 | 0.14 | 2.08e-01 | Radice et al. (2018b) |
| DD2 | 1.25 | 1.49 | 2.74 | 0.840 | 0.14 | 2.56e-01 | Cusinato et al. (2022) |
| DD2 | 1.25 | 1.50 | 2.74 | 0.833 | 0.14 | 2.53e-01 | Nedora et al. (2021) |
| DD2 | 1.30 | 1.43 | 2.73 | 0.909 | 0.15 | 2.35e-01 | Cusinato et al. (2022) |
| DD2 | 1.30 | 1.44 | 2.73 | 0.901 | 0.14 | 2.58e-01 | Cusinato et al. (2022) |
| DD2 | 1.35 | 1.35 | 2.70 | 1.000 | 0.15 | 1.51e-01 | Radice et al. (2018b) |
| DD2 | 1.35 | 1.35 | 2.70 | 1.000 | 0.15 | 1.57e-01 | Radice et al. (2018b) |
| DD2 | 1.35 | 1.35 | 2.70 | 1.000 | 0.15 | 1.62e-01 | Radice et al. (2018b) |
| DD2 | 1.36 | 1.36 | 2.73 | 1.000 | 0.15 | 1.81e-01 | Perego et al. (2019) |
| DD2 | 1.36 | 1.36 | 2.73 | 1.000 | 0.15 | 2.12e-01 | Nedora et al. (2019) |
| DD2 | 1.39 | 1.44 | 2.83 | 0.965 | 0.16 | 1.44e-01 | Radice et al. (2018b) |
| DD2 | 1.40 | 1.40 | 2.80 | 1.000 | 0.16 | 1.24e-01 | Radice et al. (2018b) |
| DD2 | 1.40 | 1.40 | 2.80 | 1.000 | 0.16 | 1.69e-01 | Radice et al. (2018b) |
| DD2 | 1.50 | 1.50 | 3.00 | 1.000 | 0.17 | 1.67e-01 | Radice et al. (2018b) |
| DD2 | 1.60 | 1.60 | 3.20 | 1.000 | 0.18 | 1.96e-02 | Radice et al. (2018b) |
| LS220 | 1.07 | 1.77 | 2.84 | 0.602 | 0.12 | 1.16e-01 | Bernuzzi et al. (2020) |
| LS220 | 1.07 | 1.77 | 2.84 | 0.602 | 0.12 | 1.18e-01 | Bernuzzi et al. (2020) |
| LS220 | 1.14 | 1.64 | 2.78 | 0.699 | 0.13 | 1.85e-01 | Nedora et al. (2021) |

| | | | | | | | |
|-------|------|------|------|-------|------|----------|--------------------------|
| LS220 | 1.20 | 1.20 | 2.40 | 1.000 | 0.14 | 1.74e-01 | Radice et al. (2018b) |
| LS220 | 1.20 | 1.40 | 2.60 | 0.857 | 0.14 | 1.21e-01 | Radice et al. (2018b) |
| LS220 | 1.20 | 1.40 | 2.60 | 0.857 | 0.14 | 1.40e-01 | Radice et al. (2018b) |
| LS220 | 1.20 | 1.40 | 2.60 | 0.857 | 0.14 | 2.03e-01 | Radice et al. (2018b) |
| LS220 | 1.20 | 1.40 | 2.60 | 0.857 | 0.14 | 2.28e-01 | Radice et al. (2018b) |
| LS220 | 1.20 | 1.40 | 2.60 | 0.857 | 0.14 | 2.34e-01 | Radice et al. (2018b) |
| LS220 | 1.25 | 1.36 | 2.62 | 0.916 | 0.15 | 8.81e-02 | Radice et al. (2018b) |
| LS220 | 1.25 | 1.36 | 2.62 | 0.916 | 0.14 | 1.69e-01 | Radice et al. (2018b) |
| LS220 | 1.27 | 1.47 | 2.74 | 0.862 | 0.15 | 1.24e-01 | Nedora et al. (2021) |
| LS220 | 1.35 | 1.35 | 2.70 | 1.000 | 0.16 | 4.65e-02 | Radice et al. (2018b) |
| LS220 | 1.35 | 1.35 | 2.70 | 1.000 | 0.16 | 7.25e-02 | Radice et al. (2018b) |
| LS220 | 1.35 | 1.35 | 2.70 | 1.000 | 0.16 | 8.59e-02 | Radice et al. (2018b) |
| LS220 | 1.35 | 1.35 | 2.70 | 1.000 | 0.16 | 9.06e-02 | Radice et al. (2018b) |
| LS220 | 1.35 | 1.35 | 2.70 | 1.000 | 0.16 | 1.41e-01 | Radice et al. (2018b) |
| LS220 | 1.35 | 1.35 | 2.70 | 1.000 | 0.16 | 1.42e-01 | Radice et al. (2018b) |
| LS220 | 1.36 | 1.36 | 2.73 | 1.000 | 0.16 | 5.02e-02 | Nedora et al. (2019) |
| LS220 | 1.36 | 1.36 | 2.73 | 1.000 | 0.16 | 6.31e-02 | Nedora et al. (2019) |
| LS220 | 1.36 | 1.36 | 2.73 | 1.000 | 0.16 | 6.97e-02 | Nedora et al. (2019) |
| LS220 | 1.36 | 1.36 | 2.73 | 1.000 | 0.16 | 1.61e-01 | Nedora et al. (2019) |
| LS220 | 1.39 | 1.44 | 2.83 | 0.965 | 0.16 | 3.91e-02 | Radice et al. (2018b) |
| LS220 | 1.40 | 1.40 | 2.80 | 1.000 | 0.16 | 2.68e-02 | Radice et al. (2018b) |
| LS220 | 1.40 | 1.40 | 2.80 | 1.000 | 0.16 | 3.12e-02 | Radice et al. (2018b) |
| LS220 | 1.40 | 1.40 | 2.80 | 1.000 | 0.16 | 4.58e-02 | Radice et al. (2018b) |
| LS220 | 1.45 | 1.45 | 2.90 | 1.000 | 0.17 | 2.05e-02 | Radice et al. (2018b) |
| LS220 | 1.50 | 1.50 | 3.00 | 1.000 | 0.18 | 1.60e-03 | Radice et al. (2018b) |
| LS220 | 1.60 | 1.60 | 3.20 | 1.000 | 0.19 | 7.00e-04 | Radice et al. (2018b) |
| SFHo | 1.07 | 1.77 | 2.84 | 0.602 | 0.13 | 9.06e-02 | Bernuzzi et al. (2020) |
| SFHo | 1.20 | 1.40 | 2.60 | 0.857 | 0.15 | 1.17e-01 | Radice et al. (2018b) |
| SFHo | 1.20 | 1.40 | 2.60 | 0.857 | 0.15 | 1.57e-01 | Radice et al. (2018b) |
| SFHo | 1.28 | 1.45 | 2.73 | 0.885 | 0.16 | 7.75e-02 | Nedora et al. (2021) |
| SFHo | 1.35 | 1.35 | 2.70 | 1.000 | 0.17 | 1.23e-02 | Radice et al. (2018b) |
| SFHo | 1.35 | 1.35 | 2.70 | 1.000 | 0.17 | 1.78e-02 | Radice et al. (2018b) |
| SFHo | 1.35 | 1.35 | 2.70 | 1.000 | 0.17 | 2.79e-02 | Radice et al. (2018b) |
| SFHo | 1.35 | 1.35 | 2.70 | 1.000 | 0.17 | 6.23e-02 | Radice et al. (2018b) |
| SFHo | 1.39 | 1.44 | 2.83 | 0.965 | 0.17 | 9.00e-04 | Radice et al. (2018b) |
| SFHo | 1.40 | 1.40 | 2.80 | 1.000 | 0.17 | 1.00e-04 | Radice et al. (2018b) |
| SFHo | 1.44 | 1.91 | 3.35 | 0.752 | 0.18 | 1.09e-02 | Camilletti et al. (2022) |
| SFHo | 1.46 | 1.46 | 2.92 | 1.000 | 0.18 | 2.00e-04 | Radice et al. (2018b) |

| | | | | | | | |
|------------------|------|------|------|-------|------|----------|--------------------------|
| SFHo | 1.52 | 1.80 | 3.32 | 0.847 | 0.19 | 5.00e-04 | Camilletti et al. (2022) |
| SFHo | 1.52 | 1.80 | 3.32 | 0.847 | 0.19 | 5.00e-04 | Camilletti et al. (2022) |
| SLy4 | 1.28 | 1.45 | 2.73 | 0.885 | 0.16 | 6.87e-02 | Nedora et al. (2021) |
| SLy4 | 1.36 | 1.36 | 2.73 | 1.000 | 0.17 | 4.17e-02 | Endrizzi et al. (2020) |
| $\Gamma = 2.528$ | 1.38 | 1.38 | 2.75 | 1.000 | 0.16 | 5.30e-02 | Kiuchi et al. (2019) |
| $\Gamma = 2.528$ | 1.20 | 1.55 | 2.75 | 0.775 | 0.14 | 1.60e-01 | Kiuchi et al. (2019) |
| $\Gamma = 2.640$ | 1.38 | 1.38 | 2.75 | 1.000 | 0.16 | 1.20e-01 | Kiuchi et al. (2019) |
| $\Gamma = 2.825$ | 1.38 | 1.38 | 2.75 | 1.000 | 0.18 | 1.80e-02 | Kiuchi et al. (2019) |
| $\Gamma = 2.825$ | 1.20 | 1.55 | 2.75 | 0.775 | 0.15 | 8.70e-02 | Kiuchi et al. (2019) |
| $\Gamma = 2.942$ | 1.20 | 1.55 | 2.75 | 0.775 | 0.15 | 1.20e-01 | Kiuchi et al. (2019) |
| $\Gamma = 2.942$ | 1.38 | 1.38 | 2.75 | 1.000 | 0.18 | 1.60e-02 | Kiuchi et al. (2019) |
| $\Gamma = 3.132$ | 1.38 | 1.38 | 2.75 | 1.000 | 0.18 | 5.00e-04 | Kiuchi et al. (2019) |
| $\Gamma = 3.132$ | 1.20 | 1.55 | 2.75 | 0.775 | 0.16 | 6.30e-02 | Kiuchi et al. (2019) |
| $\Gamma = 3.252$ | 1.20 | 1.55 | 2.75 | 0.775 | 0.16 | 1.20e-01 | Kiuchi et al. (2019) |
| $\Gamma = 3.252$ | 1.38 | 1.38 | 2.75 | 1.000 | 0.18 | 1.90e-03 | Kiuchi et al. (2019) |
| $\Gamma = 3.370$ | 1.38 | 1.38 | 2.75 | 1.000 | 0.18 | 3.10e-02 | Kiuchi et al. (2019) |
| $\Gamma = 3.446$ | 1.38 | 1.38 | 2.75 | 1.000 | 0.19 | 5.00e-04 | Kiuchi et al. (2019) |
| $\Gamma = 3.446$ | 1.20 | 1.55 | 2.75 | 0.775 | 0.17 | 3.60e-02 | Kiuchi et al. (2019) |
| $\Gamma = 3.568$ | 1.38 | 1.38 | 2.75 | 1.000 | 0.19 | 5.00e-04 | Kiuchi et al. (2019) |
| $\Gamma = 3.568$ | 1.20 | 1.55 | 2.75 | 0.775 | 0.17 | 3.80e-02 | Kiuchi et al. (2019) |
| $\Gamma = 3.687$ | 1.38 | 1.38 | 2.75 | 1.000 | 0.19 | 7.80e-03 | Kiuchi et al. (2019) |
| $\Gamma = 3.765$ | 1.38 | 1.38 | 2.75 | 1.000 | 0.20 | 5.00e-04 | Kiuchi et al. (2019) |
| $\Gamma = 3.765$ | 1.20 | 1.55 | 2.75 | 0.775 | 0.17 | 2.30e-02 | Kiuchi et al. (2019) |
| $\Gamma = 3.887$ | 1.38 | 1.38 | 2.75 | 1.000 | 0.19 | 5.00e-04 | Kiuchi et al. (2019) |
| $\Gamma = 3.887$ | 1.20 | 1.55 | 2.75 | 0.775 | 0.17 | 2.90e-02 | Kiuchi et al. (2019) |
| $\Gamma = 4.007$ | 1.38 | 1.38 | 2.75 | 1.000 | 0.19 | 2.70e-03 | Kiuchi et al. (2019) |

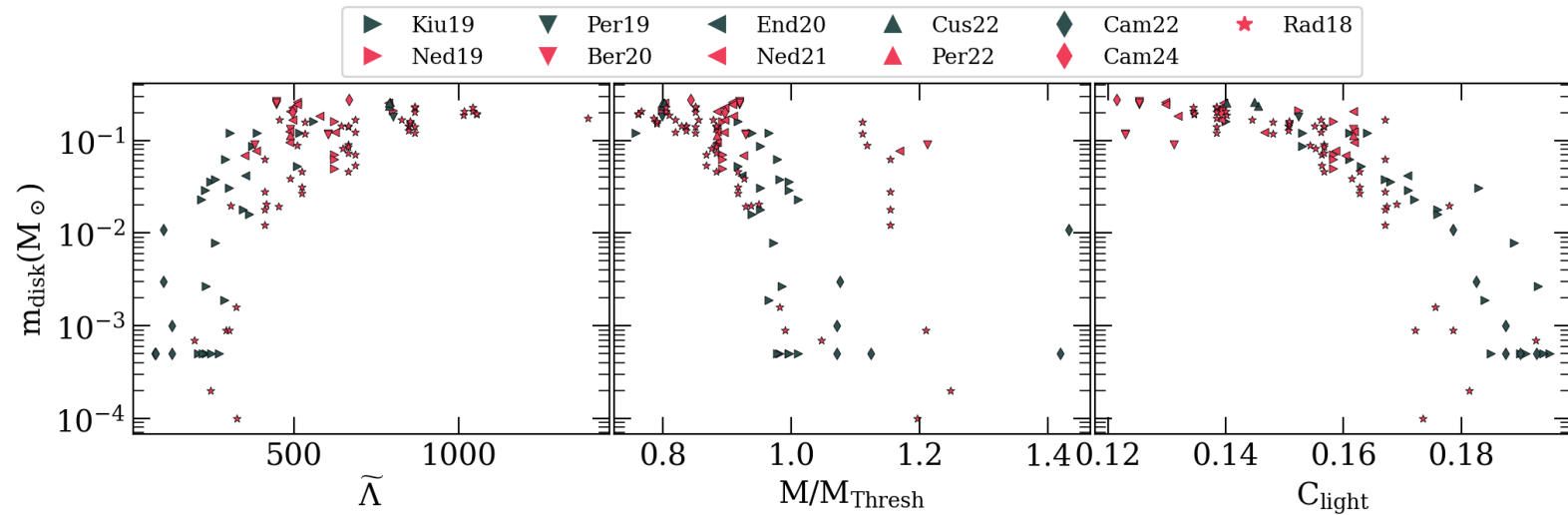


Figure D.1: Disk masses from NR simulations, shown as a function of the binary tidal deformability (left), the ratio of the total binary mass to the black hole-formation threshold mass (center), and the compactness of the smallest binary component (right). The legend indicates the sources from which each data point was extracted by the first three letters of the principal author followed by the publication year.

REFERENCES

- Abbott, B., LIGO Scientific Collaboration, and Virgo Collaboration (2017a). Gravitational waves and gamma-rays from a binary neutron star merger: Gw170817 and grb 170817a. *ApJ Letters*, 848(2):L13.
- Abbott, B., LIGO Scientific Collaboration, and Virgo Collaboration (2017b). Gw170817: Observation of gravitational waves from a binary neutron star inspiral. *Physical Review Letters*, 119(16):30–33.
- Abbott, B., LIGO Scientific Collaboration, and Virgo Collaboration (2017c). Multi-messenger Observations of a Binary Neutron Star Merger. *ApJL*, 848:L12.
- Abbott, B., LIGO Scientific Collaboration, and Virgo Collaboration (2018). GW170817: Measurements of Neutron Star Radii and Equation of State. *Physical Review Letters*, 121(16):161101.
- Aboussir, Y., Pearson, J., Dutta, A., and Tondeur, F. (1995). Nuclear mass formula via an approximation to the Hartree-Fock method. *Atomic Data and Nuclear Data Tables*, 61(1):127–176.
- Abramowicz, M. A., Blaes, O. M., Horák, J., Kluzniak, W., and Rebusco, P. (2006). Epicyclic oscillations of fluid bodies: II. Strong gravity. *Classical and Quantum Gravity*, 23(5):1689–1696.
- Abramowicz, M. A. and Fragile, P. C. (2013). Foundations of Black Hole Accretion Disk Theory. *Living Reviews in Relativity*, 16(1):1.
- Agathos, M., Zappa, F., and Sebastiano Bernuzzi, et al. (2020). Inferring prompt black-hole formation in neutron star mergers from gravitational-wave data. *Physical Review D*, 101:044006.
- Alexander, K. D., Berger, E., and W. Fong , et al. (2017). The electromagnetic counterpart of the binary neutron star merger ligo/virgo gw170817. vi. radio constraints on a relativistic jet and predictions for late-time emission from the kilonova ejecta. *ApJ Letters*, 848(2):L21.
- Allmond, M., Appiah, K., and Bollen, G. , et al. (2020). Frib decay station.
- Alpher, R. A., Bethe, H., and Gamow, G. (1948). The origin of chemical elements. *Phys. Rev.*, 73:803–804.
- Aprahamian, A., Surman, R., Frebel, A., and McLaughlin, G. C. , et al. (2018). Frib and the gw170817 kilonova.
- Arcones, A., Janka, H. T., and Scheck, L. (2007). Nucleosynthesis-relevant conditions in neutrino-driven supernova outflows. I. Spherically symmetric hydrodynamic simulations. *A&A*, 467(3):1227–1248.
- Arcones, A. and Martínez-Pinedo, G. (2011). Dynamical r -process studies within the neutrino-driven wind scenario and its sensitivity to the nuclear physics input. *Physical Review C*, 83:045809.
- Arcones, A. and Thielemann, F.-K. (2012). Neutrino-driven wind simulations and nucleosynthesis of heavy elements. *Journal of Physics G: Nuclear and Particle Physics*, 40(1):013201.
- Arlandini, C., Käppeler, F., and Klaus Wissak , et al. (1999). Neutron capture in low-mass asymptotic giant branch stars: Cross sections and abundance signatures. *ApJ*, 525(2):886.
- Asplund, M., Grevesse, N., Sauval, A. J., and Scott, P. (2009). The chemical composition of the sun. *Annual Review of Astronomy and Astrophysics*, 47(1):481–522.

- Audi, G., Kondev, F. G., Wang, M., Huang, W. J., and Naimi, S. (2017). The NUBASE2016 evaluation of nuclear properties. *Chinese Physics C*, 41(3).
- Balbus, S. A. and Hawley, J. F (1991). A powerful local shear instability in weakly magnetized disks. I - Linear analysis. II - Nonlinear evolution. *ApJ*, 376:214–233.
- Barnes, J. and Kasen, D. (2013). Effect of a high opacity on the light curves of radioactively powered transients from compact object mergers. *ApJ*, 775(1).
- Barnes, J., Kasen, D., Wu, M.-R., and Martínez-Pinedo, G. (2016). Radioactivity and Thermalization in the Ejecta of Compact Object Mergers and Their Impact on Kilonova Light Curves. *ApJ*, 829(2):110.
- Barnes, J., Zhu, Y. L., Lund, K. A., and T. M. Sprouse , et al. (2021). Kilonovae across the nuclear physics landscape: The impact of nuclear physics uncertainties on r-process-powered emission. *ApJ*, 918(2):44.
- Baumgarte, T., Shapiro, S., and Shibata, M. (1999). On the maximum mass of differentially rotating neutron stars. *ApJL*, 528:431–432.
- Bauswein, A., Baumgarte, T. W., and Janka, H.-T. (2013a). Prompt merger collapse and the maximum mass of neutron stars. *Phys. Rev. Lett.*, 111:131101.
- Bauswein, A., Goriely, S., and Janka, H. T. (2013b). Systematics of dynamical mass ejection, nucleosynthesis, and radioactively powered electromagnetic signals from neutron-star mergers. *ApJ*, 773(1).
- Bauswein, A., Just, O., Janka, H.-T., and Stergioulas, N. (2017). Neutron-star radius constraints from gw170817 and future detections. *ApJ Letters*, 850(2):L34.
- Beloborodov, A. M. (2008). Hyper-accreting black holes. *AIP Conference Proceedings*, 1054(1):51–70.
- Beniamini, P. and Lu, W. (2021). Survival times of supramassive neutron stars resulting from binary neutron star mergers. *ApJ*, 920(2):109.
- Bernuzzi, S., Breschi, M., and Daszuta, Boris, et al. (2020). Accretion-induced prompt black hole formation in asymmetric neutron star mergers, dynamical ejecta, and kilonova signals. *MNRAS*, 497(2):1488–1507.
- Bethe, H. A. (1939). Energy production in stars. *Phys. Rev.*, 55:434–456.
- Beun, J., McLaughlin, G. C., Surman, R., and Hix, W. R. (2008). Fission cycling in a supernova *r* process. *Physical Review C*, 77:035804.
- Bildsten, L. (1997). Thermonuclear burning on rapidly accreting neutron stars.
- Blandford, R. D. and Payne, D. G. (1982). Hydromagnetic flows from accretion discs and the production of radio jets. *MNRAS*, 199(4):883–903.
- Blandford, R. D. and Znajek, R. L. (1977). Electromagnetic extraction of energy from Kerr black holes. *MNRAS*, 179(3):433–456.
- Bovard, L. and Rezzolla, L. (2017). On the use of tracer particles in simulations of binary neutron stars. *Classical and Quantum Gravity*, 34(21):215005.

- Buckley, D., of Fuel Cycle, U. N. R. C. D., Safety, M., and Science Applications, i. (1980). *Environmental Assessment of Consumer Products Containing Radioactive Material*. Number v. 88 in Environmental Assessment of Consumer Products Containing Radioactive Material. The Division.
- Bugli, M., Guilet, J., Foglizzo, T., and Obergaulinger, M. (2023). Three-dimensional core-collapse supernovae with complex magnetic structures – II. Rotational instabilities and multimessenger signatures. *MNRAS*, 520(4):5622–5634.
- Bulla, M. (2019). possis: predicting spectra, light curves, and polarization for multidimensional models of supernovae and kilonovae. *MNRAS*, 489(4):5037–5045.
- Burbidge, E. M., Burbidge, G. R., Fowler, W. A., and Hoyle, F. (1957). Synthesis of the elements in stars. *Rev. Mod. Phys.*, 29:547–650.
- Burrows, A., Dessart, L., and E. Livne , et al. (2007). Simulations of magnetically driven supernova and hypernova explosions in the context of rapid rotation. *ApJ*, 664(1):416.
- Burrows, A., Reddy, S., and Thompson, T. A. (2006). Neutrino opacities in nuclear matter. *Nuclear Physics A*, 777:356–394.
- Busso, M., Gallino, R., and Wasserburg, G. J. (1999). Nucleosynthesis in asymptotic giant branch stars: Relevance for galactic enrichment and solar system formation. *Annual Review of Astronomy and Astrophysics*, 37(Volume 37, 1999):239–309.
- Butcher, H. R. (1987). Thorium in G-dwarf stars as a chronometer for the Galaxy. *Nature*, 328:127–131.
- Caballero, O. L., Arcones, A., Borzov, I. N., Langanke, K., and Martinez-Pinedo, G. (2014). Local and global effects of beta decays on r-process.
- Cameron, A. G. W. (1957). Nuclear reactions in stars and nucleogenesis. *Publications of the Astronomical Society of the Pacific*, 69:201.
- Camilletti, A., Chiesa, L., and Riciglion, Giacomo , et al. (2022). Numerical relativity simulations of the neutron star merger GW190425: microphysics and mass ratio effects. *MNRAS*, 516(4):4760–4781.
- Camilletti, A., Perego, A., and Guercilena, Federico Maria , et al. (2024). Geometric and thermodynamic characterization of binary neutron star accretion discs. *Phys. Rev. D*, 109:063023.
- Caprano, C. D., Tews, I., and Brown, Stephanie M. , et al. (2020). Stringent constraints on neutron-star radii from multimessenger observations and nuclear theory. *Nature Astronomy*, 4:625–632.
- Chabanat, E., Bonche, P., Haensel, P., J., M., and Schaeffer, R. (1998). A Skyrme parametrization from subnuclear to neutron star densities Part II. Nuclei far from stabilities. *Nuclear Physics A*, 635(1-2):231–256.
- Chen, M.-H. and Liang, E.-W. (2023). Radioactive decay of specific heavy elements as an energy source for late-time kilonovae and potential James Webb Space Telescope observations. *MNRAS*, 527(3):5540–5546.
- Chladni, E. F. F. (1794). *Ueber den Ursprung der von Pallas gefundenen und anderer ihr ähnlicher Eisenmassen und über einige damit in Verbindung stehende Naturerscheinungen*. Riga: Bey Johann Friedrich Hartknock.

- Chornock, R., Berger, E., and Kasen, D. , et al. (2017). The electromagnetic counterpart of the binary neutron star merger ligo/virgo GW170817. IV. Detection of near-infrared signatures of r-process nucleosynthesis with gemini-south. *ApJL*, 848(2):L19.
- Christie, I. M., Lalakos, A., and Tchekhovskoy, A , et al. (2019). The role of magnetic field geometry in the evolution of neutron star merger accretion discs. *MNRAS*, 490(4):4811–4825.
- Ciolfi, R. and Kalinani, J. V. (2020). Magnetically driven baryon winds from binary neutron star merger remnants and the blue kilonova of August 2017. *ApJ*, 900:L35.
- Clarke, F. W. (1873). Evolution and the spectroscope. *Popular Science Monthly*, 2.
- Coughlin, M. W., Dietrich, T., and Doctor, Zoheyr, et al. (2018). Constraints on the neutron star equation of state from AT2017gfo using radiative transfer simulations. *MNRAS*, 480:3871–3878.
- Coughlin, M. W., Dietrich, T., Margalit, B., and Metzger, B. D. (2019). Multimessenger Bayesian parameter inference of a binary neutron star merger. *MNRAS: Letters*, 489(1):L91–L96.
- Cowperthwaite, P. S., Berger, E., and Villar, V. A., et al. (2017). The electromagnetic counterpart of the binary neutron star merger LIGO/VIRGO GW170817. II. UV, optical, and near-ir light curves and comparison to kilonova models. *ApJL*, 848:L17.
- Curtis, S., Miller, J. M., and Carla Fröhlich, et al. (2023). Nucleosynthesis in outflows from black hole–neutron star merger disks with full gr(ν)rmhd. *ApJ Letters*, 945(1):L13.
- Cusinato, M., Guercilena, F. M., and Perego, Albino, et al. (2022). Neutrino emission from binary neutron star mergers: characterizing light curves and mean energies. *The European Physical Journal A*.
- Cyburt, R. H., Amthor, A. M., and Ferguson, Ryan, et al. (2010). The JINA reaclib database: Its recent updates and impact on type-I X-ray bursts. *ApJS*, 189(1):240–252.
- Danielewicz, P., Lacey, R., and Lynch, W. G. (2002). Determination of the equation of state of dense matter. *Science*, 298(5598):1592–1596.
- De, S., Finstad, D., and Lattimer, James M., et al. (2018). Tidal deformabilities and radii of neutron stars from the observation of gw170817. *Physical Review Letters*, 121:091102.
- de Haas, S., Bosch, P., and Mösta, Philipp, et al. (2023). Magnetic field effects on nucleosynthesis and kilonovae from neutron star merger remnants. *MNRAS*, page stad2931.
- de Marcillac, P., Coron, N., and Dambier, Gérard, et al. (2003). Experimental detection of α -particles from the radioactive decay of natural bismuth. *Nature*, 422(6934):876–878.
- Dessart, L., Ott, C. D., and Burrows, A., et al. (2009). Neutrino signatures and the neutrino-driven wind in binary neutron star mergers. *ApJ*, 690(2):1681–1705.
- Díaz, M. C., Macri, L. M., and Garcia Lambas, D., et al. (2017). Observations of the first electromagnetic counterpart to a gravitational wave source by the TOROS Collaboration. *ApJL*, 848(L29):1–5.
- Dietrich, T., Coughlin, M. W., and Peter T. H. Pang, et al. (2020). Multimessenger constraints on the neutron-star equation of state and the hubble constant. *Science*, 370(6523):1450–1453.

- Dietrich, T. and Ujevic, M. (2017). Modeling dynamical ejecta from binary neutron star mergers and implications for electromagnetic counterparts. *Classical and Quantum Gravity*, 34(10):105014.
- Dolence, J. C., Gammie, C. F., Mościbrodzka, M., and Leung, P. K. (2009). grmonty: A monte carlo code for relativistic radiative transport. *ApJS*, 184(2):387–397.
- Drout, M. R., Piro, A. L., and Shappee, B. J. , et al. (2017). Light curves of the neutron star merger GW170817/SSS17a: Implications for R-process nucleosynthesis. *Science*, 358(6370):1570–1574.
- Duflo, J. and Zuker, A. P. (1995). Microscopic mass formulas. *Physical Review C*, 52(1):23–27.
- Eichler, M., Arcones, A., and A. Kelic , et al. (2015). The role of fission in neutron star mergers and its impact on the r-process peaks. *ApJ*, 808(1):30.
- Eichler, M., Sayar, W., Arcones, A., and Rauscher, T. (2019). Probing the Production of Actinides Under Different R-Process Conditions. *ApJ*, 879(1):47.
- Ekanger, N., Bhattacharya, M., and Horiuchi, S. (2023). Nucleosynthesis in outflows of compact objects and detection prospects of associated kilonovae. *MNRAS*, 525(2):2040–2052.
- Endrizzi, A., Perego, A., and Fabbri, Francesco M., et al. (2020). Thermodynamics conditions of matter in the neutrino decoupling region during neutron star mergers. *European Physical Journal A*, 56(1):15.
- Evans, P., Cenko, S., and Kennea, A.J., et al. (2017). Swift and NuSTAR observations of GW170817: Detection of a blue kilonova. *Science*, 358(6370):1565–1570.
- Even, W., Korobkin, O., and Christopher L. Fryer, et al. (2020). Composition effects on kilonova spectra and light curves. i. *ApJ*, 899(1):24.
- Fahlman, S. and Fernández, R. (2022). Long-term 3D MHD simulations of black hole accretion discs formed in neutron star mergers. *MNRAS*, 513(2):2689–2707.
- Fernández, R., Kasen, D., Metzger, B. D., and Quataert, E. (2014). Outflows from accretion discs formed in neutron star mergers: effect of black hole spin. *MNRAS*, 446(1):750–758.
- Fernández, R. and Metzger, B. D. (2013). Delayed outflows from black hole accretion tori following neutron star binary coalescence. *MNRAS*, 435(1):502–517.
- Fernández, R., Tchekhovskoy, A., and Quataert, Eliot, et al. (2018). Long-term GRMHD simulations of neutron star merger accretion discs: implications for electromagnetic counterparts. *MNRAS*, 482(3):3373–3393.
- Fischer, T., Whitehouse, S. C., and Mezzacappa, A., et al. (2010). Protoneutron star evolution and the neutrino-driven wind in general relativistic neutrino radiation hydrodynamics simulations. *A&A*, 517:A80.
- Fishbone, L. G. and Moncrief, V. (1976). Relativistic fluid disks in orbit around Kerr black holes. *ApJ*, 207:962–976.
- Fontes, C. J., Fryer, C. L., and Hungerford, A L, et al. (2020). A line-binned treatment of opacities for the spectra and light curves from neutron star mergers. *MNRAS*, 493(3):4143–4171.

- Foucart, F., Haas, R., and Duez, Matthew D., et al. (2016). Low mass binary neutron star mergers: Gravitational waves and neutrino emission. *Physical Review D*, 93:044019.
- Foucart, F., O'Connor, E., and Roberts, Luke, et al. (2015). Post-merger evolution of a neutron star-black hole binary with neutrino transport. *Physical Review D*, 91:124021.
- Frebel, A. (2018). From nuclei to the cosmos: Tracing heavy-element production with the oldest stars. *Annual Review of Nuclear and Particle Science*, 68(Volume 68, 2018):237–269.
- Frebel, A., Christlieb, N., and John E. Norris, et al. (2007). Discovery of HE 1523-0901, a strongly r-process-enhanced metal-poor star with detected uranium. *ApJ*, 660(2):L117–L120.
- Fröhlich, C., Martínez-Pinedo, G., and Liebendörfer, M. , et al. (2006). Neutrino-induced nucleosynthesis of $a > 64$ nuclei: The νp process. *Phys. Rev. Lett.*, 96:142502.
- Froustey, J., Richers, S., and Grohs, Evan, et al. (2024). Neutrino fast flavor oscillations with moments: Linear stability analysis and application to neutron star mergers. *Physical Review D*, 109:043046.
- Fujibayashi, S., Kiuchi, K., and Shinya Wanajo, et al. (2023). Comprehensive study of mass ejection and nucleosynthesis in binary neutron star mergers leaving short-lived massive neutron stars. *ApJ*, 942(1):39.
- Gade, A. and Sherrill, B. M. (2016). NSCL and FRIB at Michigan State University: Nuclear science at the limits of stability. *Physica Scripta*, 91(5):053003.
- Gallino, R., Arlandini, C., and Maurizio Busso, et al. (1998). Evolution and nucleosynthesis in low-mass asymptotic giant branch stars. ii. neutron capture and the s-process. *ApJ*, 497(1):388.
- Gallino, R., Raiteri, C. M., and Busso, M. (1992). The s -process in agb stars. *Highlights of Astronomy*, 9:623–625.
- Gamba, R., Read, J. S., and Wade, L. E. (2019). The impact of the crust equation of state on the analysis of GW170817. *Classical and Quantum Gravity*, 37.
- Gammie, C. F., McKinney, J. C., and Toth, G. (2003). Harm: A numerical scheme for general relativistic magnetohydrodynamics. *ApJ*, 589(1):444–457.
- Gamow, G. (1946). Expanding universe and the origin of elements. *Phys. Rev.*, 70:572–573.
- Giuliani, S. A., Martínez-Pinedo, G., Wu, M. R., and Robledo, L. M. (2020). Fission and the r -process nucleosynthesis of translead nuclei in neutron star mergers. *Physical Review C*, 102(4):45804.
- Goldstein, A., Veres, P., and E. Burns, et al. (2017). An ordinary short gamma-ray burst with extraordinary implications: Fermi-gbm detection of grb 170817a. *ApJ Letters*, 848(2):L14.
- Goriely, S. (1999). Uncertainties in the solar system r-abundance distribution. *A&A*, 342:881–891.
- Goriely, S. (2015). The fundamental role of fission during r-process nucleosynthesis in neutron star mergers. *The European Physical Journal A*, 51:22.
- Goriely, S., Bauswein, A., and Janka, H. T. (2011). r-process nucleosynthesis in dynamically ejected matter of neutron star mergers. *ApJL*, 738(2).

- Goriely, S., Bauswein, A., and Just, O., et al. (2015). Impact of weak interactions of free nucleons on the r-process in dynamical ejecta from neutron star mergers. *MNRAS*, 452(4):3894–3904.
- Goriely, S., Chamel, N., and Pearson, J. M. (2013a). Further explorations of Skyrme-Hartree-Fock-Bogoliubov mass formulas. XIII. the 2012 atomic mass evaluation and the symmetry coefficient. *Physical Review C - Nuclear Physics*, 88(2):1–14.
- Goriely, S., Chamel, N., and Pearson, J. M. (2013b). Hartree-Fock-Bogoliubov nuclear mass model with 0.50 MeV accuracy based on standard forms of Skyrme and pairing functionals. *Physical Review C - Nuclear Physics*, 88(6):1–5.
- Goriely, S., Demetriou, P., and H.-Th. Janka, et al. (2005). The r-process nucleosynthesis: a continued challenge for nuclear physics and astrophysics. *Nuclear Physics A*, 758:587–594. Nuclei in the Cosmos VIII.
- Goriely, S., Hilaire, S., and Koning, A. J., et al. (2009). Towards a prediction of fission cross sections on the basis of microscopic nuclear inputs. *Physical Review C - Nuclear Physics*, 79(2):1–13.
- Goriely, S. and Arnould, M. (2001). Actinides: How well do we know their stellar production? *A&A*, 379(3):1113–1122.
- Grossman, D., Korobkin, O., Rosswog, S., and Piran, T. (2014). The long-term evolution of neutron star merger remnants – II. Radioactively powered transients. *MNRAS*, 439(1):757–770.
- Heinemann, T. and Papaloizou, J. C. B. (2009). The excitation of spiral density waves through turbulent fluctuations in accretion discs - II. Numerical simulations with MRI-driven turbulence. *MNRAS*, 397(1):64–74.
- Hill, V., Christlieb, N., and Beers, T. C., et al. (2017). The hamburg/eso r-process enhanced star survey (heres) - xi. the highly r-process-enhanced star cs 29497-004. *A&A*, 607:A91.
- Hill, V., Plez, B., and Cayrel, R., et al. (2002). First stars. i. the extreme r-element rich, iron-poor halo giant cs 31082-001 * - implications for the r-process site(s) and radioactive cosmochronology. *A&A*, 387(2):560–579.
- Holmbeck, E. M., Barnes, J., and Kelsey A. Lund, et al. (2023a). Superheavy elements in kilonovae. *ApJ Letters*, 951(1):L13.
- Holmbeck, E. M., Beers, T. C., and Ian U. Roederer, et al. (2018a). The r-process alliance: 2mass j09544277+5246414, the most actinide-enhanced r-II star known. *ApJ*, 859(2):L24.
- Holmbeck, E. M., Frebel, A., and G. C. McLaughlin, et al. (2019). Actinide-rich and actinide-poor r-process-enhanced metal-poor stars do not require separate r-process progenitors. *ApJ*, 881(1):5.
- Holmbeck, E. M., Hansen, T. T., and Timothy C. Beers, et al. (2020a). The r-process alliance: Fourth data release from the search for r-process-enhanced stars in the galactic halo. *ApJS*, 249(2):30.
- Holmbeck, E. M., Sprouse, T. M., and Mumpower, M. R. (2023b). Nucleosynthesis and observation of the heaviest elements. *The European Physical Journal A*, 59:28.
- Holmbeck, E. M., Sprouse, T. M., and Mumpower, Matthew R., et al. (2018b). Actinide Production in the Neutron-Rich Ejecta of a Neutron Star Merger. *ApJ*, 870(1):23.

- Holmbeck, E. M., Surman, R., and Anna Frebel, et al. (2020b). Characterizing r-process sites through actinide production. *Journal of Physics: Conference Series*, 1668(1):012020.
- Horowitz, C. J., Arcones, A., and B Côté, et al. (2019). r-process nucleosynthesis: connecting rare-isotope beam facilities with the cosmos. *Journal of Physics G: Nuclear and Particle Physics*, 46(8):083001.
- Hotokezaka, K., Kiuchi, K., and Kyutoku, Koutarou, et al. (2013a). Mass ejection from the merger of binary neutron stars. *Physical Review D - Particles, Fields, Gravitation and Cosmology*, 87(2):1–27.
- Hotokezaka, K., Kiuchi, K., and Kyutoku, Koutarou, et al. (2013b). Remnant massive neutron stars of binary neutron star mergers: Evolution process and gravitational waveform. *Phys. Rev. D*, 88:044026.
- Hotokezaka, K., Kyutoku, K., and Okawa, Hirotada, et al. (2011). Binary neutron star mergers: Dependence on the nuclear equation of state. *Phys. Rev. D*, 83:124008.
- Hoyle, F. (1946). The synthesis of the elements from hydrogen. *MNRAS*, 106:343.
- Hoyle, F. (1954). On Nuclear Reactions Occuring in Very Hot STARS.I. the Synthesis of Elements from Carbon to Nickel. *ApJS*, 1:121.
- Hüdepohl, L., Müller, B., and Janka, H.-T., et al. (2010). Neutrino signal of electron-capture supernovae from core collapse to cooling. *Physical Review Letters*, 104:251101.
- Huggins, W. and Miller, W. A. (1864). On the spectra of some of the fixed stars. *Philosophical Transactions of the Royal Society of London*, 154:413–435.
- Hulse, R. A. and Taylor, J. H. (1975a). A deep sample of new pulsars and their spatial extent in the Galaxy. *ApJ Letters*, 201:L55–L59.
- Hulse, R. A. and Taylor, J. H. (1975b). Discovery of a pulsar in a binary system. *ApJ Letters*, 195:L51–L53.
- Janiuk, Agnieszka (2014). Nucleosynthesis of elements in gamma-ray burst engines. *A&A*, 568:A105.
- Jerome, S. et al. (between approximately 1320-1330). *Bible. IE TCD MS 35*. The Catholic Church. Carnegie Corporation of New York, Sponsor.
- Just, O., Bauswein, A., and Ardevol Pulpillo, R., et al. (2015). Comprehensive nucleosynthesis analysis for ejecta of compact binary mergers. *MNRAS*, 448(1):541–567.
- Just, O., Vijayan, V., and Z. Xiong, et al. (2023). End-to-end kilonova models of neutron star mergers with delayed black hole formation. *ApJ Letters*, 951(1):L12.
- Karpov, A. V., Zagrebaev, V. I., Martinez Palenzuela, Y., Felipe Ruiz, L., and Greiner, W. (2012). Decay properties and stability of the heaviest elements. *International Journal of Modern Physics E*, 21(02):1250013.
- Kasen, D., Badnell, N. R., and Barnes, J. (2013). Opacities and spectra of the r-process ejecta from neutron star mergers. *ApJ*, 774(1).
- Kasen, D. and Barnes, J. (2019). Radioactive heating and late time kilonova light curves. *ApJ*, 876(2):128.
- Kasen, D., Metzger, B., and Barnes, Jennifer, et al. (2017). Origin of the heavy elements in binary neutron-star mergers from a gravitational-wave event. *Nature*, 551(7678):80–84.

- Kashyap, R., Das, A., and Radice, David, et al. (2022). Numerical relativity simulations of prompt collapse mergers: Threshold mass and phenomenological constraints on neutron star properties after gw170817. *Physical Review D*, 105:103022.
- Kasliwal, M. M., Kasen, D., and Lau, Ryan M, et al. (2022). Spitzer mid-infrared detections of neutron star merger GW170817 suggests synthesis of the heaviest elements. *MNRASL*, 510(1):L7–L12.
- Kawano, T., Capote, R., Hilaire, S., and Chau Huu-Tai, P. (2016). Statistical Hauser-Feshbach theory with width-fluctuation correction including direct reaction channels for neutron-induced reactions at low energies. *Physical Review C*, 94(1).
- Kedia, A., Ristic, M., and O'Shaughnessy, Richard, et al. (2023). Surrogate light curve models for kilonovae with comprehensive wind ejecta outflows and parameter estimation for at2017gfo. *Phys. Rev. Res.*, 5:013168.
- Keller, S. C., Bessell, M. S., and Frebel, A., et al. (2014). A single low-energy, iron-poor supernova as the source of metals in the star SMSS J031300.36-670839.3. *Nature*, 506(7489):463–466.
- Kerr, R. P. (1963). Gravitational Field of a Spinning Mass as an Example of Algebraically Special Metrics. *Phys. Rev. Letters*, 11(5):237–238.
- Kilpatrick, C. D., Foley, R. J., and D. Kasen, et al. (2017). Electromagnetic evidence that sss17a is the result of a binary neutron star merger. *Science*, 358(6370):1583–1587.
- Kiuchi, K., Kyutoku, K., Shibata, M., and Taniguchi, K. (2019). Revisiting the lower bound on tidal deformability derived by at 2017gfo. *ApJ Letters*, 876(2):L31.
- Kiuchi, K., Reboul-Salze, A., Shibata, M., and Sekiguchi, Y. (2023). A large-scale magnetic field via $\alpha\omega$ dynamo in binary neutron star mergers.
- Kiuchi, K., Sekiguchi, Y., Kyutoku, K., and Shibata, M. (2012). Gravitational waves, neutrino emissions and effects of hyperons in binary neutron star mergers. *Classical and Quantum Gravity*, 29(12):124003.
- Kodama, T. and Takahashi, K. (1975). r-process nucleosynthesis and nuclei far from the region of β -stability. *Nuclear Physics A*, 239(3):489–510.
- Koehn, H., Rose, H., and Peter T. H. Pang, et al. (2024). An overview of existing and new nuclear and astrophysical constraints on the equation of state of neutron-rich dense matter.
- Kohri, K., Narayan, R., and Piran, T. (2005). Neutrino-dominated accretion and supernovae. *ApJ*, 629:341 – 361.
- Kondev, F., Wang, M., and W.J. Huang, et al. (2021). The nubase2020 evaluation of nuclear physics properties *. *Chinese Physics C*, 45(3):030001.
- Körding, E., Falcke, H., and Corbel, S. (2006). Refining the fundamental plane of accreting black holes. *A&A*, 456(2):439–450.
- Korobkin, O., Rosswog, S., Arcones, A., and Winteler, C. (2012). On the astrophysical robustness of the neutron star merger r-process. *MNRAS*, 426(3):1940–1949.

- Kortelainen, M., McDonnell, J., and Nazarewicz, W., et al. (2012). Nuclear energy density optimization: Large deformations. *Physical Review C - Nuclear Physics*, 85(2).
- Kramida, A., Yu. Ralchenko, Reader, J., and and NIST ASD Team (2023). NIST Atomic Spectra Database (ver. 5.11), [Online]. Available: <https://physics.nist.gov/asd>. National Institute of Standards and Technology, Gaithersburg, MD.
- Krüger, C. J. and Foucart, F. (2020). Estimates for disk and ejecta masses produced in compact binary mergers. *Phys. Rev. D*, 101:103002.
- Kulkarni, S. R. (2005). Modeling Supernova-like Explosions Associated with Gamma-ray Bursts with Short Durations. *arXiv*, pages 1–28.
- Kullmann, I., Goriely, S., and Just, O., et al. (2021). Dynamical ejecta of neutron star mergers with nucleonic weak processes I: nucleosynthesis. *MNRAS*, 510(2):2804–2819.
- Kullmann, I., Goriely, S., and Just, O., et al. (2022). Extensive study of nuclear uncertainties and their impact on the r-process nucleosynthesis in neutron star mergers.
- Kullmann, I., Goriely, S., and Just, O., et al. (2023). Impact of systematic nuclear uncertainties on composition and decay heat of dynamical and disc ejecta in compact binary mergers. *MNRAS*, 523(2):2551–2576.
- Lattimer, J. and Schramm, D. (1974). Black-Hole-Neutron-Star Collisions. *ApJL*, 192:L145.
- Lattimer, J. M. (2012). The nuclear equation of state and neutron star masses. *Annual Review of Nuclear and Particle Science*, 62(Volume 62, 2012):485–515.
- Lattimer, J. M. and Schramm, D. N. (1976). The tidal disruption of neutron stars by black holes in close binaries. *ApJ*, 210:549–567.
- Lee, W. H., Ramirez-Ruiz, E., and López-Cámara, D. (2009). Phase transitions and he-synthesis-driven winds in neutrino cooled accretion disks: Prospects for late flares in short gamma-ray bursts. *ApJ*, 699(2):L93.
- Lehner, L., Liebling, S. L., and Palenzuela, Carlos, et al. (2016). Unequal mass binary neutron star mergers and multimessenger signals. *Classical and Quantum Gravity*, 33(18).
- Li, L.-X. and Paczyński, B. (1998). Transient Events from Neutron Star Mergers. *ApJL*, 507(1):L59–L62.
- Li, X. and Siegel, D. M. (2021). Neutrino fast flavor conversions in neutron-star postmerger accretion disks. *Physical Review Letters*, 126:251101.
- Lippuner, J., Fernández, R., and Roberts, Luke F., et al. (2017). Signatures of hypermassive neutron star lifetimes on r-process nucleosynthesis in the disc ejecta from neutron star mergers. *MNRAS*, 472(1):904–918.
- Lippuner, J. and Roberts, L. F. (2017). Skynet: A modular nuclear reaction network library. *ApJS*, 233(2):18.
- Liu, M., Wang, N., Deng, Y., and Wu, X. (2011). Further improvements on a global nuclear mass model. *Physical Review C - Nuclear Physics*, 84(1):1–8.

- Lodders, K. (2003). Solar system abundances and condensation temperatures of the elements. *ApJ*, 591(2):1220.
- Lodders, K., Palme, H., and Gail, H.-P. (2009). 4.4 abundances of the elements in the solar system: Datasheet from landolt-börnstein - group vi astronomy and astrophysics · volume 4b: "solar system".
- Lund, K. A., Engel, J., McLaughlin, G. C., Mumpower, M. R., Ney, E. M., and Surman, R. (2023). The influence of β -decay rates on r-process observables. *ApJ*, 944(2):144.
- Lund, K. A., McLaughlin, G. C., Miller, J. M., and Mumpower, M. R. (2024). Magnetic field strength effects on nucleosynthesis from neutron star merger outflows. *ApJ*, 964(2):111.
- MacFadyen, A. I. and Woosley, S. E. (1999). Collapsars: Gamma-ray bursts and explosions in “failed supernovae”. *ApJ*, 524(1):262.
- Malik, T., Alam, N., and Fortin, M., et al. (2018). GW170817: Constraining the nuclear matter equation of state from the neutron star tidal deformability. *Physical Review C*, 98(3):1–10.
- Malkus, A., Kneller, J. P., McLaughlin, G. C., and Surman, R. (2012). Neutrino oscillations above black hole accretion disks: Disks with electron-flavor emission. *Physical Review D - Particles, Fields, Gravitation and Cosmology*, 86(8):1–9.
- Malkus, A., McLaughlin, G. C., and Surman, R. (2016). Symmetric and standard matter neutrino resonances above merging compact objects. *Physical Review D*, 93(4):045021. <https://link.aps.org/accepted/10.1103/PhysRevD.93.045021>.
- Mamdouh, A., Pearson, J. M., Rayet, M., and Tondeur, F. (2001). Fission barriers of neutron-rich and superheavy nuclei calculated with the ETFSI method. *Nuclear Physics A*, 679(3-4):337–358.
- Margalit, B. and Metzger, B. D. (2017). Constraining the maximum mass of neutron stars from multi-messenger observations of gw170817. *ApJ Letters*, 850(2):L19.
- Marketin, T., Huther, L., and Martínez-Pinedo, G. (2016). Large-scale evaluation of β -decay rates of r-process nuclei with the inclusion of first-forbidden transitions. *Physical Review C*, 93(2):1–17.
- Martin, D., Perego, A., and Arcones, A., et al. (2015). Neutrino-driven winds in the aftermath of a neutron star merger: Nucleosynthesis and electromagnetic transients. *ApJ*, 813(1):2.
- Martin, D., Perego, A., Kastaun, W., and Arcones, A. (2018). The role of weak interactions in dynamic ejecta from binary neutron star mergers. *Classical and Quantum Gravity*, 35(3):034001.
- Martínez-Pinedo, G., Fischer, T., Lohs, A., and Huther, L. (2012). Charged-current weak interaction processes in hot and dense matter and its impact on the spectra of neutrinos emitted from protoneutron star cooling. *Physical Review Letters*, 109:251104.
- Marvin, U. B. (1996). Ernst florens friedrich chladni (1756–1827) and the origins of modern meteorite research. *Meteoritics & Planetary Science*, 31(5):545–588.
- Mayer, M. G. (1948). On closed shells in nuclei. *Phys. Rev.*, 74:235–239.
- McKinney, J. C. and Gammie, C. F. (2004). A Measurement of the Electromagnetic Luminosity of a Kerr Black Hole. *ApJ*, 611(2):977–995.

- McLaughlin, G. and Surman, R. (2005). Prospects for obtaining an r process from gamma ray burst disk winds. *Nuclear Physics A*, 758:189–196. Nuclei in the Cosmos VIII.
- Mendoza-Temis, J. D. J., Wu, M. R., and Langanke, Karlheinz, et al. (2015). Nuclear robustness of the r process in neutron-star mergers. *Physical Review C - Nuclear Physics*, 92(5):1–16.
- Metzger, B. D. (2020). Kilonovae. *Living Reviews in Relativity*, 23(1).
- Metzger, B. D., Martínez-Pinedo, G., and Darbha, S., et al. (2010). Electromagnetic counterparts of compact object mergers powered by the radioactive decay of r-process nuclei. *MNRAS*, 406(4):2650–2662.
- Metzger, B. D., Piro, A. L., and Quataert, E. (2009). Neutron-rich freeze-out in viscously spreading accretion discs formed from compact object mergers. *MNRAS*, 396(1):304–314.
- Metzger, B. D., Thompson, T. A., and Quataert, E. (2018). A magnetar origin for the Kilonova ejecta in GW170817. *ApJ*, 856(2):101.
- Meyer, B. S., Mathews, G. J., and Howard, W. M., et al. (1992). R-Process Nucleosynthesis in the High-Entropy Supernova Bubble. *ApJ*, 399:656.
- Mignone, A. and McKinney, J. C. (2007). Equation of state in relativistic magnetohydrodynamics: variable versus constant adiabatic index. *MNRAS*, 378(3):1118–1130.
- Miller, J. M., Ryan, B. R., and Dolence, J. C. (2019a). ν bhlight: Radiation grmhd for neutrino-driven accretion flows. *ApJS*, 241(2):30.
- Miller, J. M., Ryan, B. R., and Dolence, Joshua C., et al. (2019b). Full transport model of GW170817-like disk produces a blue kilonova. *Physical Review D*, 100(2):23008.
- Miller, J. M., Sprouse, T. M., and Christopher L. Fryer, et al. (2020). Full transport general relativistic radiation magnetohydrodynamics for nucleosynthesis in collapsars. *ApJ*, 902(1):66.
- Möller, P., Mumpower, M. R., Kawano, T., and Myers, W. D. (2019). Nuclear properties for astrophysical and radioactive-ion-beam applications (II). *Atomic Data and Nuclear Data Tables*, 125(July 2018):1–192.
- Möller, P., Pfeiffer, B., and Kratz, K.-L. (2003). New calculations of gross β -decay properties for astrophysical applications: Speeding-up the classical r process. *Physical Review C*, 67:055802.
- Möller, P., Sierk, A. J., Ichikawa, T., Iwamoto, A., and Mumpower, M. (2015). Fission barriers at the end of the chart of the nuclides. *Physical Review C - Nuclear Physics*, 91(2):1–27.
- Möller, P., Sierk, A. J., Ichikawa, T., and Sagawa, H. (2016). Nuclear ground-state masses and deformations: FRDM(2012). *Atomic Data and Nuclear Data Tables*, 109-110:1–204.
- Most, E. R., Papenfort, L. J., and Dexheimer, Veronica, et al. (2019). Signatures of quark-hadron phase transitions in general-relativistic neutron-star mergers. *Phys. Rev. Lett.*, 122:061101.
- Mösta, P., Roberts, L. F., and Goni Halevi, et al. (2018). r-process nucleosynthesis from three-dimensional magnetorotational core-collapse supernovae. *ApJ*, 864(2):171.

- Mościbrodzka, M., Falcke, H., and Noble, S. (2016). Scale-invariant radio jets and varying black hole spin. *A&A*, 596:A13.
- Mumpower, M. R., Kawano, T., and Möller, P. (2016a). Neutron- γ competition for β -delayed neutron emission. *Physical Review C*, 94(6):1–8.
- Mumpower, M. R., Kawano, T., and Sprouse, T. M., et al. (2018). β -Delayed Fission in R-Process Nucleosynthesis. *ApJ*, 869(1):14.
- Mumpower, M. R., McLaughlin, G. C., and Surman, R. (2012). Formation of the rare-earth peak: Gaining insight into late-time r -process dynamics. *Physical Review C*, 85:045801.
- Mumpower, M. R., Surman, R., McLaughlin, G. C., and Aprahamian, A. (2016b). The impact of individual nuclear properties on r-process nucleosynthesis. *Progress in Particle and Nuclear Physics*, 86:86–126.
- Mustonen, M. T. and Engel, J. (2016). Global description of β^- decay in even-even nuclei with the axially-deformed Skyrme finite-amplitude method. *Physical Review C*, 93:014304.
- Myers, W. D. and Świątecki, W. J. (1996). Nuclear properties according to the Thomas-Fermi model. *Nuclear Physics A*, 601(2):141–167.
- Myers, W. D. and Świątecki, W. J. (1999). Thomas-Fermi fission barriers. *Physical Review C - Nuclear Physics*, 60(1):4.
- Narayan, R., Igumenshchev, I. V., and Abramowicz, M. A. (2003). Magnetically Arrested Disk: an Energetically Efficient Accretion Flow. *Publications of the Astronomical Society of Japan*, 55(6):L69–L72.
- Narayan, R., Sądowski, A., Penna, R. F., and Kulkarni, A. K. (2012). GRMHD simulations of magnetized advection-dominated accretion on a non-spinning black hole: role of outflows. *MNRAS*, 426(4):3241–3259.
- Nedora, V., Bernuzzi, S., and David Radice, et al. (2019). Spiral-wave wind for the blue kilonova. *ApJ Letters*, 886(2):L30.
- Nedora, V., Bernuzzi, S., and David Radice, et al. (2021). Numerical relativity simulations of the neutron star merger GW170817: Long-term remnant evolutions, winds, remnant disks, and nucleosynthesis. *ApJ*, 906(2):98.
- Ness, M., Freeman, K., and Athanassoula, E., et al. (2013). ARGOS – III. Stellar populations in the Galactic bulge of the Milky Way. *MNRAS*, 430(2):836–857.
- Ney, E. M., Engel, J., Li, T., and Schunck, N. (2020). Global description of β -decay with the axially deformed Skyrme finite-amplitude method: Extension to odd-mass and odd-odd nuclei. *Physical Review C*, 102(3):1–10.
- Nicholl, M., Berger, E., and Kasen, D., et al. (2017). The electromagnetic counterpart of the binary neutron star merger ligo/virgo Gw170817. Iii. Optical and Uv spectra of a blue kilonova from fast polar ejecta. *ApJL*, 848(2):L18.
- Nikas, S., Perdikakis, G., and Beard, M., et al. (2020). Propagation of hauser-feshbach uncertainty estimates to r-process nucleosynthesis: Benchmark of statistical property models for neutron rich nuclei far from stability.

- Novikov, I. D. and Thorne, K. S. (1973). Astrophysics of black holes. In *Black Holes (Les Astres Occlus)*, pages 343–450.
- Obergaulinger, M. and Aloy, M. A. (2022). Magnetorotational core collapse of possible gamma-ray burst progenitors – IV. A wider range of progenitors. *MNRAS*, 512(2):2489–2507.
- O'Connor, E. and Ott, C. D. (2010a). A new open-source code for spherically symmetric stellar collapse to neutron stars and black holes. *Classical and Quantum Gravity*, 27(11):114103.
- O'Connor, E. and Ott, C. D. (2010b). Stellar collapse: Microphysics. Online access. <https://stellarcollapse.org/equationofstate>.
- Oechslin, R. and Janka, H.-T. (2006). Torus formation in neutron star mergers and well-localized short gamma-ray bursts. *MNRAS*, 368(4):1489–1499.
- Oechslin, R., Janka, H.-T., and Marek, A. (2007). Relativistic neutron star merger simulations with non-zero temperature equations of state. *Astronomy & Astrophysics*, 467(2):395–409.
- Oppenheimer, J. R. and Volkoff, G. M. (1939). On massive neutron cores. *Phys. Rev.*, 55:374–381.
- Orford, R., Vassh, N., and Clark, J. A., et al. (2022). Searching for the origin of the rare-earth peak with precision mass measurements across ce–eu isotopic chains. *Physical Review C*, 105:L052802.
- Padilla-Gay, I., Shalgar, S., and Tamborra, I. (2024). Symmetry breaking due to multi-angle matter-neutrino resonance in neutron star merger remnants. *Journal of Cosmology and Astroparticle Physics*, 2024(05):037.
- Pang, P. T. H., Dietrich, T., and Coughlin, Michael W., et al. (2023). An updated nuclear-physics and multi-messenger astrophysics framework for binary neutron star mergers. *Nature Communications*, 14:8352.
- Panov, I. V. and Janka, H. T. (2009). On the dynamics of proto-neutron star winds and r-process nucleosynthesis. *Astronomy & Astrophysics*, 494(3):829–844.
- Perego, A., Bernuzzi, S., and Radice, D. (2019). Thermodynamics conditions of matter in neutron star mergers. *European Physical Journal A*, 55(8):124.
- Perego, A., Cabezón, R. M., and Käppeli, R. (2016). An advanced leakage scheme for neutrino treatment in astrophysical simulations. *ApJS*, 223(2):22. <https://iopscience.iop.org/article/10.3847/0067-0049/223/2/22/pdf>.
- Perego, A., Radice, D., and Bernuzzi, S. (2017). AT2017gfo: An Anisotropic and Three-Component Kilonova Counterpart of GW170817. *ApJL*, 850(2):L37.
- Perego, A., Rosswog, S., and Cabezón, R. M., et al. (2014). Neutrino-driven winds from neutron star merger remnants. *MNRAS*, 443(4):3134–3156.
- Perego, A., Vescovi, D., and Achille Fiore, et al. (2022). Production of very light elements and strontium in the early ejecta of neutron star mergers. *ApJ*, 925(1):22.
- Pian, E., D'Avanzo, P., and Benetti, S., et al. (2017). Spectroscopic identification of r-process nucleosynthesis in a double neutron-star merger. *Nature*, 551(7678):67–70.

- Pignatari, M., Gallino, R., and M. Heil, et al. (2010). The weak s-process in massive stars and its dependence on the neutron capture cross sections. *ApJ*, 710(2):1557.
- Placco, V. M., Holmbeck, E. M., and Anna Frebel, et al. (2017). RAVE j203843.2–002333: The first highly r-process-enhanced star identified in the RAVE survey. *ApJ*, 844(1):18.
- Popham, R., Woosley, S. E., and Fryer, C. (1999). Hyperaccreting black holes and gamma-ray bursts. *ApJ*, 518(1):356.
- Porth, O., Chatterjee, K., Narayan, R., and Collaboration), T. E. H. T. (2019). The event horizon general relativistic magnetohydrodynamic code comparison project. *ApJ*, 243(2):26.
- Powell, J., Müller, B., Aguilera-Dena, D. R., and Langer, N. (2023). Three dimensional magnetorotational core-collapse supernova explosions of a 39 solar mass progenitor star. *MNRAS*, 522(4):6070–6086.
- Qian, Y. Z. and Woosley, S. E. (1996). Nucleosynthesis in Neutrino-driven Winds. I. The Physical Conditions. *ApJ*, 471:331.
- Radice, D., Galeazzi, F., and Lippuner, Jonas, et al. (2016). Dynamical mass ejection from binary neutron star mergers. *MNRAS*, 460(3):3255–3271.
- Radice, D., Perego, A., Bernuzzi, S., and Zhang, B. (2018a). Long-lived remnants from binary neutron star mergers. *MNRAS*, 481(3):3670–3682.
- Radice, D., Perego, A., and Hotokezaka, Kenta, et al. (2018b). Binary neutron star mergers: Mass ejection, electromagnetic counterparts, and nucleosynthesis. *ApJ*, 869(2):130.
- Radice, D., Perego, A., Zappa, F., and Bernuzzi, S. (2017). GW170817: Joint constraint on the neutron star equation of state from multimessenger observations. *ApJL*, 852(2):L29.
- Reichert, M., Bugli, M., and Guilet, Jérôme, et al. (2024). Nucleosynthesis in magnetorotational supernovae: impact of the magnetic field configuration. *MNRAS*, 529(4):3197–3209.
- Reichert, M., Obergaulinger, M., and Aloy, M. Á, et al. (2022). Magnetorotational supernovae: a nucleosynthetic analysis of sophisticated 3D models. *MNRAS*, 518(1):1557–1583.
- Reichert, M., Obergaulinger, M., Eichler, M., Aloy, M. A., and Arcones, A. (2021). Nucleosynthesis in magneto-rotational supernovae. *MNRAS*, 501(4):5733–5745.
- Reichert, M., Winteler, C., and O. Korobkin, et al. (2023). The nuclear reaction network winnet. *ApJS*, 268(2):66.
- Ren, J., Christlieb, N., and Zhao, G. (2012). The hamburg/eso r-process enhanced star survey (heres) - vii. thorium abundances in metal-poor stars. *A&A*, 537:A118.
- Ressler, S. M., Tchekhovskoy, A., Quataert, E., and Gammie, C. F. (2017). The disc-jet symbiosis emerges: modelling the emission of Sagittarius A* with electron thermodynamics. *MNRAS*, 467(3):3604–3619.
- Richers, S., Kasen, D., and O'Connor, Evan, et al. (2015). Monte Carlo neutrino Transport Through Remnant Disks from Neutron Star Mergers. *ApJ*, 813(1):38.
- Ristić, M., Holmbeck, E. M., and Ryan T. Wollaeger, et al. (2023). Constraining inputs to realistic kilonova simulations through comparison to observed r-process abundances. *ApJ*, 956(1):64.

- Roberts, L. F., Kasen, D., Lee, W. H., and Ramirez-Ruiz, E. (2011). Electromagnetic transients powered by nuclear decay in the tidal tails of coalescing compact binaries. *ApJ*, 736(1):L21.
- Roberts, L. F., Reddy, S., and Shen, G. (2012). Medium modification of the charged-current neutrino opacity and its implications. *Physical Review C*, 86:065803.
- Robin, C., Litvinova, E., and Martínez-Pinedo, G. (2022). Beyond-mean-field calculations of allowed and first-forbidden β -decays of r-process waiting-point nuclei. In *European Physical Journal Web of Conferences*, volume 260 of *European Physical Journal Web of Conferences*, page 03002.
- Rockefeller, G., Fryer, C. L., and Patrick Young, et al. (2008). Nucleosynthetic yields from "collapsars".
- Rosswog, S., Liebenörfer, M., and Thielemann, F.K., et al. (1999). Mass ejection in neutron star mergers. *A&A*, 341:499–526.
- Ruffert, M., Janka, H. T., Takahashi, K., and Schäfer, G. (1997). Coalescing neutron stars - A step towards physical models: II. Neutrino emission, neutron tori, and gamma-ray bursts. *Astronomy & Astrophysics*, 319(1):122–153.
- Rusotto, P., Gannon, S., and Kupny, S., et al. (2016). Results of the asy-eos experiment at gsi: The symmetry energy at suprasaturation density. *Phys. Rev. C*, 94:034608.
- Ryan, B. R., Dolence, J. C., and Gammie, C. F. (2015). bhlight: General relativistic radiation magnetohydrodynamics with monte carlo transport. *ApJ*, 807(1):31.
- Sano, T., ichiro Inutsuka, S., Turner, N. J., and Stone, J. M. (2004). Angular momentum transport by magnetohydrodynamic turbulence in accretion disks: Gas pressure dependence of the saturation level of the magnetorotational instability. *ApJ*, 605(1):321.
- Savard, G., Brodeur, M., and Clark, J. A., et al. (2020). The N = 126 factory: A new facility to produce very heavy neutron-rich isotopes. *Nuclear Instruments and Methods in Physics Research B*, 463:258–261.
- Savchenko, V., Ferrigno, C., and E. Kuulkers, et al. (2017). Integral detection of the first prompt gamma-ray signal coincident with the gravitational-wave event gw170817. *ApJ Letters*, 848(2):L15.
- Schatz, H., Aprahamian, A., and Barnard, V., et al. (2001). End point of the rp process on accreting neutron stars. *Phys. Rev. Lett.*, 86:3471–3474.
- Schatz, H., Reyes, A. D. B., and A Best, et al. (2022). Horizons: nuclear astrophysics in the 2020s and beyond. *Journal of Physics G: Nuclear and Particle Physics*, 49(11):110502.
- Schatz, H., Toenjes, R., and Bernd Pfeiffer, et al. (2002). Thorium and uranium chronometers applied to cs 31082-001. *ApJ*, 579(2):626.
- Seeger, P. A., Fowler, W. A., and Clayton, D. D. (1965). Nucleosynthesis of Heavy Elements by Neutron Capture. *ApJS*, 11:121.
- Sekiguchi, Y., Kiuchi, K., Kyutoku, K., and Shibata, M. (2011). Gravitational waves and neutrino emission from the merger of binary neutron stars. *Phys. Rev. Lett.*, 107:051102.
- Sekiguchi, Y., Kiuchi, K., Kyutoku, K., and Shibata, M. (2015). Dynamical mass ejection from binary neutron star mergers: Radiation-hydrodynamics study in general relativity. *Physical Review D - Particles, Fields, Gravitation and Cosmology*, 91(6):1–7.

- Shafer, T., Engel, J., and Fröhlich, C., et al. (2016). β decay of deformed *r*-process nuclei near $a = 80$ and $a = 160$, including odd- a and odd-odd nuclei, with the Skyrme finite-amplitude method. *Physical Review C*, 94:055802.
- Shah, S. P., Ezzeddine, R., and Alexander P. Ji, et al. (2023). Uranium abundances and ages of r-process enhanced stars with novel u ii lines. *ApJ*, 948(2):122.
- Shakura, N. I. and Sunyaev, R. A. (1973). Black holes in binary systems. Observational appearance. *A&A*, 24:337–355.
- Shibata, M., Sekiguchi, Y.-i., and Takahashi, R. (2007). Magnetohydrodynamics of Neutrino-Cooled Accretion Tori around a Rotating Black Hole in General Relativity. *Progress of Theoretical Physics*, 118(2):257–302.
- Shibata, M. and Taniguchi, K. (2006). Merger of binary neutron stars to a black hole: Disk mass, short gamma-ray bursts, and quasinormal mode ringing. *Phys. Rev. D*, 73:064027.
- Shibata, M., Taniguchi, K., and Uryū, K. b. o. (2005). Merger of binary neutron stars with realistic equations of state in full general relativity. *Physical Review D*, 71:084021.
- Siegel, D. M., Barnes, J., and Metzger, B. D. (2019). Collapsars as a major source of r-process elements. *Nature*, 569(7755):241–244.
- Siegel, D. M. and Metzger, B. D. (2017). Three-Dimensional General-Relativistic Magnetohydrodynamic Simulations of Remnant Accretion Disks from Neutron Star Mergers: Outflows and r -Process Nucleosynthesis. *Physical Review Letters*, 119(23):1–7.
- Siegel, D. M. and Metzger, B. D. (2018). Three-dimensional grmhd simulations of neutrino-cooled accretion disks from neutron star mergers. *ApJ*, 858(1):52.
- Siqueira Mello, C., Spite, M., and Barbuy, B., et al. (2013). First stars - xvi. hst/stis abundances of heavy elements in the uranium-rich metal-poor star cs 31082-001. *A&A*, 550:A122.
- Skinner, M. A., Dolence, J. C., and Adam Burrows, et al. (2019). Fornax: A flexible code for multiphysics astrophysical simulations. *ApJ*, 241(1):7.
- Smartt, S. J., Chen, T. W., and Jerkstrand, A., et al. (2017). A kilonova as the electromagnetic counterpart to a gravitational-wave source. *Nature*, 551(7678):75–79.
- Sneden, C., Cowan, J. J., and James E. Lawler, et al. (2003). The extremely metal-poor, neutron capture-rich star CS 22892-052: A comprehensive abundance analysis. *ApJ*, 591(2):936–953.
- Soares-Santos, M., Holz, D. E., Annis, J., Survey, T. D. E., and Collaboration), T. D. E. C. G.-E. (2017). The electromagnetic counterpart of the binary neutron star merger ligo/virgo gw170817. i. discovery of the optical counterpart using the dark energy camera. *ApJ Letters*, 848(2):L16.
- Sprouse, T. M., Lund, K. A., and Jonah M. Miller, et al. (2024). Emergent nucleosynthesis from a 1.2 s long simulation of a black hole accretion disk. *ApJ*, 962(1):79.
- Sprouse, T. M., Mumpower, M. R., and Surman, R. (2021). Following nuclei through nucleosynthesis: A novel tracing technique. *Physical Review C*, 104(1):015803.

- Sprouse, T. M., Navarro Perez, R., and Surman, R., et al. (2020). Propagation of statistical uncertainties of skyrme mass models to simulations of r -process nucleosynthesis. *Physical Review C*, 101:055803.
- Steiner, A. W., Hempel, M., and Fischer, T. (2013). Core-collapse supernova equations of state based on neutron star observations. *ApJ*, 774(1).
- Stewart, A. R., Lo, L.-T., and Korobkin, Oleg, et al. (2022). Realistic kilonova up close.
- Straniero, O., Gallino, R., and Busso, M., et al. (1995). Radiative 13C Burning in Asymptotic Giant Branch Stars and s-Processing. *ApJL*, 440:L85.
- Suess, H. E. and Urey, H. C. (1956). Abundances of the elements. *Rev. Mod. Phys.*, 28:53–74.
- Surman, R. and McLaughlin, G. C. (2004). Neutrinos and nucleosynthesis in gamma-ray burst accretion disks. *ApJ*, 603(2):611.
- Surman, R., McLaughlin, G. C., and Hix, W. R. (2006). Nucleosynthesis in the Outflow from Gamma-Ray Burst Accretion Disks. *ApJ*, 643(2):1057–1064.
- Surman, R., McLaughlin, G. C., and M. Ruffert, et al. (2008). r-process nucleosynthesis in hot accretion disk flows from black hole-neutron star mergers. *ApJ*, 679(2):L117.
- Surman, Rebecca and Mumpower, Matthew (2018). Masses and lifetimes for r-process nucleosynthesis: Frib outlook. *EPJ Web Conf.*, 178:04002.
- Symbalisty, E. and Schramm, D. N. (1982). Neutron Star Collisions and the r-Process. *ApJ Letters*, 22:143.
- Symbalisty, E. M. D., Schramm, D. N., and Wilson, J. R. (1985). An expanding vortex site for the r-process in rotating stellar collapse. *ApJ Letters*, 291:L11–L14.
- Tain, J., Agramunt, J., and Algorta, A., et al. (2018). The briken project: extensive measurements of β -delayed neutron emitters for the astrophysical r process. *Acta physica polonica B*, 49(3):417–428.
- Takahashi, K., Witti, J., and Janka, H. T. (1994). Nucleosynthesis in neutrino-driven winds from protoneutron stars II. The r-process. *A&A*, 286:857–869.
- Takami, K., Rezzolla, L., and Baiotti, L. (2014). Constraining the equation of state of neutron stars from binary mergers. *Phys. Rev. Lett.*, 113:091104.
- Tanaka, M. and Hotokezaka, K. (2013). Radiative transfer simulations of neutron star merger ejecta. *ApJ*, 775(2).
- Tanaka, M., Kato, D., Gaigalas, G., and Kawaguchi, K. (2020). Systematic opacity calculations for kilonovae. *MNRAS*, 496(2):1369–1392.
- Tanvir, N. R., Levan, A. J., and C. González-Fernández, et al. (2017). The emergence of a lanthanide-rich kilonova following the merger of two neutron stars. *ApJ Letters*, 848(2):L27.
- Tchekhovskoy, A., McKinney, J. C., and Narayan, R. (2007). WHAM: a WENO-based general relativistic numerical scheme - I. Hydrodynamics. *MNRAS*, 379(2):469–497.
- Tews, I., Carlson, J., Gandolfi, S., and Reddy, S. (2018). Constraining the speed of sound inside neutron stars with chiral effective field theory interactions and observations. *ApJ*, 860(2):149.

- Thielemann, F.-K., Eichler, M., and Panov, Igor, et al. (2017). *Making the Heaviest Elements in a Rare Class of Supernovae*, pages 1–35. Springer International Publishing, Cham.
- Thompson, T. A., Burrows, A., and Meyer, B. S. (2001). The physics of proto-neutron star winds: Implications for r-process nucleosynthesis. *ApJ*, 562(2):887.
- van Putten, M. H. and Valle, M. D. (2019). Observational evidence for extended emission to GW170817. *MNRAS: Letters*, 482(1):L46–L49.
- Vassh, N., Vogt, R., and Surman, R., et al. (2019). Using excitation-energy dependent fission yields to identify key fissioning nuclei in r-process nucleosynthesis. *Journal of Physics G: Nuclear and Particle Physics*, 46(6).
- Velikhov, E. (1959). Stability of an ideally conducting liquid flowing between rotating cylinders in a magnetic field. *Zhur. Eksptl' i Teoret. Fiz.*, 36(5).
- Villar, V. A., Guillochon, J., and Berger, E., et al. (2017). The combined ultraviolet, optical, and near-infrared light curves of the kilonova associated with the binary neutron star merger gw170817: unified data set, analytic models, and physical implications. *ApJL*, 851(1):L21.
- Virtanen, P., Gommers, R., and SciPy 1.0 Contributors (2020). SciPy 1.0: Fundamental Algorithms for Scientific Computing in Python. *Nature Methods*, 17:261–272.
- Wanajo, S., Janka, H. T., Müller, B., and Kubono, S. (2011). Proton vs. neutron captures in the neutrino winds of core-collapse supernovae. *Journal of Physics: Conference Series*, 312(4):042008.
- Wanajo, S., Kajino, T., Mathews, G. J., and Otsuki, K. (2001). The r-process in neutrino-driven winds from nascent, “compact” neutron stars of core-collapse supernovae. *ApJ*, 554(1):578.
- Wanajo, S., Sekiguchi, Y., and Nishimura, Nobuya, et al. (2014). Production of all the r-process nuclides in the dynamical ejecta of neutron star mergers. *ApJL*, 789(2).
- Wang, M., Audi, G., and Kondev, F. G., et al. (2017). The AME2016 atomic mass evaluation (II). Tables, graphs and references. *Chinese Physics C*, 41(3).
- Wang, M., Huang, W., and F.G. Kondev, et al. (2021). The ame 2020 atomic mass evaluation (ii). tables, graphs and references*. *Chinese Physics C*, 45(3):030003.
- Watson, D., Hansen, C. J., and Selsing, Jonatan, et al. (2019). Identification of strontium in the merger of two neutron stars. *Nature*, 574(7779):497–500.
- Waxman, E., Ofek, E. O., Kushnir, D., and Gal-Yam, A. (2018). Constraints on the ejecta of the GW170817 neutron star merger from its electromagnetic emission. *MNRAS*, 481(3):3423–3441.
- Winteler, C., Käppeli, R., and A. Perego, et al. (2012). Magnetorotationally driven supernovae as the origin of early galaxy r-process elements? *ApJ Letters*, 750(1):L22.
- Wollaeger, R. T., Korobkin, O., and Fontes, Christopher J, et al. (2018). Impact of ejecta morphology and composition on the electromagnetic signatures of neutron star mergers. *MNRAS*, 478(3):3298–3334.
- Woosley, S. E. and Heger, A. (2006). The progenitor stars of gamma-ray bursts. *ApJ*, 637(2):914.

- Woosley, S. E. and Hoffman, R. D. (1992). The alpha -Process and the r-Process. *ApJ*, 395:202.
- Woosley, S. E., Wilson, J. R., and Mathews, G. J., et al. (1994). The r-Process and Neutrino-heated Supernova Ejecta. *ApJ*, 433:229.
- Wu, J., Nishimura, S., and Möller, P., et al. (2020). β -decay half-lives of 55 neutron-rich isotopes beyond the N =82 shell gap. *Physical Review C*, 101(4):042801.
- Wu, M. R., Barnes, J., Martínez-Pinedo, G., and Metzger, B. D. (2019). Fingerprints of Heavy-Element Nucleosynthesis in the Late-Time Lightcurves of Kilonovae. *Physical Review Letters*, 122(6):62701.
- Wu, M. R., Fernández, R., Martínez-Pinedo, G., and Metzger, B. D. (2016). Production of the entire range of r-process nuclides by black hole accretion disc outflows from neutron star mergers. *MNRAS*, 463(3):2323–2334.
- Zagrebaev, V. I., Karpov, A. V., Mishustin, I. N., and Greiner, W. (2011). Production of heavy and superheavy neutron-rich nuclei in neutron capture processes. *Physical Review C - Nuclear Physics*, 84(4):1–8.
- Zhu, Y., Wollaeger, R. T., and Vassh, N., et al. (2018). Californium-254 and Kilonova Light Curves. *ApJ*, 863(2):L23.
- Zhu, Y. L., Lund, K. A., and J. Barnes, et al. (2021). Modeling kilonova light curves: Dependence on nuclear inputs. *ApJ*, 906(2):94.
- Zhu, Y. L., Perego, A., and McLaughlin, G. C. (2016). Matter-neutrino resonance transitions above a neutron star merger remnant. *Physical Review D*, 94:105006.